

**UNIVERSITY OF GAZIANTEP  
GRADUATE SCHOOL OF  
NATURAL & APPLIED SCIENCES**

**INVESTIGATION OF FIRST-STAGE SINTERING  
KINETICS OF UO<sub>2</sub>, ThO<sub>2</sub> AND (Th,U)O<sub>2</sub> PELLETS  
MANUFACTURED BY INTERNAL GELATION  
TECHNIQUE OF SOL-GEL PROCESS**

**Ph.D THESIS  
IN  
ENGINEERING PHYSICS**

**BY  
AYŞE SİBEL SÖKÜCÜ (ALTUNBAYRAK)  
DECEMBER 2015**

**DECEMBER 2015**

**Ph.D THESIS IN ENGINEERING PHYSICS**

**AYŞE SİBEL SÖKÜCÜ  
(ALTUNBAYRAK)**

**Investigation of First-Stage Sintering Kinetics of UO<sub>2</sub>, ThO<sub>2</sub>  
and (Th,U)O<sub>2</sub> Pellets Manufactured by Internal Gelation  
Technique of Sol-Gel Process**

**Ph.D Thesis**

**in**

**Physics Engineering**

**University of Gaziantep**

**Supervisor**

**Prof. Dr. Metin BEDİR**

**Co-Supervisor**

**Assoc. Prof. Dr. M.Timuçin AYBERS**

**by**

**Ayşe Sibel SÖKÜCÜ (ALTUNBAYRAK)**

**December 2015**

©2015 [AYŞE SİBEL SÖKÜCÜ (ALTUNBAYRAK)]

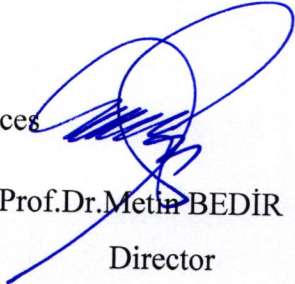
REPUBLIC OF TURKEY  
UNIVERSITY OF GAZIANTEP  
GRADUATE SCHOOL OF NATURAL & APPLIED SCIENCES  
ENGINEERING PHYSICS

Name of the thesis: Investigation of First-Stage Sintering Kinetics of  $UO_2$ ,  $ThO_2$  and  $(Th,U)O_2$  Pellets Manufactured by Internal Gelation Technique of Sol-Gel Process.

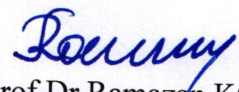
Name of the student: Ayşe Sibel SÖKÜCÜ (ALTUNBAYRAK)

Exam date: 25.12.2015

Approval of the Graduate School of Natural and Applied Sciences

  
Prof. Dr. Metin BEDİR  
Director

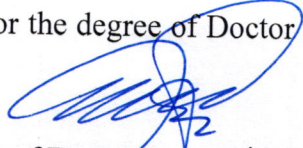
I certify that this thesis satisfies all the requirements as a thesis for the degree of Master of Science/Doctor of Philosophy.

  
Prof. Dr. Ramazan KOÇ  
Head of Department

This is to certify that we have read this thesis and that in our consensus/majority opinion it is fully adequate, in scope and quality, as a thesis for the degree of Doctor of Philosophy.

Assoc. Prof. Dr. M. Timuçin AYBERS  
Co-Supervisor



  
Prof. Dr. Metin BEDİR  
Supervisor

Examining Committee Members

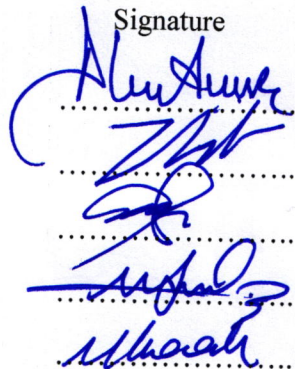
Prof. Dr. Fikret ANLI

Prof. Dr. Zihni ÖZTÜRK

Prof. Dr. Metin BEDİR

Assoc. Prof. Dr. Fatih HASOĞLU

Asst. Prof. Dr. Mehmet KOÇAK

Signature  


**I hereby declare that all information in this document has been obtained and presented in accordance with academic rules and ethical conduct. I also declare that, as required by these rules and conduct, I have fully cited and referenced all material and results that are not original to this work.**

**Ayşe Sibel SÖKÜCÜ (ALTUNBAYRAK)**

**İmza**

## ABSTRACT

### INVESTIGATION OF FIRST-STAGE SINTERING KINETICS OF $UO_2$ , $ThO_2$ AND $(Th,U)O_2$ PELLETS MANUFACTURED BY INTERNAL GELATION TECHNIQUE OF SOL-GEL PROCESS

SÖKÜCÜ (ALTUNBAYRAK), Ayşe Sibel

Ph.D. Thesis, Engineering Physics, University of Gaziantep

Supervisor: Prof. Dr. Metin BEDİR

Co-Supervisor: Assoc. Prof. Dr. M.Timuçin AYBERS

December 2015

100 pages

The sol-gel process which is among the methods used for the production of  $UO_2$ ,  $ThO_2$  and  $ThO_2-UO_2$  mixed oxide fuel pellets allows a high degree of micro-homogeneity of uranium and thorium in the solution stage. The first aim of this study was to develop an alternative method to produce uranium, thorium and mixed thorium-uranium dioxide fuel pellets by using internal gelation technique of sol-gel process. The second aim was to investigate shrinkage behavior and first-stage sintering kinetics of pellets compacted in the Ar-%5  $H_2$  atmosphere using dilatometer. Shrinkage curves of the  $UO_2$ ,  $ThO_2$ ,  $ThO_2-10\%UO_2$  and  $ThO_2-5\%UO_2$  pellets obtained from the dilatometer were used to determine the sintering mechanism, the diffusion coefficients and the activation energy.

**Key Words:** Sol-gel, internal gelation, first-stage sintering, shrinkage, uranium, thorium, mixed oxide pellet.

## ÖZET

### SOL-GEL PROSESİNİN İÇ JELLEŞME TEKNİĞİ İLE ÜRETİLEN $UO_2$ , $ThO_2$ VE $(Th,U)O_2$ PELETLERİNİN BİRİNCİ SAFHA SİNERLEME KİNETİĞİNİN İNCELENMESİ

SÖKÜCÜ (ALTUNBAYRAK), Ayşe Sibel

Doktora Tezi, Fizik Mühendisliği Bölümü

Tez Yöneticisi: Prof. Dr. Metin BEDİR

Yardımcı Yönetici: Doç. Dr. M. Timuçin AYBERS

Aralık 2015

100 sayfa

$UO_2$ ,  $ThO_2$  ve  $ThO_2-UO_2$  karışık oksit peletlerinin üretimi için kullanılan yöntemler içerisinde sol-jel yöntemi, uranyum ve toryumu çözelti formunda kullanarak yüksek seviyede bir mikro-homojenlik sağlar. Bu çalışmanın ilk amacı; sol-jel prosesinin iç jelleşme tekniğini kullanarak uranyum, toryum ve karışık toryum-uranyum oksit yakıt peletleri üretiminde alternatif bir pelet üretim yöntemi geliştirmektir. İkinci amaç ise dilatometrede Ar-%5  $H_2$  atmosferinde peletlerin büzülme davranışı ve birinci safha sinterleme kinetiklerinin incelenmesidir. Dilatometreden elde edilmiş olan  $UO_2$ ,  $ThO_2$ ,  $ThO_2-10\%UO_2$  and  $ThO_2-5\%UO_2$  peletlerinin büzülme eğrileri kullanılarak sinterleme mekanizması, difüzyon katsayıları ve aktivasyon enerjileri hesaplanmıştır.

**Anahtar Kelimeler:** Sol-jel, iç jelleşme, birinci safha sinterleme, büzülme, uranyum, toryum, karışık oksit pelet.

*To my family...*



## ACKNOWLEDGEMENTS

I would like to express my sincere thanks to my advisor Prof.Dr.Metin BEDİR for his invaluable guidance and great support throughout this study. I would like to mention his excellent academic and individual approach to several subjects, which will give me motivation and inspiration for the rest of my life.

I would like to thank my co-supervisor Assoc. Prof. Dr. M. Timuçin AYBERS for all his help and advice during this thesis. I am truly grateful for the encouragement and consideration of him. It is now my privilege to thank him.

The author and supervisor would like to thank to the Reactor Materials Unit of the Çekmece Nuclear Research and Training Center for giving opportunity to do this study and the experiments.

I would like to thank my friends, researchers in the Reactor Materials Unit of the Çekmece Nuclear Research and Training Center, for their encouragement, suggestion, experience, patience and dear friendship.

Most importantly, none of this would have been possible without the love and patience of my family. I would like to thank my endless gratitude to my dear family.

## TABLE OF CONTENTS

	<b>Page</b>
ABSTRACT.....	i
ÖZET.....	ii
ACKNOWLEDGEMENT.....	iv
TABLE OF CONTENTS.....	v
LIST OF FIGURES.....	viii
LIST OF TABLES.....	xii
LIST OF SYMBOLS/ABBREVIATIONS.....	xiii
CHAPTER I.....	1
INTRODUCTION.....	1
1.1 Literature Survey.....	5
1.2 Scope of This Research Work.....	7
CHAPTER II.....	9
THEORY.....	9
2.1 Principles of Nuclear Reactors.....	9
2.1.1 Nuclear Fuel Cycle.....	10
2.2 Nuclear Fuels.....	11
2.2.1 Uranium.....	11
2.2.2 Thorium.....	13
2.3 Fuel Fabrication Process.....	16
2.4 Sol-Gel Process.....	17
2.4.1 General Flow Sheet of Sol-Gel Processes.....	18
2.4.2 Internal Gelation Process.....	19
2.4.3 Chemistry of Internal Gelation Process.....	20
2.5 Sintering Process.....	23
2.5.1 Sintering Variables.....	25
2.5.2 Material transport mechanisms of sintering.....	26

2.5.3 Stages of Sintering.....	28
2.5.4 Sintering Kinetics and Activation Energy.....	31
CHAPTER III.....	33
CHARACTERIZATION METHODS.....	33
3.1 Thermal Analysis Methods.....	33
3.1.1 Thermo Gravimetric Analysis (TGA).....	34
3.1.2 Differential Thermal Analysis (DTA).....	35
3.1.3 Dilatometry (DIL).....	35
3.2 Surface Analysis Method-BET.....	38
3.2.1 Adsorption Isotherm.....	39
3.3 Structure Analysis Method-XRD.....	40
CHAPTER IV.....	43
EXPERIMENTAL PROCEDURE.....	43
4.1 Initial Materials.....	43
4.2 Preparation of Gel Microspheres.....	44
4.2.1 Preparation of UO <sub>2</sub> Microspheres.....	44
4.2.2 Preparation of ThO <sub>2</sub> Microspheres.....	46
4.2.3 Preparation of (Th,U)O <sub>2</sub> Microspheres.....	47
4.3 Preparation of Green Pellets.....	48
4.4 Characterization.....	48
4.4.1 Thermogravimetry.....	49
4.4.2 BET.....	49
4.4.3 XRD.....	49
4.5 Sintering of the Green Pellets.....	50
CHAPTER V	
RESULTS and DISCUSSIONS.....	51
5.1 Investigation of TGA/DTA Curve by Thermogravimetry.....	51
5.1.1 TGA/DTA Curve of the UO <sub>2+x</sub> .....	51
5.1.2 TGA/DTA Curve of the ThO <sub>2</sub> .....	51
5.1.3 TGA/DTA Curve of the (Th,U)O <sub>2+x</sub> .....	52
5.2 Investigation of Specific Surface Area by BET Method.....	54
5.3 Investigation of Crystallite Size from XRD.....	56

5.3.1 Crystallite Sizes of $\text{UO}_{2+x}$ Powder.....	56
5.3.2 Crystallite Sizes of $\text{ThO}_2$ Powder.....	56
5.3.3 Crystallite Sizes of $(\text{Th,U})\text{O}_{2+x}$ Powders.....	59
5.4 Investigation of Sintering Kinetics and Activation Energy.....	65
5.4.1 Investigation for $\text{UO}_2$ Pellets.....	65
5.4.2 Investigation for $\text{ThO}_2$ Pellets.....	69
5.4.3 Investigation for $\text{ThO}_2$ -10% $\text{UO}_2$ Pellets.....	74
5.4.4 Investigation for $\text{ThO}_2$ -5% $\text{UO}_2$ Pellets.....	78
5.5 XRD Analysis of $\text{ThO}_2$ , $\text{ThO}_2$ -10% $\text{UO}_2$ and $\text{ThO}_2$ -5% $\text{UO}_2$ Pellets After Sintering in $\text{Ar}+5\% \text{H}_2$ Atmosphere.....	85
CHAPTER VI	
CONCLUSION.....	88
REFERENCES.....	93
CURRICULUM VITAE.....	101

## LIST OF FIGURES

	Page
<b>Figure 2.1</b> General flow sheet of the sol-gel processes for nuclear fuel microspheres.....	18
<b>Figure 2.2</b> The flow sheet for the internal gelation process.....	20
<b>Figure 2.3</b> Gelation field diagram of uranium.....	21
<b>Figure 2.4</b> Gelation field diagram for the preparation of thoria microspheres.....	23
<b>Figure 2.5</b> Six distinct mechanisms can contribute to the sintering of a consolidated mass of crystalline particles.....	26
<b>Figure 2.6</b> Idealized models for the three stages of sintering.....	29
<b>Figure 2.7</b> Examples of real microstructures (planar sections).....	29
<b>Figure 3.1</b> Schematic and measuring part of DIL 402 C.....	36
<b>Figure 3.2</b> Schematic of the adsorption of gas molecules onto the surface of a sample.....	38
<b>Figure 3.3</b> Schematic representation of XRD by regularly spaced planes of atoms in a crystal.....	41
<b>Figure 4.1</b> Flow sheet for the preparation of UO <sub>2</sub> , ThO <sub>2</sub> and (Th,U)O <sub>2</sub> pellets by internal gelation technique.....	43
<b>Figure 4.2</b> Pure Uranil Nitrate Crystal, HMTA+Urea and Uranly Nitrate solutions.....	44
<b>Figure 4.3</b> Forming microspheres.....	45
<b>Figure 4.4</b> Washing and dried UO <sub>3</sub> microspheres.....	45
<b>Figure 4.5</b> Dried and calcined ThO <sub>2</sub> microspheres.....	46
<b>Figure 4.6 (a)</b> UO <sub>2</sub> , <b>(b)</b> ThO <sub>2</sub> , <b>(c)</b> ThO <sub>2</sub> -10%UO <sub>2</sub> , and <b>(d)</b> ThO <sub>2</sub> -5%UO <sub>2</sub> pellets.....	48
<b>Figure 5.1</b> TGA/DTA curves of UO <sub>2+x</sub> .....	52
<b>Figure 5.2</b> TGA/DTA curves of ThO <sub>2</sub> .....	52

<b>Figure 5.3</b> TGA/DTA curves of ThO <sub>2</sub> -10%UO <sub>2+x</sub> .....	53
<b>Figure 5.4</b> TGA/DTA curves of ThO <sub>2</sub> -5%UO <sub>2+x</sub> .....	53
<b>Figure 5.5</b> BET plot of (a)UO <sub>2</sub> , (b)ThO <sub>2</sub> , (c)ThO <sub>2</sub> -10%UO <sub>2</sub> and (d) ThO <sub>2</sub> -5%UO <sub>2</sub> powders.....	55
<b>Figure 5.6</b> XRD of UO <sub>2</sub> powder prepared by the sol-gel method.....	57
<b>Figure 5.7</b> XRD of ThO <sub>2</sub> powder prepared by the sol-gel method.....	58
<b>Figure 5.8</b> XRD of ThO <sub>2</sub> -10%UO <sub>2</sub> powder prepared by the sol-gel method....	60
<b>Figure 5.9</b> XRD of ThO <sub>2</sub> -5%UO <sub>2</sub> powder prepared by the sol-gel method....	61
<b>Figure 5.10</b> XRD of ThO <sub>2</sub> , ThO <sub>2</sub> -10%UO <sub>2</sub> and ThO <sub>2</sub> -5%UO <sub>2</sub> powders.....	62
<b>Figure 5.11</b> X-Ray Diffraction patterns of UO <sub>2</sub> , ThO <sub>2</sub> , ThO <sub>2</sub> -10%UO <sub>2</sub> and ThO <sub>2</sub> -5%UO <sub>2</sub> powders.....	64
<b>Figure 5.12</b> Shrinkage curves of the UO <sub>2</sub> pellets in Ar+%5H <sub>2</sub> versus time and temperature sintered at 1300°C, 1200°C and 1100°C.....	66
<b>Figure 5.13</b> Shrinkage curves for UO <sub>2</sub> pellets in Ar+%5H <sub>2</sub> plotted against temperature.....	67
<b>Figure 5.14</b> Shrinkage rate $d(dL/L_o)/dt$ of UO <sub>2</sub> pellet in Ar+5%H <sub>2</sub> plotted against temperature, where $L_o$ is the initial length.....	67
<b>Figure 5.15</b> Diffusion mechanism of UO <sub>2</sub> in reducing Ar-%5H <sub>2</sub> atmosphere.	68
<b>Figure 5.16</b> The Arrhenius plot $\ln D$ versus $1/T$ for UO <sub>2</sub> pellet sintered in Ar+%5H <sub>2</sub> .....	69
<b>Figure 5.17(a)</b> Shrinkage curves of the ThO <sub>2</sub> pellets in Ar+%5H <sub>2</sub> versus time and temperature sintered at 1300°C and 1200°C.....	70
<b>Figure 5.17(b)</b> Shrinkage curves of the ThO <sub>2</sub> pellets in Ar+%5H <sub>2</sub> versus time and temperature sintered at 1100°C and 1000°C.....	71
<b>Figure 5.18</b> Shrinkage curves for ThO <sub>2</sub> pellets in Ar+%5H <sub>2</sub> versus temperature .....	72
<b>Figure 5.19</b> Shrinkage rate $d(dL/L_o)/dt$ of ThO <sub>2</sub> pellet in Ar+5%H <sub>2</sub> plotted against temperature, where $L_o$ is the initial length.....	73
<b>Figure 5.20</b> Diffusion mechanism of ThO <sub>2</sub> in reducing Ar-%5H <sub>2</sub> atmosphere.....	73
<b>Figure 5.21</b> The Arrhenius plot $\ln D$ versus $1/T$ for ThO <sub>2</sub> pellet sintered in Ar+%5H <sub>2</sub> .....	74

<b>Figure 5.22</b> Shrinkage curves of the ThO <sub>2</sub> -10%UO <sub>2</sub> pellets in Ar+%5H <sub>2</sub> versus time and temperature sintered at 1200°C, 1100°C and 1000°C.....	75
<b>Figure 5.23</b> Shrinkage curves for ThO <sub>2</sub> -10%UO <sub>2</sub> pellets in Ar+%5H <sub>2</sub> versus temperature .....	76
<b>Figure 5.24</b> Shrinkage rate $d(dL/L_o)/dt$ of ThO <sub>2</sub> -10%UO <sub>2</sub> pellet in Ar+5%H <sub>2</sub> plotted against temperature, where $L_o$ is the initial length.....	76
<b>Figure 5.25</b> Diffusion mechanism of ThO <sub>2</sub> -10%UO <sub>2</sub> in reducing Ar - %5 H <sub>2</sub> atmosphere.....	77
<b>Figure 5.26</b> The Arrhenius plot $\ln D$ versus $1/T$ for ThO <sub>2</sub> -10%UO <sub>2</sub> pellet sintered in Ar+%5H <sub>2</sub> .....	78
<b>Figure 5.27</b> Shrinkage curves of the ThO <sub>2</sub> -5%UO <sub>2</sub> pellets in Ar+%5H <sub>2</sub> versus time and temperature sintered at 1200°C, 1100°C and 1000°C.....	79
<b>Figure 5.28</b> Shrinkage curves for ThO <sub>2</sub> -5%UO <sub>2</sub> pellets in Ar+%5H <sub>2</sub> versus temperature .....	80
<b>Figure 5.29</b> Shrinkage rate $d(dL/L_o)/dt$ of ThO <sub>2</sub> -5%UO <sub>2</sub> pellet in Ar+5%H <sub>2</sub> plotted against temperature, where $L_o$ is the initial length.....	80
<b>Figure 5.30</b> Diffusion mechanism of ThO <sub>2</sub> -5%UO <sub>2</sub> in reducing Ar-%5H <sub>2</sub> atmosphere.....	81
<b>Figure 5.31</b> The Arrhenius plot $\ln D$ versus $1/T$ for ThO <sub>2</sub> -5%UO <sub>2</sub> pellet sintered in Ar+%5H <sub>2</sub> .....	82
<b>Figure 5.32</b> Shrinkage behaviour on heating in Ar+%5H <sub>2</sub> Atmosphere. Curves of UO <sub>2</sub> , ThO <sub>2</sub> , ThO <sub>2</sub> -10%UO <sub>2</sub> and ThO <sub>2</sub> -5%UO <sub>2</sub> are shown.....	83
<b>Figure 5.33</b> Shrinkage rate for UO <sub>2</sub> , ThO <sub>2</sub> , ThO <sub>2</sub> -10%UO <sub>2</sub> and ThO <sub>2</sub> -5%UO <sub>2</sub> pellets heated in Ar+%5H <sub>2</sub> Atmosphere plotted against temperature.....	83
<b>Figure 5.34</b> XRD patterns of the ThO <sub>2</sub> pellets sintered in Ar+%5H <sub>2</sub> atmosphere at 1300°C, 1200°C, 1100°C and 1000°C for 16 h.....	85

<b>Figure 5.35</b> XRD patterns of the ThO <sub>2</sub> -10%UO <sub>2</sub> sintered in Ar+5%H <sub>2</sub> atmosphere at 1000°C, 1100°C, 1200°C and 1300°C for 16 h.....	86
<b>Figure 5.36</b> XRD patterns of the ThO <sub>2</sub> -5%UO <sub>2</sub> pellets sintered in Ar+5%H <sub>2</sub> atmosphere at 1000°C, 1100°C, 1200 °C and 1300°C for 16 h.....	86
<b>Figure 5.37</b> XRD patterns of the ThO <sub>2</sub> , ThO <sub>2</sub> -10%UO <sub>2</sub> and ThO <sub>2</sub> -5%UO <sub>2</sub> pellets sintered in Ar+5%H <sub>2</sub> atmosphere at 1300°C for 16 h.....	87



## LIST OF TABLES

	<b>Page</b>
<b>Table 1.1</b> Power Reactors in Operation and Under Construction in the Worlds.....	3
<b>Table 2.1</b> Known Recoverable Resources of Uranium 2013.....	12
<b>Table 2.2</b> Estimated world thorium resources.....	14
<b>Table 2.3</b> Types and geometry of thorium-based fuels and fuel elements.....	16
<b>Table 2.4</b> Variables affecting sinterability and microstructure.....	25
<b>Table 2.5</b> Material transport mechanisms during sintering.....	27
<b>Table 2.6</b> Parameters Associated with the Stages of Sintering for Polycrystalline Solids.....	30
<b>Table 5.1</b> Parameters used for the calculation of specific surface area of the powders.....	54
<b>Table 5.2</b> Crystallite sizes of UO <sub>2</sub> powder calculated from XRD.....	59
<b>Table 5.3</b> Crystallite sizes of ThO <sub>2</sub> powder calculated from XRD.....	59
<b>Table 5.4</b> Crystallite sizes of ThO <sub>2</sub> -10%UO <sub>2</sub> powder calculated from XRD.....	63
<b>Table 5.5</b> Crystallite sizes of ThO <sub>2</sub> -5%UO <sub>2</sub> powder calculated from XRD.....	63
<b>Table 5.6</b> Characterization of the UO <sub>2</sub> , ThO <sub>2</sub> , ThO <sub>2</sub> -10%UO <sub>2</sub> and ThO <sub>2</sub> -5%UO <sub>2</sub> powders.....	65
<b>Table 5.7</b> The diffusion mechanism characteristics ( <i>A</i> , <i>n</i> and <i>p</i> ), diffusion coefficients and activation energy values of the sintered UO <sub>2</sub> , ThO <sub>2</sub> , ThO <sub>2</sub> -10%UO <sub>2</sub> and ThO <sub>2</sub> -5%UO <sub>2</sub> pellets.....	84

## LIST OF SYMBOLS/ABBREVIATION

TAEK	Turkish Atomic Energy Authority
IAEA	International Atomic Energy Agency
IEO	International Energy Outlook
BARC	Bhabha Atomic Research Centre
INIR	Integrated Nuclear Infrastructure Review
PRIS	Power Reactor Information System
PWR	Pressurized Water Reactor
BWR	Boiling Water Reactor
PHWR	Pressurized Heavy Water Reactor
AHWR	Advanced Heavy Water Reactor
GCR	Gas Cooled Reactor
LMFBR	Liquid Metal Fast Breeder Reactor
GCFBR	Gas Cooled Fast Breeder Reactor
HTGR	High Temperature Gas Cooled Reactor
WWER	Water-cooled Water-moderated power Reactor
MSBR	Molten Salt Breeder Reactor
MOX	Mixed Oxide Fuel
IGP	Internal Gelation Process
CAP	Coated Agglomerate Pelletization
$(\text{CH}_2)_6\text{N}_4$	HMTA (Hexa Methylene Tetra Amine)
$\text{CO}(\text{NH}_2)_2$	Urea

HMUR	HMTA/Urea solution
UNH	Uranyl Nitrate Hexahydrate
ADUN	Acid Deficient Uranyl Nitrate
Th(NO <sub>3</sub> ) <sub>4</sub>	Thorium Nitrate
CCl <sub>4</sub>	Carbon Tetra Chloride
NH <sub>3</sub>	Ammonia
TCE	Trichloro ethylene
HNO <sub>3</sub>	Nitric acid
XRD	X-ray diffraction
TEM	Transmission Electron Microscopy
SEM	Scanning Electron Microscopy
IR	Infrared spectroscopy
NMR	Nuclear Magnetic Resonance
XRF	X-ray Fluorescence
EDAX	Energy-Dispersive X-ray Analysis
DTA	Differential Thermal Analysis
TGA	Thermal Gravimetric Analysis
DSC	Differential Scanning Calorimetry
DIL	Dilatometry
BET	Surface Analysis Method
LVDT	Linear Variable Displacement Transducer
ICSD	Inorganic Crystal Structure Database
EGA	Evolved Gas Analysis
STP	Standard Temperature and Pressure
SC	Simple Cubic crystal structure
BCC	Body-Centred Cubic crystal structure

FCC	Face-Centred Cubic crystal structure
FWHM	Full Width at Half Maximum
B	Line full width at half maximum
$D_t$	Lattice diffusivity
$D_b$	Grain boundary diffusivity
$D_s$	Surface diffusivity
$D_g$	Gas diffusivity
$\eta$	Viscosity
$L_o$	Initial sample length at the start of sintering
$K(T)$	Arrhenius constant
$D$	Diffusion coefficient
$A, n$ and $p$	Constants whose values depend on the sintering mechanism
$r$	Particle radius
$\gamma$	Surface tension
$\Omega$	Vacancy volume
$k$	Boltzmann constant
$\alpha$	Coefficient of expansion
$\theta$	Fractional cover of the surface
P	Gas pressure
$X_m$	Monolayer capacity
$S_t$	Total surface area
$L_{av}$	Avogadro's number
C	Dimensionless constant related to energy of adsorption
$A_m$	Cross sectional area of the adsorbate
M	Molecular weight of adsorbate
$\lambda$	Wavelength of the radiation

d	Distance between two atomic planes
$\theta$	Angle between the planes and the incident X-ray beam
a	Lattice constant
h, k, l	Miller indices
t	Crystallite size

## CHAPTER I

### INTRODUCTION

The demand for energy is increasing in the world. Energy growth is directly linked to well-being and prosperity across the globe. Meeting the growing demand for energy in a safe and environmentally responsible manner is a key challenge for all economies. There are seven billion people on earth who use energy each day to make their lives richer, more productive, safer and healthier. It is perhaps the biggest driver of energy demand: the human desire to sustain and improve the well-being of ourselves, our families and our communities. Through 2040, population and economic growth will drive demand higher, but the world will use energy more efficiently and shift toward lower-carbon fuels.

Nuclear power is the most environmentally benign way of producing electricity on a large scale. Renewable energy sources such as solar and wind are costly per unit of output and are intermittent but can be helpful at the margin in providing clean power.

Fuel and operational costs for nuclear power are very low, making it more affordable than gas, wind, and solar power. And because most of the cost of nuclear power is derived from the construction of facilities, pricing is both stable and predictable.

Concern about clean air is a main reason that as of 31 December 2014, 70 reactors were under construction around the world [1]. Nuclear energy is by far the largest source of electricity that doesn't emit any air pollution and the only one that can produce large amounts of electricity around the clock.

There were 438 nuclear power reactors in operation worldwide, the total generating capacity of nuclear energy was 376.2 gigawatts-electric (GW(e)) at the end of 2014 (Table 1.1) [2]. During the year, there were five new grid connections, one permanently shut down and three construction starts on new reactors.

Nuclear reactors are classified as i) the pressurized water reactor (PWR), ii) the boiling water reactor (BWR), iii) the pressurized heavy water reactor (PHWR), iv) the gas cooled reactor (GCR), v) the liquid metal or gas cooled fast breeder reactor (LMFBR, GCFBR). This classification is based on the energy removal mechanism. Of the commercial reactors in operation, approximately 81.5% are light water moderated and cooled reactors; 11.2% are heavy water moderated and cooled reactors; 3.4% are light water cooled, graphite moderated reactors; and 3.4% are gas cooled reactors (GCRs). Two reactors are liquid metal cooled fast reactors.[1]

Turkey continues to develop its nuclear power programme infrastructure. In December 2014, the Ministry of Environment and Urban Planning approved the environmental impact assessment of the four proposed WWER-1200 units at Akkuyu. The Turkish regulatory body enlisted in October 2014 a technical support organization to assist with its review and assessment of the construction licence application for Akkuyu, expected to be submitted in 2015. Following an intergovernmental agreement signed with Japan in 2013, Turkey is also working on a second NPP project at Sinop and has started, in cooperation with its partners, site investigations and the preparation of a technical feasibility study.[1]

As of December 2015, 30 countries worldwide are operating 441 nuclear reactors for electricity generation and 65 new nuclear plants are under construction in 15 countries. [3]

In addition to commercial nuclear power plants, there are about 240 research reactors operating, in 56 countries, with more under construction. These have many uses including research and the production of medical and industrial isotopes, as well as for training.

**Table 1.1** Power Reactors in Operation and Under Construction in the Worlds (as of 31 December 2014) [4]

COUNTRY	Reactors in operation		Reactors under construction		Nuclear electricity supplied in 2014		Total operating experience through 2014	
	No. of units	Total MW(e)	No. of units	Total MW(e)	TW(e).h	% of total	Years	Mounths
Argentina	3	1627	1	25	5.3	4.1	73	2
Armenia	1	375			2.3	30.7	40	8
Belarus			2	2 218				
Belgium	7	5 927			32.1	47.5	268	7
Brazil	2	1 884	1	1 245	14.5	2.9	47	3
Bulgaria	2	1 926			15.0	31.8	157	3
Canada	19	13 500			98.6	16.8	674	6
China	23	19 007	26	25 756	123.8	2.4	181	7
Czech Republic	6	3 904			29.6	35.8	140	10
Finland	4	2 752	1	1 600	22.6	34.7	143	4
France	58	63 130	1	1 630	418.0	76.9	1 990	4
Germany	9	12 074			91.8	15.8	808	1
Hungary	4	1 889			14.8	53.6	118	2
India	21	5 308	6	3 907	33.2	3.5	418	6
Iran	1	915			3.7	1.5	3	4
Italy							80	8
Japan	48	42 388	2	2 650	0	0	1694	4
Kazakhstan							25	10
Korea	23	20 717	5	6 370	149.2	30.4	450	1
Lithuania							43	6
Mexico	2	1 330			9.3	5.6	45	11



**Table 1.1** Power Reactors in Operation and Under Construction in the Worlds (as of 31 December 2014) [4] (cont.)

COUNTRY	Reactors in operation		Reactors under construction		Nuclear electricity supplied in 2014		Total operating experience through 2014	
	No. of units	Total MW(e)	No. of units	Total MW(e)	TW(e).h	% of total	Years	Mounths
Netherlands	1	482			3.9	4.0	70	0
Pakistan	3	690	2	630	4.6	4.3	61	8
Romania	2	1 300			10.8	18.5	25	11
Russian Federation	34	24 654	9	7 371	169.1	18.6	1 157	3
Slovakia	4	1 814	2	880	14.4	56.8	152	7
Slovenia	1	688			6.1	37.3	33	3
South Africa	2	1 860			14.8	6.2	60	3
Spain	7	7 121			54.9	20.4	308	1
Sweden	10	9 470			62.3	41.5	422	6
Switzerland	5	3 333			26.5	37.9	199	11
Ukraine	15	13 107	2	1 900	83.1	49.4	443	6
United Arab Emirates			3	4 035				
United Kingdom	16	9 373			57.9	17.2	1 543	7
United States of America	99	98 639	5	5 633	798.6	19.5	4 012	4
<b>Total</b>	<b>438</b>	<b>376 216</b>	<b>70</b>	<b>68 450</b>	<b>2 410.4</b>		<b>16 096</b>	<b>10</b>

**Source:** Data are from the IAEA's Power Reactor Information System (PRIS), available at <http://www.iaea.org/pris>

**Note:** The total figures include the following data from Taiwan, China:

- Six units, 5032 MW(e), in operation; two units, 2600 MW(e), under construction;
  - 40.8 TW·h of nuclear electricity generation, representing 18.9% of the total electricity generated.
- 1 GW(e), or gigawatt (electric), equals one thousand million watts of electrical power.

Turkey has considered using its abundant thorium reserves (estimated at around 345,000 tonnes) as an alternative source of fuel. Turkish scientists have carried out work on thorium fuel cycles and fusion technology. Indeed, a paper published in 2003 assessed the feasibility of using a solvent-extraction process to reprocess thorium-based spent fuel, in anticipation of Turkey constructing a thorium-based high-temperature reactor. [5] TAEK officials speak of promoting energy security by relying on Turkey's abundant sources of thorium. Nevertheless it seems unlikely that this will be achievable in the short term, due to the intrinsic technical difficulties posed by the thorium fuel cycle, and the lack of experience of the processes involved, both in Turkey and internationally. The current technology in Turkey was more suitable for the use of uranium, although the use of thorium would be considered in the future. [6,7]

Turkey has extensive experience in certain nuclear areas, especially in research related to the front-end of the fuel cycle. Turkey's pilot nuclear-fuel-fabrication and conversion plant, the Nuclear Fuel Facility Unit, was built as part of a project of the Nuclear Facilities Department at Cekmece Nuclear Research and Training Centre (CNAEM) in 1977. Since 1986 it has operated a small-scale pilot facility for uranium purification, conversion to  $UO_2$  and the production of fuel pellets. In the late 1980s and early 1990s, the IAEA provided expert services to help improve the fuel-fabrication process at CNAEM. It is now possible for CNAEM staff to produce high-grade  $UO_2$  pellets, which they claim are of sufficient purity to be used in nuclear-fuel production. Under a technical cooperation project that started in 2007, the IAEA is helping Turkey upgrade its infrastructure for fabrication, characterization, and irradiation testing of uranium and thorium-based oxide fuels. [7,8]

### **1.1 Literature survey**

Thorium fuels and thorium fuel cycle options have been widely investigated in the past in Canada, Germany, India, the Russian Federation, UK and the USA and documented in several international conference proceedings and IAEA publications [9-32]. In recent years, there has been renewed interest in thorium fuel cycle mainly from the point of view of proliferation resistance and utilization of natural resources. [33,35].

In manufacturing the mixed oxide fuels like (Pu,U)O<sub>2</sub> and (Th,U)O<sub>2</sub>, the homogeneous distribution of the constituent metals is an important point to be studied, since it relates to the safety and reliability of the fuel [36-40]. The requirement for high homogeneity of the distribution of the actinides in the fuel is also essential for most of new generation (Gen IV) reactors. Traditionally, (Th,U)O<sub>2</sub> pellets are made by powder metallurgy technique consisting of blending of ThO<sub>2</sub> and UO<sub>2</sub> powders followed by milling, compaction and sintering in reducing atmosphere at around 1700 °C [41,42]. The key step in the production of the above mixed oxide fuels is the preparation of homogeneous oxide mixtures [40]. The presence of fissile rich regions in a pellet affects the fuel performance since they act as hot spots generating high temperatures and releasing more fission gases [43,44].

Generally, the large scale production of MOX fuel pellets is carried out by sintering the green compacts in a reducing atmosphere at high temperatures around 1700 °C [41,42]. However, when the fabrication of fuels containing highly radioactive materials, such as <sup>233</sup>U, americium, curium, long-lived fission products or transmutation nuclides is considered, the production of dust and consequent radiation exposure to personnel could restrict the use of the above usual process consisting of co-milling, cold compaction and sintering.

Therefore, alternative fabrication routes that are more amenable for remotization and automation procedures are being considered [45-48]. Some of the promising methods other than powder pellet route are (a) sol-gel microsphere pelletization (b) vibro-sol route and (c) impregnation technique [9].

Thorium fuel cycle contributes to produce long term nuclear energy with a small amount of radiotoxic waste. The fuel not only reduces plutonium production but also reduces the formation of highly radioactive isotopes [49-53]. Regarding to waste management, the Th containing fuel creates more <sup>129</sup>I and <sup>234</sup>U due to higher amount of <sup>233</sup>U in it. However, the U fuel forms more <sup>99</sup>Tc, <sup>237</sup>Np and <sup>239</sup>Pu and some heavier actinides [27,54].

Sintering is an important process for the nuclear fuel; various reports on sintering of UO<sub>2</sub> are available in the literature [55-62]. The sintering kinetics of UO<sub>2</sub> during initial stages have been studied by several workers. Layand Carter [58] has found out the sintering mechanism to be volume diffusion of uranium ion, whereas Bacmann

and Cizeron [60] and Woolfrey [59] have suggested that to be grain boundary diffusion. The activation energies for initial stages of sintering, reported by different workers varies in a wide range from 84 kJ/mol [62] to 420 kJ/mol [61]. Sintering kinetics of (Th,U)O<sub>2</sub> has been also studied by several authors[63-67]. Three different compositions of (Th,U)O<sub>2</sub> pellets fabricated by Coated Agglomerate Pelletization (CAP) process were studied on sintering kinetics using master sintering curve approach [66]. Recently, activation energy for sintering of ThO<sub>2</sub> was determined to be 370±20 kJ/mol by Clavier et al [63]. Although initial stage sintering of ThO<sub>2</sub> and UO<sub>2</sub> alone has been investigated in detail, but article on study of sintering kinetics of mixed oxides (Th,U)O<sub>2</sub> are limited. The densification behavior of ThO<sub>2</sub> containing 2%U<sub>3</sub>O<sub>8</sub> pellet, prepared by powder metallurgy technique, was evaluated using a temperature dilatometer at various atmospheres [68]. The densification behavior of ThO<sub>2</sub>-2%UO<sub>2</sub> and ThO<sub>2</sub>-4%UO<sub>2</sub> pellets, fabricated by impregnation technique, was evaluated using high temperature dilatometry in the atmospheres of Ar-8%H<sub>2</sub> and air [69]. Recently, sintering kinetics and activation energy of ThO<sub>2</sub>-4%UO<sub>2</sub> pellet, fabricated by CAP process, has been studied using vertical dilatometer at different heating rate [70]. Further, apparent activation energy and diffusion coefficients at initial-stage of (Th<sub>0.2</sub>,U<sub>0.8</sub>)O<sub>2</sub> have been investigated under oxidizing and reducing atmosphere to demonstrate that activation energy is lower in oxidizing atmosphere as compared to reducing one [71]. Activation energies for the rest ThO<sub>2</sub> and the compositions of 5%, 20% and 80% UO<sub>2</sub> are reported to be 283.8 kJ/mol, 315.7 kJ/mol and 294.7 kJ/mol in oxidizing atmosphere; and 263.3 kJ/mol, 478.8 kJ/mol and 326 kJ/mol in reducing atmosphere [72]. On the other hand, no systematic trend on the values of activation energy with increasing UO<sub>2</sub> content could be established from that study.

## **1.2 Scope of This Research Work**

Fuel pellets are usually fabricated by conventional powder metallurgy technique. Large-scale production of these pellets are carried out by the process of cold compaction followed by high temperature sintering in reducing atmosphere so as to attain pellet density close to its theoretical value. This study seeks to develop an alternative method to produce thorium, uranium and mixed thorium-uranium dioxide fuel pellets which are prepared by internal gelation technique of sol-gel process. The

sol-gel method which is among the methods used for the production of ThO<sub>2</sub>-UO<sub>2</sub> mixed oxide fuel pellets allows a high degree of micro-homogeneity of uranium and thorium in the solution stage.

This study further aims to investigate shrinkage behavior and first-stage sintering kinetics of pellets compacted in the Ar-%5 H<sub>2</sub> atmosphere by using dilatometer. Sintering is an important step in the processing of ceramic nuclear fuel involving micro-structural evolution by densification through several different transport mechanisms. During the first-stage sintering, solid particles in contact are bonded together and the aggregate shrinks resulting in a decrease of surface area and energy. The neck formation, the neck growth and shrinkage take place by the material transport. The determination of the first-stage sintering kinetics parameters is not only important in determining the properties of the end product but have also fascinated the powder technologists ever since they have started contending with science of sintering. Therefore it is very important to determine the sintering kinetics parameters. Various methods have been used to study the determination of sintering mechanism. Among these, dilatometric studies of the kinetics of isothermal shrinkage of powder compacts have been particularly useful they allow one continuously to follow dimensional variation in the same sample. In the study, dilatometric curves are used to determine the sintering mechanism, the diffusion coefficients and the activation energy.

## CHAPTER II

### THEORY

#### 2.1 Principles of Nuclear Reactors

Nuclear reactors generate electricity like any other steam-electric power plant. Water is heated, and steam from the boiling water turns turbines and generates electricity. The main difference in the various types of steam-electric plants is the heat source. Heat from a self-sustaining chain reaction boils the water in a nuclear power plant. Coal, oil, or gas is burned in other power plants to heat the water.

Despite the many possible differences in design, there are the basic parts of a reactor which are the core, a moderator, control rods, a coolant, and shielding.

- The central part of a nuclear reactor is an active core in which the fission chain reaction is sustained. The **core** of a reactor contains the uranium fuel. For a light water reactor with an output of 1,000 megawatts, the core would contain about 75 tonnes of uranium enclosed in approximately 200 fuel assemblies.
- The **moderator**, which decreases the speed of fast neutrons, is usually carbon in the form of graphite and water. Slower neutrons are much more likely to cause fission and keep the reaction going.
- **Control rods** containing a neutron absorber, such as boron that can be inserted into the core of the nuclear, provide more precise control of the chain reaction. Pushed in, they absorb neutrons and slow down the reaction – pulled out they allow it to speed up again.
- A liquid or gas used as **coolant** to transfer the enormous heat generated by fission away from the reactor to a boiler where steam is made.
- **Shielding**, typically made of steel and concrete about two meters thick, is an outer casing that prevents the escape of radiation to the environment.

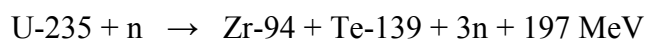
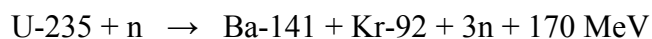
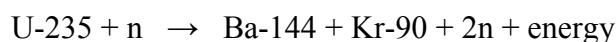
### 2.1.1 Nuclear Fuel Cycle

Nuclear Fuel Cycle can be defined as the set of processes to make use of nuclear materials and to return it to normal state. It starts with the mining of unused nuclear materials from the nature and ends with the safe disposal of used nuclear material in the nature.

To produce energy from Uranium in a nuclear reactor, it must be passed through in a series of different processes. The complete set of processes to make nuclear fuel from uranium ore is known as *front end of the nuclear fuel cycle*. The processes in the front end of the nuclear cycle are mining and milling, conversion, enrichment and fuel fabrication. After producing energy in the reactor, nuclear fuel becomes spent fuel. Spent fuel has also to be processed in a storage facility or in a reprocessing facility if it is being recycled. Temporary storage, reprocessing, long-term storage, or final storage of spent fuel are together called *back end of the nuclear fuel cycle*. If spent fuel is not reprocessed, the fuel cycle is referred to as an *open fuel cycle* (or a *once-through fuel cycle*); if the spent fuel is reprocessed, it is referred to as a *closed fuel cycle*.

Neutrons in motion are the starting point for everything that happens in a nuclear reactor. When a neutron passes near to a heavy nucleus, for example uranium-235 (U-235), the neutron may be captured by the nucleus and this may or may not be followed by fission. [41] Other relatively common heavy nuclei that are fissile (implying thermal fission) are U-233, Pu-239 and Pu-241. Each of these is produced artificially in a nuclear reactor, from the fertile nuclei Th-232, U-238 and Pu-240 respectively. U-235 is the only naturally occurring isotope which is thermally fissile, and it is present in natural uranium at a concentration of 0.7 percent. U-238 and Th-232 are the main naturally-occurring fertile isotopes.

The fission reaction in U-235 produces fission products such as Ba, Kr, Sr, Cs, I and Xe with atomic masses distributed around 95 and 135. Examples may be given of typical reaction products, such as:



In such an equation, the number of nucleons (protons + neutrons) is conserved but a small loss in atomic mass may be shown to be equivalent to the energy released. Both the barium and krypton isotopes subsequently decay and form more stable isotopes of neodymium and yttrium, with the emission of several electrons from the nucleus (beta decays). It is the beta decays, with some associated gamma rays, which make the fission products highly radioactive. This radioactivity decreases with time.

The chain reaction that takes place in the core of a nuclear reactor is controlled by rods which absorb neutrons and which can be inserted or withdrawn to set the reactor at the required power level. The fuel elements are surrounded by a substance called a moderator to slow the speed of the emitted neutrons and thus enable the chain reaction to continue. Water, graphite and heavy water are used as moderators in different types of reactors. [73]

## **2.2 Nuclear Fuels**

### **2.2.1 Uranium**

Uranium was discovered by Martin Klaproth, a German chemist, in 1789 in the mineral pitchblende, and was named after the planet Uranus. Hahn, Meitner and Strassmann reported fission of uranium (U-235) in 1939. Uranium is the basic material for nuclear energy and the heaviest elements occurring in nature. Like other elements, uranium occurs in slightly differing forms known as isotopes. These isotopes differ from each other in the number of neutron particles in the nucleus. Natural uranium as found in the Earth's crust is a mixture of three isotopes: uranium-238 (U-238), accounting for 99.275%; U-235 – 0.720%; and traces of U-234 – 0.005%.

The isotope U-235 is important because under certain conditions it can readily be split, yielding a lot of energy. It is therefore said to be 'fissile' and we use the expression 'nuclear fission'. During the fission two or three neutrons are thrown off. If enough of these expelled neutrons are captured by the nuclei of other U-235 atoms to split, releasing further neutrons, a fission 'chain reaction' occurs. When this happens over and over again, many millions of times, a very large amount of heat is produced from a relatively small amount of uranium. [73]



The following Table 2.1 gives some idea of our present knowledge of uranium resources.

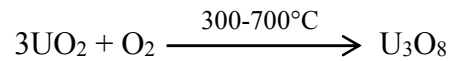
**Table 2.1** Known Recoverable Resources of Uranium 2013[74]

	<b>tonnes U</b>	<b>percentage of world</b>
<b>Australia</b>	1,706,100	29%
<b>Kazakhstan</b>	679,300	12%
<b>Russia</b>	505,900	9%
<b>Canada</b>	493,900	8%
<b>Niger</b>	404,900	7%
<b>Namibia</b>	382,800	6%
<b>South Africa</b>	338,100	6%
<b>Brazil</b>	276,100	5%
<b>USA</b>	207,400	4%
<b>China</b>	199,100	4%
<b>Mongolia</b>	141,500	2%
<b>Ukraine</b>	117,700	2%
<b>Uzbekistan</b>	91,300	2%
<b>Botswana</b>	68,800	1%
<b>Tanzania</b>	58,500	1%
<b>Jordan</b>	33,800	1%
<b>other</b>	191,500	3%
<b>World total</b>	<b>5,902,500</b>	

Reasonably Assured Resources plus Inferred Resources, to US\$ 130/kg U, 1/1/13, from OECD NEA & IAEA, *Uranium 2013: Resources, Production and Demand* ("Red Book"). The total to US\$ 260/kg U is 7.635 million tonnes U, and Namibia moves up ahead of Niger and USA ranks just after Canada.

The uranium dioxide (UO<sub>2</sub>) is the most common composition of uranium when used as reactor fuel around the world. It is a non-stoichiometric oxide exhibiting high reactivity with oxygen or air. It can be readily oxidized to U<sub>3</sub>O<sub>8</sub> through a two-step reaction. In order to achieve uranium dioxide pellets complying with the specification, besides oxygen to uranium stoichiometric ratio (O/U ratio), the original powders must hold a set of several determinate properties, such as surface area, bulk and tap densities, water and impurities content, powder flowability, etc. [75]

UO<sub>2</sub> is stable, one of three prevalent, uranium oxides that is present in the inventory. Considering the following reaction, in an oxidizing atmosphere, starting from 300°C, UO<sub>2</sub> can be oxidized to form U<sub>3</sub>O<sub>8</sub> [76,77]



The rate of this reaction is a function of particle size, and the temperature requirement will change accordingly.

### 2.2.2 Thorium

Thorium is a naturally-occurring, slightly radioactive metal discovered in 1828 by the Norwegian mineralogist Morten Thrane Esmark and identified by the Swedish chemist Jöns Jakob Berzelius, who named it after Thor, the Norse god of thunder. It is found in small amounts in most rocks and soils, where it is about three times more abundant than uranium. Soil commonly contains an average of around 6 parts per million (ppm) of thorium. The most common being the rare earth-thorium-phosphate mineral, monazite, which contains up to about 12% thorium oxide, but average 6-7%. Soil commonly contains an average of around 6 ppm (parts per million) of [78]; others [79] reported that thorium content of soil as much as 10 ppm.

Unlike natural uranium, which contains ~0.7% ‘fissile’ <sup>235</sup>U isotope, natural thorium does not contain any ‘fissile’ material and is made up of the ‘fertile’ <sup>232</sup>Th isotope only. Hence, thorium and thorium-based fuel as metal, oxide or carbide, has been utilized in combination with ‘fissile’ <sup>235</sup>U or <sup>239</sup>Pu in nuclear research and power reactors for conversion to ‘fissile’ <sup>233</sup>U, thereby enlarging the ‘fissile’ material resources.

In a fast reactor or thermal reactor, the fertile isotope <sup>232</sup>Th is bombarded by slow neutrons, undergoing neutron capture to become <sup>233</sup>Th. This normally emits an electron and an anti-neutrino (ν) by β<sup>-</sup> decay to become <sup>233</sup>Pa. This then emits another electron and anti-neutrino by a second β<sup>-</sup> decay to become <sup>233</sup>U, the fuel:



**Table 2.2** Estimated world thorium resources [80]

<b>Country</b>	<b>Tonnes</b>
<b>India</b>	846,000
<b>Brazil</b>	632,000
<b>Australia</b>	595,000
<b>USA</b>	595,000
<b>Egypt</b>	380,000
<b>Turkey</b>	374,000
<b>Venezuela</b>	300,000
<b>Canada</b>	172,000
<b>Russia</b>	155,000
<b>South Africa</b>	148,000
<b>China</b>	100,000
<b>Norway</b>	87,000
<b>Greenland</b>	86,000
<b>Finland</b>	60,000
<b>Sweden</b>	50,000
<b>Kazakhstan</b>	50,000
<b>Other countries</b>	1,725,000
<b>World total</b>	<b>6,355,000</b>

Thorium fuels and fuel cycles are particularly relevant to countries having large thorium deposits but very limited uranium reserves for their long term nuclear power programme. Thorium cycles are feasible in all existing thermal and fast reactors, e.g. light water reactors, heavy water reactors, high temperature gas reactors, sodium-cooled fast reactors, and molten salt reactors. In the short term, it should be possible to incorporate the thorium fuel cycle in some of the above existing reactors without major modifications in the engineered systems, reactor control and the reactivity devices. However, for the innovative reactors and fuel cycles, a lot of reactor physics studies and other technological developments would be required before these could be implemented.

Thorium fuel cycles offer attractive features, including lower levels of waste generation, less transuranic elements in that waste, and providing a diversification option for nuclear fuel supply. Also, the use of thorium in most reactor types leads to extra safety margins. Despite these merits, the commercialization of thorium fuels

faces some significant hurdles in terms of building an economic case to undertake the necessary development work.

Large scale utilization of thorium for nuclear power is possible only with the introduction of an additional step of first converting the ‘fertile’  $^{232}\text{Th}$  into the ‘fissile’  $^{233}\text{U}$ . The subsequent use of  $^{233}\text{U}$  is conceivable in the following ways:

- ‘Open’ fuel cycle based on irradiation of  $^{232}\text{Th}$  and in situ fission of  $^{233}\text{U}$ , without involving chemical separation of  $^{233}\text{U}$ .
- ‘Closed’ fuel cycle based on chemical reprocessing of irradiated thorium or thorium based fuels for recovery of  $^{233}\text{U}$  and refabrication and recycling of  $^{233}\text{U}$  bearing fuels.

All commercial power reactors in operation today are reliant on the uranium-plutonium (U-Pu) fuel cycle, in which  $^{235}\text{U}$  is the principal fissile nuclide providing the fission neutrons needed to maintain criticality and power output. The thorium fuel cycle is an alternative to uranium-plutonium. Thorium is widespread in the Earth’s crust and is known to occur in economically accessible deposits in many locations. Natural thorium is made up entirely of the isotope  $^{232}\text{Th}$ , which is fertile, but not fissile. When irradiated by neutrons,  $^{232}\text{Th}$  is converted to  $^{233}\text{U}$ , which is fissile. In principle, if there are sufficient spare neutrons from uranium fuelled reactor available, useful quantities of  $^{233}\text{U}$  can be produced by irradiating  $^{232}\text{Th}$ . The  $^{233}\text{U}$  can then either fission in situ in the fuel, increasing its useful energy output, or is separated and recycled into new fuel. This is the basis of the thorium fuel cycle.

There is a big diversity of thorium-based nuclear fuels and fuel elements depending on the type of reactor. Except for the molten salt breeder reactor (MSBR), which uses mixed fluoride in liquid form as fuel and primary coolant, all other reactors use solid fuels in the form of tiny “ceramic fuel microspheres” (100–1000  $\mu$ ), “ceramic fuel pellets” or “metallic alloy fuel rods”. Table 2.3 summarizes the thorium-based fuel and fuel elements used in experimental and power reactors.

**Table 2.3** Types and geometry of thorium-based fuels and fuel elements [9]

REACTOR TYPE	COMPOSITION	FUEL SHAPE	FUEL ELEMENT
<b>High temperature Gas cooled reactors</b>	ThO <sub>2</sub> , (Th,U)O <sub>2</sub> , ThC <sub>2</sub> , (Th,U)C <sub>2</sub> ( <sup>235</sup> U or <sup>233</sup> U)	Microspheres 200-800 μ coated with multiple layer of buffer & pyrolytic carbon and SiC	Mixed with graphite and pressed into large spheres (~60 mm) for Pebble-Bed Reactor or fuel rods for HTGRs with prismatic fuel elements
<b>Light water reactors</b>	ThO <sub>2</sub> , (Th,U)O <sub>2</sub> , (Th,Pu)O <sub>2</sub> (<5%Pu, <sup>235</sup> U or <sup>233</sup> U)	<ul style="list-style-type: none"> <li>• High-density Sintered Pellets</li> <li>• High-density Microspheres</li> </ul>	<ul style="list-style-type: none"> <li>• Zircaloy clad Pin Cluster encapsulating Pellet-Stack</li> <li>• Zircaloy clad ‘vipac’ Pin Cluster encapsulating fuel microspheres</li> </ul>
<b>Heavy water reactors</b>			
<b>PHWR</b>	ThO <sub>2</sub> for neutron flux flattening or initial core		
<b>AHWR</b>	(Th,U)O <sub>2</sub> , (Th,Pu)O <sub>2</sub> (<5%Pu, <sup>235</sup> U or <sup>233</sup> U)	High-density Sintered Pellets	Zircaloy clad Pin Cluster encapsulating Pellet-Stack
<b>Fast reactors</b>	<ul style="list-style-type: none"> <li>• ThO<sub>2</sub> blanket</li> <li>• (Th,U)O<sub>2</sub> &amp; (Th,Pu)O<sub>2</sub> (&lt;5%Pu, <sup>235</sup>U or <sup>233</sup>U)</li> <li>• Th metal blanket</li> <li>• Th-U-Zr &amp; Th-U-Pu-Zr fuels</li> </ul>	High-density Sintered Pellets  Injection-cast Fuel Rods	Stainless steel (SS) clad Pin Cluster encapsulating Pellet-Stack  SS clad Pin Cluster encapsulating Fuel Rods
<b>Molten salt breeder reactor</b>	Li <sup>7</sup> F+BeF <sub>2</sub> +ThF <sub>4</sub> +UF <sub>4</sub>	Molten salt liquid form	Circulating molten salt acting as fuel and primary coolant

### 2.3 Fuel Fabrication Processes

The essential steps of conventional ‘powder-pellet’ route are co-milling of oxide powders, granulation, cold pelletization and sintering. The ‘powder pellet’ route is suitable for fabrication of high-density fuel pellets but has the disadvantage of ‘radiotoxic dust hazard’ as it involves handling of fine fuel particles. Further, fine powders have poor flowability, which makes automation and remote fabrication somewhat difficult. The alternative ‘vibro sol’ or ‘sphere pac’ process involves preparation of dust-free and free flowing sol gel derived fuel microspheres, which after high temperature treatment produces very high-density fuel microspheres.

The following processes are being developed for the fabrication of thoria and thoria based fuel pellets:

(1) **‘Powder-pellet’ route**: for preparation of high density fuel pellets, using ThO<sub>2</sub>, UO<sub>2</sub> and PuO<sub>2</sub> powders as starting materials; the fuel pellet stacks are encapsulated in cladding tubes.

(2) **‘Vibro-sol’ route**: for preparation of fuel microspheres using nitrate solutions of uranium, plutonium and thorium as starting materials and adapting ‘ammonia external gelation’ or ‘ammonia internal gelation’ process for obtaining hydrated gel microspheres; the microspheres are sintered and vibro packed in cladding tubes followed by encapsulation.

(3) **‘Sol-gel microsphere pelletization’**: using dust-free and free-flowing sol gel derived oxide fuel microspheres for direct pelletization and sintering.

(4) **‘Impregnation technique’**: where (a) partially sintered ThO<sub>2</sub> pellets of relatively low density ( $\leq 75\%$  theoretical density) or (b) ‘porous’ ThO<sub>2</sub> microspheres are vacuum impregnated in uranyl nitrate (‘U’ as <sup>233</sup>U) or Pu–nitrate solution followed by calcination and sintering to form high density ThO<sub>2</sub>-based mixed oxide fuel pellets, which are encapsulated in cladding tubes.

## 2.4 Sol-Gel Process

The sol-gel process involving the transition of a solution system from a liquid "sol" into a solid "gel" phase is a versatile solution process for making advanced materials. The processes have been developed for the fabrication of nuclear fuel materials, i.e. the oxides, carbides and nitrides of uranium, plutonium and thorium as well as their solid solutions. Development of solution based fuel fabrication processes for the production of Th-<sup>233</sup>U fuels dates back to the early sixties. Solution based routes were first investigated for the production of (Th-<sup>233</sup>U) oxide-based spherical coated particle fuels for the high temperature gas cooled reactors (HTGR).

The sol-gel processes provide the following advantages over the conventional powder pellet making route. The sol-gel process

- (i) uses only sol/solutions and eliminates handling of radioactive powders containing U, Pu.
- (ii) requires handling of fluids and fluid-like microspheres. The transfers of fluids are much simpler than that of powders of fuel materials. Therefore, sol-gel process is more easily amenable to remote handling.

- (iii) can use the nitrate solutions of the fuel materials like uranium and plutonium or thorium from the reprocessing plants as the feed which reduces the number of process steps such as actinide oxalate precipitation, conversion to actinide oxides etc. involving powder handling.

The disadvantages of the sol-gel processes are:

- (i) Large amount of liquid waste is produced
- (ii) Large amount of irradiation experience is available around the world for the pellet fuels and their irradiation behaviour is well established, but the irradiation experience for sphere-pac fuel is very limited.

#### 2.4.1 General Flow Sheet of Sol-Gel Processes

There are many sol-gel process routes that have been developed by countries having fuel development programme for nuclear fuel fabrication. Generalized flow sheet common to these processes is given in Figure 2.1. The temperature differs from process to process and also with the type of material, hence they are not mentioned in the flow sheet. Droplets of the sol/solution of the fuel material are generated and then these droplets are converted into hard gel particles by the gelation process. Afterwards, the gel particles are washed, dried, calcined and sintered into high density fuel microspheres.

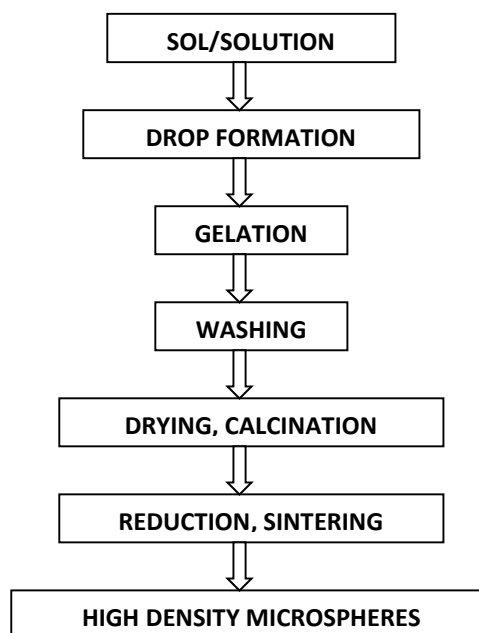


**Figure 2.1** General flow sheet of the sol-gel processes for nuclear fuel microspheres

## 2.4.2 Internal Gelation Process

Internal Gelation Process (IGP) is one of the most important routes of the sol–gel process and has been accepted as the most promising process route globally because of its simplicity and ability to control the properties of final product. The IGP was developed for the production of  $\text{UO}_2$  microspheres by Kanij et al. [81] and Bruggens et al. [82] at KEMA laboratories, Netherlands in 1967. The flow sheet for the internal gelation process is shown in Figure 2.2.

In IGP, the solutions of the nitrates of uranium, thorium and plutonium or their desired mixtures are used to make gel microspheres. Metal nitrate solutions are cooled and then mixed with  $\text{CO}(\text{NH}_2)_2$  urea and  $(\text{CH}_2)_6\text{N}_4$  alias HMTA (hexamethylenetetramine) solution in cooled condition. The droplets of the solution are allowed to fall in a hot oil to provide the heating. Since the ammonia donor and the heavy metal ions are dissolved in the same solution, gelation occurs rapidly and nearly uniformly throughout the drop typical of a homogeneous precipitation. These gel microspheres are washed first with  $\text{CCl}_4$  to remove the silicone oil and then with ammonia solution to remove excess gelation agents HMTA, Urea and ammonium nitrate. The washed particles are dried in air and then calcined to remove residual organic matter and ammonium nitrate and finally reduced.

Concerning urania microspheres, preparation of Acid Deficient Uranyl Nitrate (ADUN) solution with a  $\text{NO}_3^-/\text{UO}_2^{2+}$  mole ratio of 1.5–1.7 is the first step of the flow sheet, as it has higher solubility in water. It is done in one of the following ways: One of the following ways can be used to pre-neutralize of Uranyl Nitrate solution:

1. addition of  $\text{UO}_3$  to a sub-stoichiometric amount of nitric acid ( $\text{HNO}_3$ ) or to a stoichiometric solution of uranyl nitrate.
2. addition of  $\text{U}_3\text{O}_8$  to a sub-stoichiometric amount of  $\text{HNO}_3$ .
3. addition of  $\text{UO}_2$  to a sub-stoichiometric amount of  $\text{HNO}_3$ .
4. amine extraction of acid from uranyl nitrate solution.



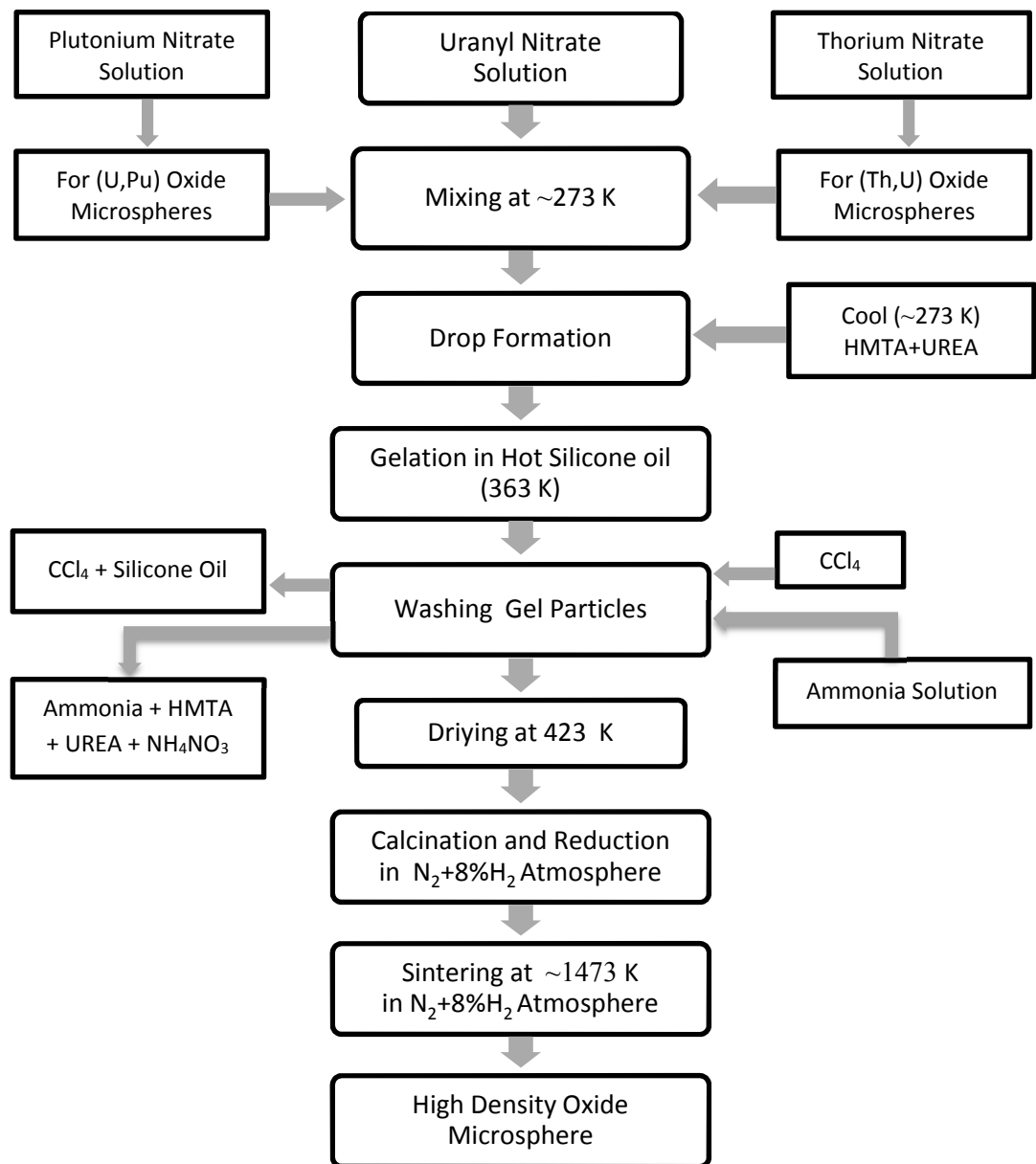


**Figure 2.2** The flow sheet for the internal gelation process [83]

### 2.4.3 Chemistry of Internal Gelation Process

The ADUN solutions require aeration for 24 h to remove  $\text{NO}_2$  dissolved in the broth. A 3 M solution of ADUN thus prepared is mixed with a 3 M HMTA/Urea solution (known as HMUR) in the ratio 1:1.4. Under these acidic conditions, HMTA hydrolyses to form ammonia and formaldehyde which leads to premature gelation. The presence of urea helps to complex the uranyl ion to prevent hydrolysis at low temperature with ammonia. Collins et al. [84] have explained the mechanism of the

gelation sequence. The feed solution is cooled to 273–272 K to reduce the rate of decomposition of HMTA and to increase the stability of the uranyl-urea complex. So broth preparation is carried out by mixing cold uranyl nitrate solution with cold HMUR solution. Although gelation has been reported to occur over a wide range of solution compositions (uranium molarity from 0.7 to 1.6) and a range of molar ratios of HMUR to Uranium 0.75–2.3, the window of operating parameters become narrower for making hard, opaque gels which behave well in the subsequent steps to result in good quality, crack-free hard microspheres. Detailed studies carried out at Bhabha Atomic Research Centre (BARC) Mumbai, India have resulted in the gelation field diagram shown in Figure 2.3 [85] for the preparation of urania microspheres. Feed compositions from the gelation field diagram resulting in hard, opaque gel are suitable for making very good quality  $UO_2$  microspheres which can withstand washing, drying, reduction and sintering procedures with a very small (1%) process loss.

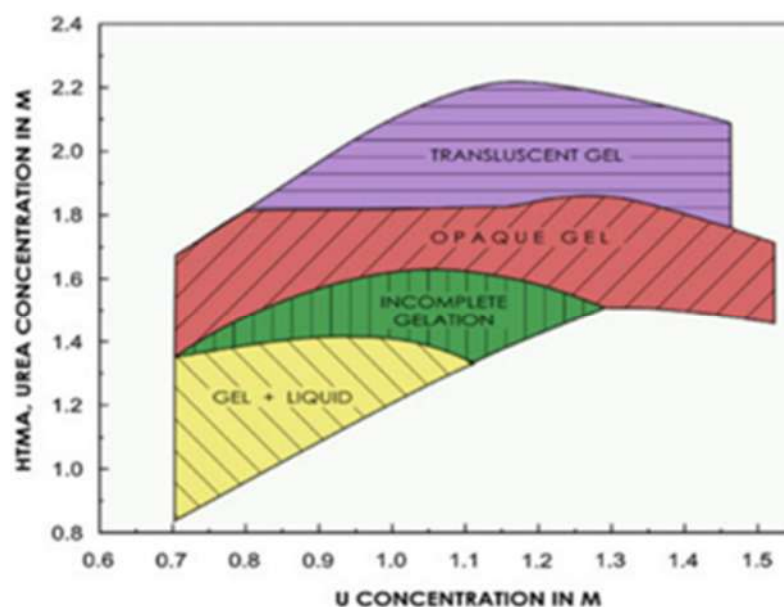
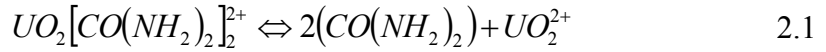


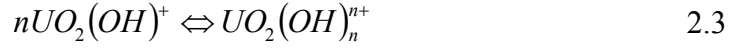
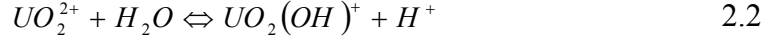
**Figure 2.3** Gelation field diagram of uranium

In the feed solution made by mixing the ADUN with HMUR, the pH varies between 3.5 and 6 depending on the  $NO_3/U$  ratio and uranium precipitation occurs above a Ph of 3.25. When the droplets of the broth are introduced in the hot silicone oil, the following reactions occur which control the extent of gelation. The following key reactions are important in the chemistry of the internal gelation process.

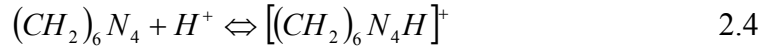
At first, temperature-induced decomplexation of ADUN-urea complex occurs.



Then the metal ion gets hydrolyzed to release hydrogen ion



HMTA gets protonated consuming this hydrogen ion:



The decomposition of HMTA occurs through



Reactions (2.1) to (2.3) are the initiating reactions for the gelation. Since all these reactions are highly temperature dependent and the degree of acid deficiency affects the total concentration of hydrogen ion produced during hydrolysis, temperature and acid deficiency greatly influence the gelation process. Further, the neutralising effect of reaction (2.4) or (2.5) to form the metal ion polymer,  $(UO_2(OH)_n)^{n+}$  is governed by the HMUR/U ratio. At large HMUR/U ratios, the protonation reaction (2.4), which is ionic in nature and hence very fast, is involved in the hydrolysis. The fast kinetics does not allow the crystallites to grow and the resultant gel is transparent or translucent. The gels formed with lower molar ratio of HMUR/U are predominantly formed by the relatively slower reaction (2.5) resulting in the large crystallites and opaque gel. The variation of crystallite size as function of composition has been reported by Lloyd et al. [86]. The gels formed with lower molar ratio of HMTA/U in the solution are predominantly formed by reaction (2.5) and thus the crystallites of the polymer are allowed to grow because of slow kinetics. These variations are clearly seen in the gelation field diagrams [85,87] for urania and thoria gels as shown in Figure 2.3 and Figure 2.4, respectively.

Washing is an important step in the internal gelation process. Washing is done at first with an organic solvent like  $CCl_4$  or trichloro ethylene (TCE) to remove the organics and then with ammonia to remove the urea and ammonium nitrate ensuring that the pH is at or above 8.5. Incompletely washed spheres fail during the subsequent steps. Opaque gels are easier to wash than transparent or translucent gels.

Drying is done in air between room temperature and 425 K in an oven or in a belt drier in a continuous mode. Different calcination conditions have been used by different laboratories. Generally, after drying calcination is done at 773–823 K in air. For urania microspheres, reduction is carried out at 823–873 K to form  $\text{UO}_2$  followed by sintering under reducing atmosphere at 1473–1523 K. Reduction step is not required for preparing thorium microspheres.

Studies have also been carried out in many countries on the preparation of thorium oxide and  $(\text{U,Th})\text{O}_2$  microspheres. A large number of studies have been carried out in India on these systems and Kumar et al. [87] have reported the gelation field diagram for thorium system shown in Figure 2.4.

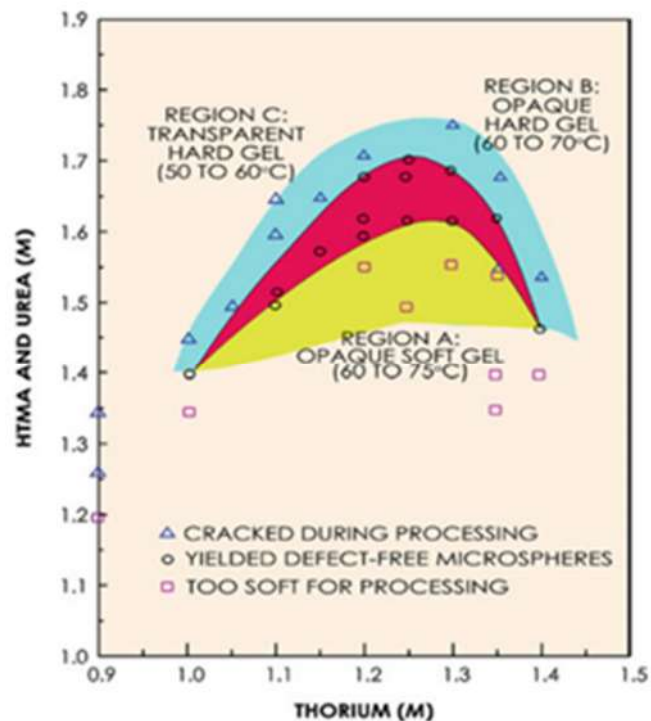


**Figure 2.4** Gelation field diagram for the preparation of thorium microspheres

## 2.5 Sintering Process

Sintering is the thermal treatment of a powder or compact at a temperature below the melting point of the main constituent until its particles adhere to each other. The purpose of sintering is to increase its strength by welding together of the particles.

The definition by Thummler [88] from the point of view of physical chemistry is: ‘Sintering is a thermally activated mass transport process which leads to strengthening of particle contacts and/or a change in porosity and pore geometry

accompanied by a reduction of the free energy. A liquid phase can take part in the process'.

Sintering is actually one of the oldest human technologies, originating in the prehistoric era with the firing of pottery. The production of tools from sponge iron was also made possible by sintering. Nonetheless, it was only after the 1940s that sintering was studied essentially and scientifically. Since then, remarkable developments in sintering science have been made. One of the most essential and beneficial uses of sintering in the modern era is the fabrication of sintered parts of all kinds, including powder-metallurgical parts and bulk ceramic components. [89]

The sintering process is the phenomenon on which the entire field of powder metallurgy is based. Excess surface energy contained in the mass of the powder particles, and the presence of lattice defect in the crystalline state provide the driving force to ensure the coalescence of these solid particles in contact. Shortly, the sintering is the growth of contact interface between powder particles in the solid state under appropriate conditions of time, temperature and atmosphere.

During sintering process:

- Atomic diffusion takes place and the welded areas formed during compaction grow until eventually they may be lost completely.
- Recrystallisation and grain growth may follow, and the pores tend to become rounded and the total porosity, as a percentage of the whole volume tends to decrease.
- In the pressing operation the powder particles are brought together and deformed at the points of contact.
- At elevated temperature, the sintering temperature, the atoms can move more easily and quickly migrate along the particle surfaces (the technical term is Diffusion).
- At the sintering temperature new crystallites form at the points of contact so that the original inter-particle boundaries disappear, or become recognizable merely as grain boundaries (This process is called Recrystallisation).
- The total internal surface area of the pressed body is reduced by sintering.
- Neck-like junctions are formed between adjacent particles as can be seen on the adjoining scanning electron micrograph.

### 2.5.1 Sintering Variables

The major variables which determine the sintered microstructure and sinterability of a powder compact may be divided into two categories. These categories are material variables and process variables (Table 2.4). The variables related to raw materials (material variables) include chemical composition and impurity of powder compact, degree of powder agglomeration, powder shape, powder size and powder size distribution, etc. These variables influence the powder compressibility and sinterability (densification and grain growth). In particular, for compacts containing more than two kinds of powders, the homogeneity of the powder mixture is of prime importance. To improve the homogeneity, not only mechanical milling but also chemical processing, such as sol-gel and coprecipitation processes, have been investigated and utilized.

**Table 2.4** Variables affecting sinterability and microstructure [89]

<b>Variables related to raw materials</b> (material variables)	<b>Powder:</b> shape, size, size distribution, agglomeration, mixedness, etc. <b>Chemistry:</b> composition, impurity, non- stoichiometry, homogeneity, etc.
<b>Variables related to sintering materials</b> (process variables)	Temperature, time, pressure, atmosphere, heating and cooling rate, etc.

The other variables involved in sintering are mostly thermodynamic variables, such as temperature, time, atmosphere, pressure, heating and cooling rate. Many previous sintering studies have examined the effects of sintering temperature and time on sinterability of powder compacts. It appears, however, that in real processing, the effects of sintering atmosphere and pressure are much more complicated and important. Unconventional processes controlling these variables have also been intensively studied and developed. [89]

## 2.5.2 Material transport mechanisms of sintering

Sintering of polycrystalline materials occurs by diffusional transport of matter along definite paths which define the *mechanisms of sintering*. In polycrystalline materials, there are at least six different mechanisms of sintering as shown schematically in Figure 2.5 for a system of three sintering particles. The strength of the powder compact increases during sintering since they all lead to bonding and growth of necks between the particles. Only certain mechanisms, however, lead to shrinkage or densification, and a distinction is commonly made between *densifying* and *nondensifying* mechanisms.

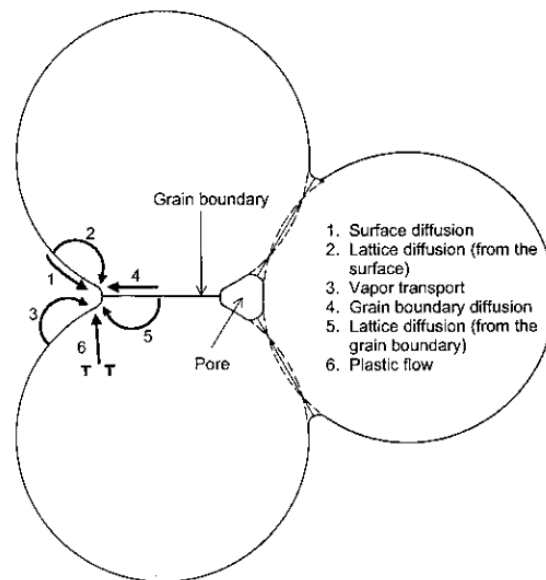


**Figure 2.5** Six distinct mechanisms can contribute to the sintering of a consolidated mass of crystalline particles: (1) surface diffusion, (2) lattice diffusion from the particle surfaces to the neck, (3) vapor transport, (4) grain boundary diffusion, (5) lattice diffusion from the grain boundary, and (6) plastic flow

Surface diffusion, lattice diffusion (volume diffusion) from the particle surfaces to the neck, and vapor transport lead to neck growth without densification and are referred to as nondensifying mechanisms (mechanisms 1, 2, and 3). Grain boundary diffusion and lattice diffusion from the grain boundary to the pore are the most important densifying mechanisms in polycrystalline ceramics (mechanisms 4 and 5). Diffusion from the grain boundary to the pore permits neck growth as well as densification. Plastic flow by dislocation motion also leads to neck growth and densification but is more common in the sintering of metal powders (mechanism 6).

The nondensifying mechanisms cannot simply be ignored because when they occur, they reduce the curvature of the neck surface and so reduce the rate of the densifying mechanisms. [90] Only mechanisms 1 to 3 lead to densification, but all cause the necks to grow and so influence the rate of densification.

The major mechanisms of material transport and their related parameters are listed in Table 2.5. The material transport due to the difference in interface curvature occurs under the parallel actions of various mechanisms. The dominant mechanism, however, can vary depending on, i.e., particle size, neck radius, temperature and time for a given system.

Some of these material transport mechanisms contribute to densification and shrinkage while others do not. The interparticle distance can be reduced only by bulk material flow via viscous flow or by material transport from the grain boundary via atom movement. When material comes to the neck from the particle surface, interparticle distance is not reduced but the neck size is increased by redistribution of material. Therefore, the grain boundary is the source of material transport for densification and shrinkage in crystalline powder compacts. [90,91]

**Table 2.5** Material transport mechanisms during sintering[89]

<b>Material transport mechanism</b>	<b>Material source</b>	<b>Material sink</b>	<b>Related parameter</b>
1. Lattice diffusion	Grain boundary	Neck	Lattice diffusivity, $D_t$
2. Grain boundary diffusion	Grain boundary	Neck	Grain boundary diffusivity, $D_b$
3. Viscous flow	Bulk grain	Neck	Viscosity, $\eta$
4. Surface diffusion	Grain surface	Neck	Surface diffusivity, $D_s$
5. Lattice diffusion	Grain surface	Neck	Lattice diffusivity, $D_t$
6. Gas phase transport			
6.1. Evaporation/Condensation	Grain surface	Neck	Vapour pressure difference, $\Delta p$
6.2. Gas diffusion	Grain surface	Neck	Gas diffusivity, $D_g$



### 2.5.3 Stages of Sintering

Sintering is ordinarily thought to occur in three consecutive stages referred to as (1) the *initial* stage, (2) the *intermediate* stage, and (3) the *final* stage. In some analyses of sintering, an extra stage, stage 0, is considered which define the instantaneous contact between the particles, when they are first brought together due to elastic deformation in response to surface energy reduction at the interface [92]. Figure 2.6 shows the idealized geometrical structures that were suggested by Coble [93] as representative of the three stages for polycrystalline materials. The geometrical models assumed for the intermediate and final stages are very different from those for the polycrystalline case for amorphous materials. [90]

#### **Initial Stage**

The initial stage consists of considerably rapid interparticle neck growth by diffusion, vapor transport, plastic flow, or viscous flow. In this stage, the large initial differences in surface curvature are removed, and densification (or shrinkage) accompanies neck growth for the densifying mechanisms. For a powder system consisting of spherical particles, the transition between Figures 2.6(a) and 2.6(b) represents the initial stage. For a powder system with an initial density of 0.5–0.6 of the theoretical density, this corresponds to a linear shrinkage of 3 to 5 % or an increase in density to  $\sim 0.65$  of the theoretical when the densifying mechanisms dominate.

#### **Intermediate Stage**

When the pores have reached their equilibrium shapes, the intermediate stage begins as dictated by the surface and interfacial tensions. The pore phase is still continuous. In the sintering models, the structure is generally idealized in terms of a spaghetti-like array of porosity sitting along the grain edges as illustrated in Figure 2.6(c). Densification is assumed to occur by the pores simply shrinking to reduce their cross section. Consequently, the pores become unstable and pinch off, leaving isolated pores; this constitutes the beginning of the final stage. The intermediate stage normally covers the major part of the sintering process, and when the density is  $\sim 0.9$  of the theoretical, it is taken to end.

## Final Stage

The microstructure in the final stage can develop in a variety of ways. In one of the simplest descriptions as shown by the idealized structure in Figure 2.6(d), the final stage begins when the pores pinch off and become isolated at the grain corners. In this simple description, the pores are assumed to shrink continuously and may disappear altogether.

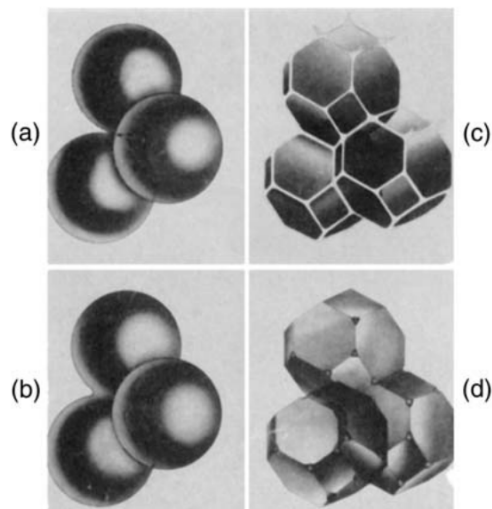


**Figure 2.6** Idealized models for the three stages of sintering. (a) Initial stage: Model structure represented by spheres in tangential contact. (b) Near the end of the initial stage: Spheres have begun to coalesce. The neck growth illustrated is for center-to-center shrinkage of 4%. (c) Intermediate stage: Dark grains have adopted the shape of a tetrakaidecahedron, enclosing white pore channels at the grain edges. (d) Final stage: Pores are tetrahedral inclusions at the corners where four tetrakaidecahedra meet. [93]

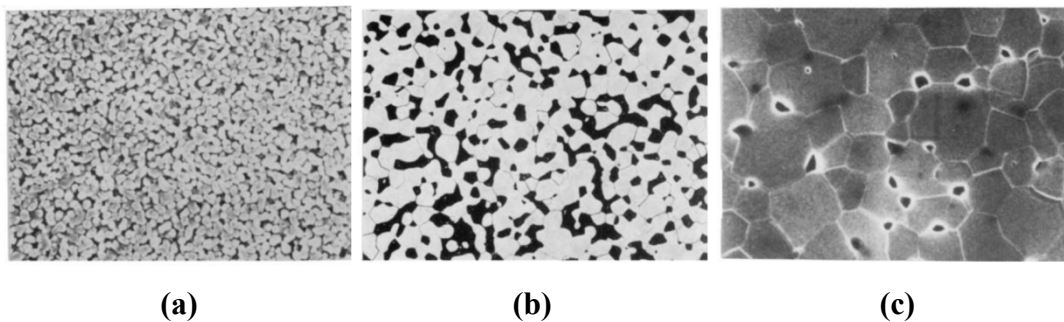


**Figure 2.7** Examples of real microstructures (planar sections) for (a) initial stage of sintering, (b) intermediate stage, and (c) final stage.

The removal of almost all of the porosity has been achieved in the sintering of several real powder systems. In Table 2.6, some of the main parameters associated with the three idealized stages of sintering are summarized, and examples of the microstructures (planar section) of real powder compacts in the initial, intermediate, and final stages are shown in Figure 2.7.

**Table 2.6** Parameters Associated with the Stages of Sintering for Polycrystalline Solids [90]

<b>Stage</b>	<b>Typical microstructural feature</b>	<b>Relative density range</b>	<b>Idealized model</b>
<b>Initial</b>	Rapid inter-particle neck growth	Up to ~0.65	Two monosize spheres in contact
<b>Intermediate</b>	Equilibrium pore shape with continuous porosity	~0.65-0.90	Tetrakaidecahedron with cylindrical pores of the same radius along the edges
<b>Final</b>	Equilibrium pore shape with isolated porosity	>~0.90	Tetrakaidecahedron with spherical monosize pores at the corners

In these sintering stages, the most important is the first-stage. During this stage solid particles in contact are bonded together and the aggregate shrinks resulting in a decrease of surface area and energy. A method of isolating the initial stage of the process is to employ small spheres of the same diameter touching each other. The neck growth and shrinkage take place by the material transport. Various types of material transport including viscous flow, plastic flow, evaporation-condensation, surface diffusion, grain-boundary diffusion and volume diffusion may occur during the sintering. All of these mechanisms may produce neck growth. But, only grain-boundary and volume diffusion are capable of producing shrinkage.

Various methods have been used to study the determination of sintering mechanism. Among these, dilatometric studies of the kinetics of isothermal shrinkage of powder compacts have been particularly useful because they allow one continuously to follow dimensional variation in the same sample.

#### 2.5.4 Sintering Kinetics and Activation Energy

The mechanism of material movement in sintering are not only important in determining the properties of the end product but have also fascinated the powder technologists ever since they have started contending with the science of sintering. Therefore, it is very important to determine the sintering kinetic parameters.

The kinetic equations of first-stage sintering have been derived by many investigators [94-96], who have based their considerations on the contact geometries and on material transport mechanisms. According to Bannister [97], the general equation for isothermal initial-stage sintering is given in equation 2.6.

The experimental shrinkage curves obtained generally follow an equation of the form:

$$\Delta L/L_o = Y = [K(T)t]^n, \quad 2.6$$

where

$$K(T) = A\gamma\Omega D / kTr^p. \quad 2.7$$

In this equation:  $L_o$  is the initial sample length at the start of sintering,  $K(T)$  is Arrhenius constant,  $D$  is the diffusion coefficient ( $\text{cm}^2/\text{s}$ ),  $r$  is the particle radius (cm),  $\gamma$  is the surface tension ( $\text{erg}/\text{cm}^2$ ),  $\Omega$  is the vacancy volume ( $\text{cm}^3$ ),  $A$ ,  $n$ ,  $p$  are the constants whose values depend on the sintering mechanism and  $k$  is the Boltzmann constant.

It is very difficult to determine the origin of the curve since the sample will not reach the isothermal temperature immediately. Following the time and shrinkage correction Eq. (2.6) became [98]:

$$Y+Y_o = K^n(t+ t_o)^n \quad (t_o \ll 0). \quad 2.8$$

Differentiation form of the equation gives the following:

$$dY/dt = \dot{Y} = n K^n t^{n-1}. \quad 2.9$$

$\dot{Y}$  can be calculated from experimental data. With plotting  $\log \dot{Y}$  versus  $\log t$  a straight line (slope:  $n-1$ ) will be obtained for each isothermal temperature. The value of  $n$  (determination of sintering mechanism) can be determined from the slope of this line and  $K(T)$  from the intercept with  $\log \dot{Y}$  axis. When  $K(T)$  is known the diffusion coefficient can be calculated from Eq. (2.7).

From the variation of  $\log D$  versus  $1/T$  the expression is as follows

$$D = D_o \exp -(Q / RT) \quad 2.10$$

where  $D_o$  is the preexponential factor of Arrhenius equation and  $Q$  is the activation energy and  $R$  is the molar gas constant.

The apparent activation energy is calculated from the slope of the variation of  $\ln D$  versus  $1/T$  (a straight line). The slope of the plot of  $\ln D$  and  $1/T$  gives the  $-Q/R$ .  $R$  being a constant of value  $8.31441 \text{ J K}^{-1} \text{ mol}^{-1}$ ,  $Q$  is determined from the slope of the plot.

## CHAPTER III

### CHARACTERIZATION METHODS

After the process of synthesis, it is necessary to obtain a thorough characterization of the materials. If we do not understand its composition, structure, and morphology, it is almost impossible to understand the properties of a material and, consequently, its proper application [99].

The most important rule of material characterization is to apply numerous methods, because only one methodology generally does not bring about a complete understanding of the material. In order to thoroughly characterize a material, various procedures are applied. Among them include x-ray diffraction (XRD), transmission electron microscopy (TEM), scanning electron microscopy (SEM), infrared (IR) and Raman spectroscopy, nuclear magnetic resonance (NMR), x-ray fluorescence (XRF) and energy-dispersive x-ray analysis (EDAX). To supplement these characterization methodologies, thermal methods are also usually applied, for example, differential thermal analysis (DTA), thermal gravimetric analysis (TGA), differential scanning calorimetry (DSC), dilatometry (DIL) and adsorption methods (BET).

#### 3.1 Thermal Analysis Methods

Thermal analysis techniques involve the measurement of various properties of materials subjected to dynamically changing environments under previously determined condition of heating rate, temperature range and gaseous atmosphere or vacuum. The most widely used techniques are TGA, DTA and DIL, which are employed in inorganic and organic chemistry, metallurgy, mineralogy and other areas.

In certain cases, the use of a single thermo analytical technique may not provide sufficient information to solve the problem on hand and hence the use of other thermal techniques, either independently or simultaneously, for complementary information becomes necessary. For example, both differential thermal analysis

(DTA) and thermo gravimetric analysis (TGA) are widely used in studies involving physicochemical changes accompanied by variation in the heat content and the weight of the material, and Dilatometer (DIL) is a technique by which the dimensional changes of the sample are monitored as a function of temperature or time.

### **3.1.1 Thermo Gravimetric Analysis (TGA)**

TGA is an analytical technique in which the mass of a substance is measured as a function of temperature or time while the sample specimen is subjected to a controlled temperature program in a controlled atmosphere.

The null-point weighing mechanism is employed since the sample remains in the same zone of furnace irrespective of changes in mass. The furnace is normally an electrical resistive heater and the temperature range for most of the furnace is from ambient to 1000-2000°C. The rate of heat exchange between the furnace and the sample depends on the heating rate which influences the TG curve in a number of ways. A slower rate gives a better resolution of the closely lying steps, while the faster heating rate merges such steps. The shape of thermogravimetric curve of a particular compound is influenced by the heating rate of the sample and the atmosphere surrounding it.

If the identity of the product after heating is known, then the ceramic yield can be found from analysis of the ash content. By taking the weight of the known product and dividing it by the initial mass of the starting material, the mass percentage of all inclusions can be found. Knowing the mass of the starting material and the total mass of inclusions, such as ligands, structural defects, or side-products of reaction, which are liberated upon heating, the stoichiometric ratio can be used to calculate the percent mass of the substance in a sample. [100]

Applications of TGA

- Study thermal degradation / decomposition / dehydration.
- Chemical reaction resulting in changes of mass such as absorption, adsorption, desorption.
- To check the sample purity.

### **3.1.2 Differential Thermal Analysis (DTA)**

DTA is a technique in which the temperature difference between a substance and a reference material is measured as a function of temperature whilst the substance and reference material are subjected to a controlled temperature program [101]. DTA provides information on the chemical reactions, phase transformations, and structural changes that occur in a sample during a heat-up or a cool-down cycle. The DTA measures the differences in energies released or absorbed, and the changes in heat capacity of materials as a function of temperature. The graph of DTA signal, i.e. differential thermocouple output in micro volts on the Y-axis plotted versus the sample temperature in °C on the X-axis gives the results of DTA.

Modern thermo-balances are often equipped so as to record the DTA signal and the actual thermo-gravimetric measurement, simultaneously. In addition to showing the energetic nature of weight loss events, the DTA signal can also show thermal effects that are not accompanied by a change in mass, e.g. melting, crystallization or a glass transition. Transition temperatures are measured precisely using the DTA.

Application of DTA

- Primarily used for detection of transition temperature.
- To check the sample purity.

### **3.1.3 Dilatometry (DIL)**

Dilatometry is a thermo-analytical technique used to measure dimensional changes of a specimen brought about by changes in its thermal environment. Typical measurements include thermal expansion, annealing studies, determination of phase transitions and the glass transition, softening points, kinetics studies, construction of phase diagrams and sintering studies, including the determination of sintering temperature, sintering step and rate-controlled sintering.

Dilatometry can be applied not only to solid samples, but also to powders, pastes, and even liquids. It can also be used to carry out ratecontrolled sintering studies on reactive powders in fields such as advanced ceramics or powder metallurgy.

Due to large technological advances, this thermal analysis method can now measure even the slightest of thermal behaviors in ceramics. Recent innovations in



dilatometer hardware and software design promise to augment the possibilities provided by thermal expansion measurement.

The Dilatometer (DIL 402 C), shown in Figure 3.1, has an Invar measurement system with a high-resolution measurement transducer and comprehensive thermostatic control, offering the highest degree of accuracy, reproducibility and long-term stability for application temperatures up to 1650°C.

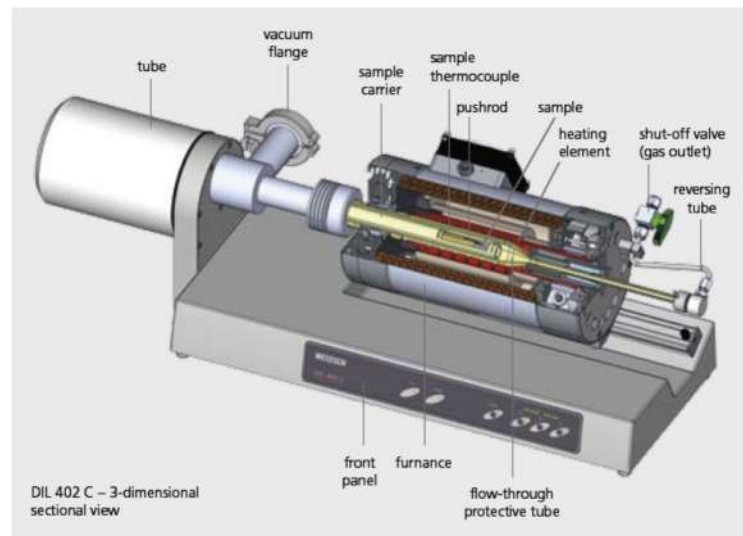


**Figure 3.1** Schematic and measuring part of DIL 402 C

### Method and Principle of Operation

Pushrod dilatometry is a method for determining dimensional changes versus temperature or time while the sample undergoes a controlled temperature program. The degree of expansion divided by the change in temperature is called the material's coefficient of expansion ( $\alpha$ ) and generally varies with temperature.

$$\alpha = \frac{1}{L_0} \left( \frac{\Delta l}{\Delta T} \right) \quad (3.1)$$

In this equation,  $\alpha$  is coefficient of expansion,  $L_0$  is initial sample length,  $\Delta T$  is change in temperature and  $\Delta l$  is change in length.

To perform a dilatometric analysis, a sample is inserted into a special holder within a movable furnace. A pushrod is positioned directly against the sample and transmits the length change to a linear variable displacement transducer (LVDT).

As the sample length changes during the temperature program, the LVDT core is moved, and an output signal proportional to the displacement is recorded. The temperature program is controlled using a thermocouple located either next to the heating element of the furnace or next to the sample.

Since the sample holder and the front part of the pushrod are being exposed to the same temperature program as the sample, they are also expanding. The resulting dilatometer signal is therefore the sum of the length changes of sample, sample holder, and pushrod.

It is thus necessary to correct the raw dilatometer data in order to obtain a true view of sample behavior. There are two correction methods: the application of tabulated expansion data, or – often more precise – of a correction curve to eliminate systematic error.

### **Advantage of a Horizontal Pushrod Dilatometer**

The superior thermal uniformity of a horizontal pushrod dilatometer can be attributed to very low temperature gradients. A horizontal furnace is not subject to convection parallel with the sample. Particularly for long samples, a horizontal dilatometer system is essential in ensuring that the temperature distribution is reasonably uniform.

The Characteristics of DIL 402 C are wide temperature range, 6 exchangeable furnaces, vacuum-tight by design, large sample dimensions, adjustable contact pressure, extremely low drift and high resolution, various accessories for special applications, coupling to evolved gas analysis (EGA).

### **Atmosphere – High Vacuum**

The vacuum-tight design of the DIL 402 C allows for careful control of the atmosphere and pure gas conditions. For example, the system can be evacuated and back-filled with pure inert or non-reactive gas. Static or dynamic reactive gas atmospheres can be applied as well. Materials sensitive to oxygen can be studied under pure inert gas conditions.

### 3.2 Surface Analysis Method-BET

Brunauer, Emmett and Teller (BET) theory aims to explain the physical adsorption of gas molecules on a solid surface and serves as the basis for an important analysis technique for the measurement of the specific surface area of a material. In 1938, Stephen Brunauer, Paul Hugh Emmett, and Edward Teller published the first article about the BET theory in the Journal of the American Chemical Society.[102] The specific surface area of a powder is determined by calculating the amount of adsorbate gas usually non-corrosive (like nitrogen, Ar, CO<sub>2</sub> etc.) corresponding to a mono molecular layer on the surface. Physical adsorption results from the relatively weak forces (van der Waals) between the adsorbate gas molecules and the adsorbent surface area of the test powder. The determination is usually carried out at the temperature of liquid nitrogen. The amount of gas adsorbed can be measured by a volumetric or continuous flow procedure.

The concept of the BET theory was an extension of the Langmuir theory, developed by Irving Langmuir in 1916, which relates the monolayer adsorption of gas molecules (Figure 3.2) adsorbates onto a solid surface to the gas pressure of a medium above the solid surface at a fixed temperature to Equation 3.2, where  $\theta$  is the fractional cover of the surface,  $P$  is the gas pressure and  $\alpha$  is a constant.

$$\theta = \frac{\alpha \cdot P}{1 + (\alpha \cdot P)} \quad (3.2)$$

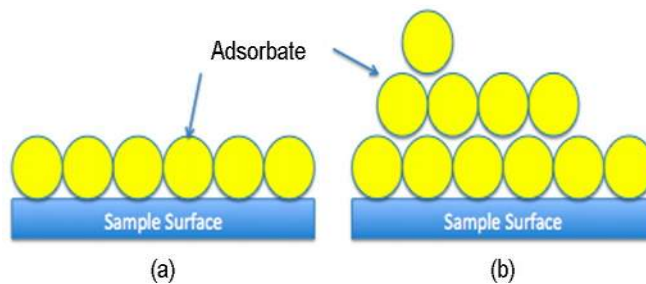


**Figure 3.2** Schematic of the adsorption of gas molecules onto the surface of a sample showing (a) the monolayer adsorption model assumed by the Langmuir theory and (b) the multilayer adsorption model assumed by the BET theory [103]

### 3.2.1 Adsorption isotherm

When a gas comes in contact with a solid surface, under suitable conditions of temperature and pressure, the concentration of the gas (the adsorbate) is always found to be greater near the surface (the adsorbent) than in the bulk of the gas phase. This process is known adsorption. The amount of gas adsorbed depends on the exposed surface area but also on the temperature, gas pressure and strength of interaction between the gas and solid.

In BET surface area analysis, nitrogen is usually used because of its availability in high purity and its strong interaction with most solids. Because the interaction between gaseous and solid phases is usually weak, the surface is cooled using liquid N<sub>2</sub> to obtain detectable amounts of adsorption. Known amounts of nitrogen gas are then released stepwise into the sample cell. Relative pressures less than atmospheric pressure is achieved by creating conditions of partial vacuum. After the saturation pressure, no more adsorption occurs regardless of any further increase in pressure. Highly precise and accurate pressure transducers monitor the pressure changes due to the adsorption process. After the adsorption layers are formed, the sample is removed from the nitrogen atmosphere and heated to cause the adsorbed nitrogen to be released from the material and quantified. The data collected is displayed in the form of a BET isotherm, which plots the amount of gas adsorbed as a function of the relative pressure. [104-106]

The BET equation, Equation 3.3, uses the information from the isotherm to determine the surface area of the sample, where X is the weight of nitrogen adsorbed at a given relative pressure (P/P<sub>0</sub>), X<sub>m</sub> is monolayer capacity, which is the volume of gas adsorbed at standard temperature and pressure (STP), and C is constant related to energy of adsorption. STP is defined as 273 K and 1 atm.

$$\frac{1}{X \left[ \left( \frac{P_0}{P} \right) - 1 \right]} = \frac{1}{X_m C} + \frac{C-1}{X_m C} \left( \frac{P}{P_0} \right) \quad (3.3)$$

$$y = b + m x$$

Ideally five data points, with a minimum of three data points, in the P/P<sub>0</sub> range 0.025 to 0.30 should be used to successfully determine the surface area using the BET equation. At relative pressures higher than 0.5, there is the onset of capillary

condensation, and at relative pressures that are too low, only monolayer formation is occurring. When the BET equation is plotted, the graph should be of linear with a positive slope. If such a graph is not obtained, then the BET method was insufficient in obtaining the surface area. The monolayer capacity  $X_m$  can be calculated with Equation 3.4.

$$X_m = \frac{1}{s+i} = \frac{c-1}{c_s} \quad (3.4)$$

Once  $X_m$  is determined, the total surface area  $S_t$  can be calculated with the following equation, where  $L_{av}$  is Avogadro's number,  $A_m$  is the cross sectional area of the adsorbate (nitrogen) and equals  $0.162 \text{ nm}^2$  for an adsorbed nitrogen molecule, and  $M$  is the molecular weight of adsorbate (nitrogen) Equation 3.5.

$$S_t = \frac{X_m L_{av} A_m}{M} \quad (3.5)$$

Single point BET can also be used by setting the intercept to 0 and ignoring the value of  $C$ . The data point at the relative pressure of 0.3 will match up the best with a multipoint BET. Single point BET can be used over the more accurate multipoint BET to determine the appropriate relative pressure range for multi-point BET.

The isotherm data obtained from partial pressure range of 0.05 to 0.3 is plugged into the BET equation, Equation 3.3 to obtain the BET plot. Using Equation 3.4, the monolayer capacity is determined. Now that  $X_m$  is known, then Equation 3.5 can be used to determine that the surface area. [104-106]

### 3.3 Structure Analysis Method-XRD

X-ray diffraction (XRD) is a rapid analytical technique primarily used for phase identification of a crystalline material and can provide information on unit cell dimensions. The analysed material is finely ground, homogenized, and average bulk composition is determined. Max von Laue, in 1912, discovered that crystalline substances act as three-dimensional diffraction gratings for X-ray wavelengths similar to the spacing of planes in a crystal lattice. X-ray diffraction is now a common technique for the study of crystal structures and atomic spacing. X-ray diffraction is based on constructive interference of monochromatic X-rays and a crystalline sample. These X-rays are generated by a cathode ray tube, filtered to produce monochromatic radiation, collimated to concentrate, and directed toward the

sample. The interaction of the incident rays with the sample produces constructive interference (and a diffracted ray) when conditions are described satisfy Bragg's Law, Equation 3.6. This law relates the wavelength of electromagnetic radiation to the diffraction angle and the lattice spacing in a crystalline sample.

$$2d \sin (\theta) = n\lambda \quad (3.6)$$

Where  $n$  is an integer called the order of reflectance,  $\lambda$  is wavelength of the radiation,  $d$  is the distance between two atomic planes ( $d$ -spacing), and  $\theta$  is the angle between the planes and the incident X-ray beam. This equation expresses the condition for diffraction, in effect, that for a given  $d$ -spacing and wavelength of radiation diffraction will occur at a unique angle between the beam and the set of planes in question. For crystals where the spacing is on the order of a few angstroms only a few constructive interference peaks are observed. These diffracted X-rays are then detected, processed and counted. By scanning the sample through a range of  $2\theta$  angles, all possible diffraction directions of the lattice should be attained due to the random orientation of the powdered material (Figure 3.3). [107-110]

Conversion of the diffraction peaks to  $d$ -spacing allows identification of the mineral because each mineral has a set of unique  $d$ -spacing. Typically, this is achieved by comparison of  $d$ -spacing with standard reference patterns.

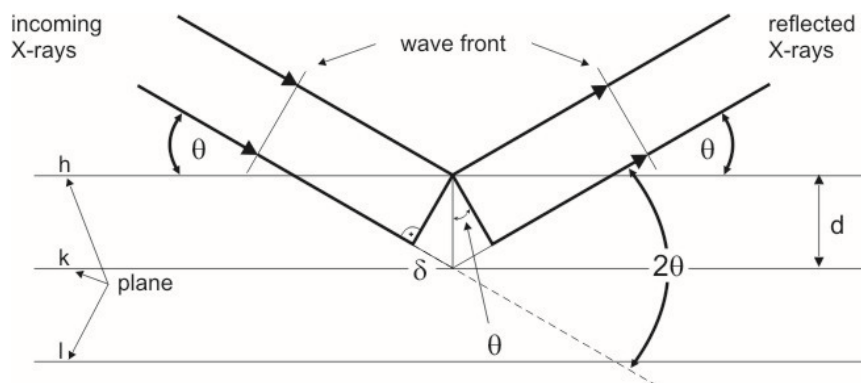


**Figure 3.3** Schematic representation of XRD by regularly spaced planes of atoms in a crystal.

Theta ( $\theta$ ) is the angle that the beam makes with the atomic planes;  $2\theta$  is the angle that the diffracted beam deviates from the primary beam;  $d$  is the distance between equivalent atomic planes in the crystal ( $d$ -spacing); and  $\lambda$  is wavelength of the radiation. [107]

In the cubic system, the plane spacing is related to the lattice constant  $a$  and the Miller indices by the following equation:

$$d = \frac{a}{\sqrt{h^2+k^2+l^2}} \quad (3.7)$$

Combining Eqn. 3.6 and 3.7,

$$\left(\frac{\lambda}{2\alpha}\right)^2 = \frac{\sin^2 \theta}{h^2+k^2+l^2} \quad (3.8)$$

Thus for all sets of Miller indices there is an angle that will satisfy the Bragg condition such that the value of  $\lambda/2\alpha$  is a constant. The distinction between the simple cubic (SC), body-centred cubic (BCC) and face-centred cubic (FCC) crystal structures can therefore be made by comparing the allowed Miller indices with those evaluated from the x-ray spectrum.

The powder method of X-Ray diffraction was devised independently in 1916 by Debye and Scherrer in Germany. The powder method is very useful and when properly employed, can yield a great deal of structural information about the material under investigation. The method is generally used in metallurgical work, as single crystals are not always available to the metallurgic. If the materials are polycrystalline wire, sheet, rod, etc. The Single formula given by Debye Scherrer can be used to calculate the crystalline size from the available XRD data. According to Scherrer, it is possible to determine the average grain size of spherical crystallites by measuring the FWHM of the diffraction peaks corrected for the contributions from the diffractometer. Debye Scherrer formula for calculate particle (crystalline) size, Eqn. 3.9.

$$B = \frac{k \lambda}{t \cos \theta} \quad (3.9)$$

Where;  $t$  (D) is the crystallite size,  $\lambda$  is the wavelength of the X-ray radiation (CuK $_{\alpha}$  = 0.15406 nm),  $k$  is a constant dependent on crystal shape 0.94 for spherical crystals with cubic symmetry,  $\theta$  is the diffraction angle and  $B$  is the line full width at half maximum (FWHM) (radians) height. This derivation is based on the assumption of a Gaussian shape profile. [111-113]

## CHAPTER IV

### EXPERIMENTAL PROCEDURE

#### 4.1 Initial Materials

The initial materials are uranyl nitrate hexahydrate (UNH) and commercial thorium nitrate. UNH was prepared by the conversion of  $U_3O_8$ , which was supplied by Canada Atomic Energy, to the ammonium diuranate (ADU) form at Cekmece Research and Training Center and commercial thorium nitrate salt supplied by company of Rhone-Poulench.

Experimental studies were performed in the Reactor Materials Unit of the Cekmece Nuclear Research and Training Center (CNAEM).

Before starting the experiments chemicals needed, uranyl nitrate and thorium nitrate powders, HMTA and Urea powders, silicon oil, ammonia ( $NH_3$ ) and carbon tetrachloride( $CCl_4$ ) solutions, argon(Ar),  $Ar+H_2(5\%)$ ,  $CO_2$  and nitrogen gasses were provided.

The  $UO_2$ ,  $ThO_2$ ,  $ThO_2-5\%UO_2$  and  $ThO_2-10\%UO_2$  green pellets were prepared by internal gelation technique of sol-gel process where in which we used the solutions of uranium nitrate, thorium nitrate and their desired mixtures for the mixed oxide pellets.

The flow-sheet used for the preparation of  $UO_2$ ,  $ThO_2$  and  $(Th,U)O_2$  pellets by internal gelation in the present study is shown in Figure 4.1.

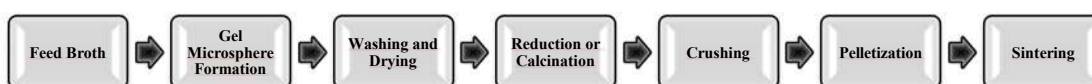


**Figure 4.1** Flow sheet for the preparation of  $UO_2$ ,  $ThO_2$  and  $(Th,U)O_2$  pellets by internal gelation technique



## 4.2 Preparation of Gel Microspheres

The gelation behaviour of the feed solution is understood the way urea and HMTA react with metal nitrate solutions under varying temperature conditions. The feed solution is made by mixing heavy metal nitrate solution with an equimolar solution of HMTA and urea under cooled conditions. Urea ( $\text{CO}(\text{NH}_2)_2$ ) reacts with the heavy metal ions U(VI), Pu(IV) and Th(IV) at low temperature to form complexes which prevent hydrolysis at low temperature of these metal ions by HMTA ( $((\text{CH}_2)_6\text{N}_4)$ ). The formation of complex prevents the hydrolysis of the metal ion at low temperature. The metal ion complexes dissociate during gelation as they are unstable at higher temperatures.

### 4.2.1 Preparation of $\text{UO}_2$ Microspheres

Preparation of 3 M UNH solution which was pre-neutralized to  $\text{NO}_3/\text{U} \approx 1.7$  by adding ammonia solution with concentration of %25. The calculated weights of analytical grade HMTA and urea crystals were dissolved in distilled water to obtain 3 M HMTA-Urea solution. The uranium concentration of in broth solution was 1.2 M.



**Figure 4.2** Pure Uranyl Nitrate Crystal, HMTA+Urea and Uranyl Nitrate solutions.

### Dropping and gelation

UNH and HMTA/Urea solutions were cooled to  $0.5 \pm 0.1^\circ\text{C}$  by chiller and then HMTA/Urea solution dropped slowly in UNH solution during stirring with glass rod. The temperature of silicon oil column was heated to  $90 \pm 2^\circ\text{C}$ .

Then this broth solution was dropped through 0.5 mm diameter nozzle into hot silicon oil in glass column to make gel microsphere. The microspheres are collected from the bottom side of column in a beaker.

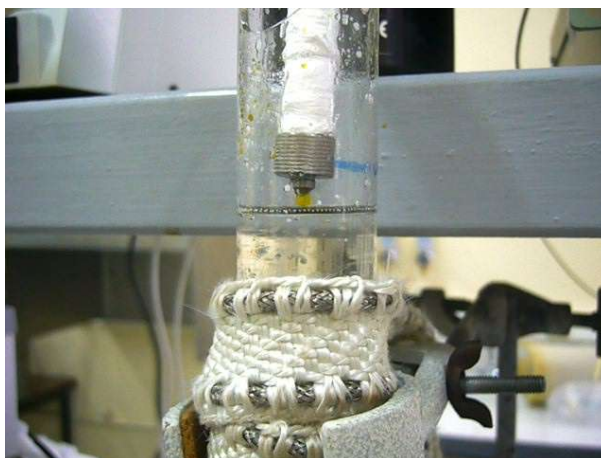


**Figure 4.3** Forming microspheres

### **Washing and drying**

These collected microspheres first washed five times with carbon tetra chloride ( $\text{CCl}_4$ ) to remove silicon oil contamination, and then the microspheres washed eight times with %2 ammonia solution to complete gelation and removing other contaminations. After washing steps, the microspheres were dried in heat controlled oven 8 hours at  $100^\circ\text{C}$  in air with slow heating rate.



**Figure 4.4** Washing and dried  $\text{UO}_3$  microspheres

### **Reduction**

The dried  $\text{UO}_3$  microspheres were reduced to  $\text{UO}_{2+x}$  at  $650^\circ\text{C}$  in  $\text{Ar}+\text{H}_2(\%5)$  gas mixture for 1.5 hours. During cooling period of reduction step at about  $180^\circ\text{C}$  reducing gas stopped and from this temperature to room temperature the furnace is cooled in  $\text{CO}_2$  atmosphere to passivation of the microspheres.

#### 4.2.2 Preparation of ThO<sub>2</sub> Microspheres

Preparation of 3 M thorium nitrate (Th(NO<sub>3</sub>)<sub>4</sub>).5H<sub>2</sub>O solution which was pre-neutralized to NO<sub>3</sub>/Th ≈3 by adding ammonia solution with concentration of %25. The calculated weights of analytical grade HMTA and urea crystals were dissolved in distilled water to obtain 3 M HMTA-Urea solution. The thorium concentration of in broth solution was 1.2 M.

#### Dropping and gelation

Thorium Nitrate and HMTA/Urea solutions were cooled to 10±1°C by chiller and then HMTA/Urea solution dropped slowly in Thorium Nitrate solution during stirring with glass rod. The temperature of silicon oil column was heated to 105±2°C. Then this broth solution was dropped through 0.5 mm diameter nozzle into hot silicon oil in glass column to make gel microsphere. The microspheres are collected from the bottom side of column in a beaker.

#### Washing, drying and calcination:

These collected microspheres first washed five times with carbon tetra chloride (CCl<sub>4</sub>) to remove silicon oil contamination, and then the microspheres washed twelve times with %5 ammonia solution to complete gelation and removing other contaminations.

After washing steps, the microspheres were dried in heat controlled oven at 50°C and then the oven heated to 100°C in air with slow heating rate, the microsphere were during two days at this temperature.



**Figure 4.5** Dried and calcined ThO<sub>2</sub> microspheres.

The dried ThO<sub>2</sub> microspheres were calcined around 700°C for five hours to remove residual chemicals.

#### **4.2.3 Preparation of (Th,U)O<sub>2</sub> Microspheres**

Preparation of 3 M uranyl nitrate hexahydrate (UNH) and thorium nitrate (Th(NO<sub>3</sub>)<sub>4</sub>) (Th<sub>0.9</sub>U<sub>0.1</sub>)O<sub>2</sub> and (Th<sub>0.95</sub>U<sub>0.05</sub>)O<sub>2</sub> solutions which are pre-neutralized by adding ammonia solution with concentration of %25. The calculated weights of analytical grade HMTA and urea crystals were dissolved in distilled water to obtain 3 M HMTA-Urea solution. The thorium and uranium concentrations of in broth solution were 1.2 M.

#### **Dropping and gelation**

UNH and thorium nitrate were mixed in the specified proportions before adding gelling agents. The mixed metal solution and HMTA/Urea solution were cooled to about 13°C during stirring with glass rod and then adding slowly one another to produce feed solution. The temperature of silicon oil column was heated to 120±2°C. After that, this feed solution was dropped through 0.5 mm diameter nozzle into hot silicon oil in glass column to make gel microsphere. The microspheres are collected from the bottom side of column in a beaker.

#### **Washing and drying**

These collected microspheres first washed five times with carbon tetra chloride (CCl<sub>4</sub>) to remove silicon oil contamination, and then the microspheres washed ten times with 5% ammonia solution to complete gelation and removing other contaminations. After washing steps, the microspheres were dried in heat controlled oven at 50°C and then the oven heated to 100°C in air with slow heating rate, the kernels were during two days at this temperature.

#### **Calcination and reduction**

The dried ThO<sub>2</sub>-10%UO<sub>2+x</sub> and ThO<sub>2</sub>-5%UO<sub>2+x</sub> microspheres were calcined around 700°C for five hours to remove residual chemicals.

The calcined microspheres were reduced in Ar+5% H<sub>2</sub> gas mixture at 650°C for 1.5 hours. During cooling period of reduction step at about 180°C reducing gas stopped

and from this temperature to room temperature the furnace is cooled in CO<sub>2</sub> atmosphere to passivation of the microspheres.

### 4.3 Preparation of Green Pellets

The reduced UO<sub>2</sub>, ThO<sub>2</sub>, ThO<sub>2</sub>-10%UO<sub>2</sub> and ThO<sub>2</sub>-5%UO<sub>2</sub> microspheres were extremely hard to pressed directly and so the kernels were grinded with automatic mortar grinder to obtain soft powder. These ThO<sub>2</sub>, ThO<sub>2</sub>, ThO<sub>2</sub>-10%UO<sub>2</sub> and ThO<sub>2</sub>-5%UO<sub>2</sub> powders were pressed in a 6 mm diameter and around 4 mm in height by compaction at nearly 567 MPa for UO<sub>2</sub> powder, 392 MPa for ThO<sub>2</sub> powder and 390 MPa for mix ThO<sub>2</sub>-10%UO<sub>2</sub> and ThO<sub>2</sub>-5%UO<sub>2</sub> powders. The green densities of the pellets have been calculated by geometrical method.

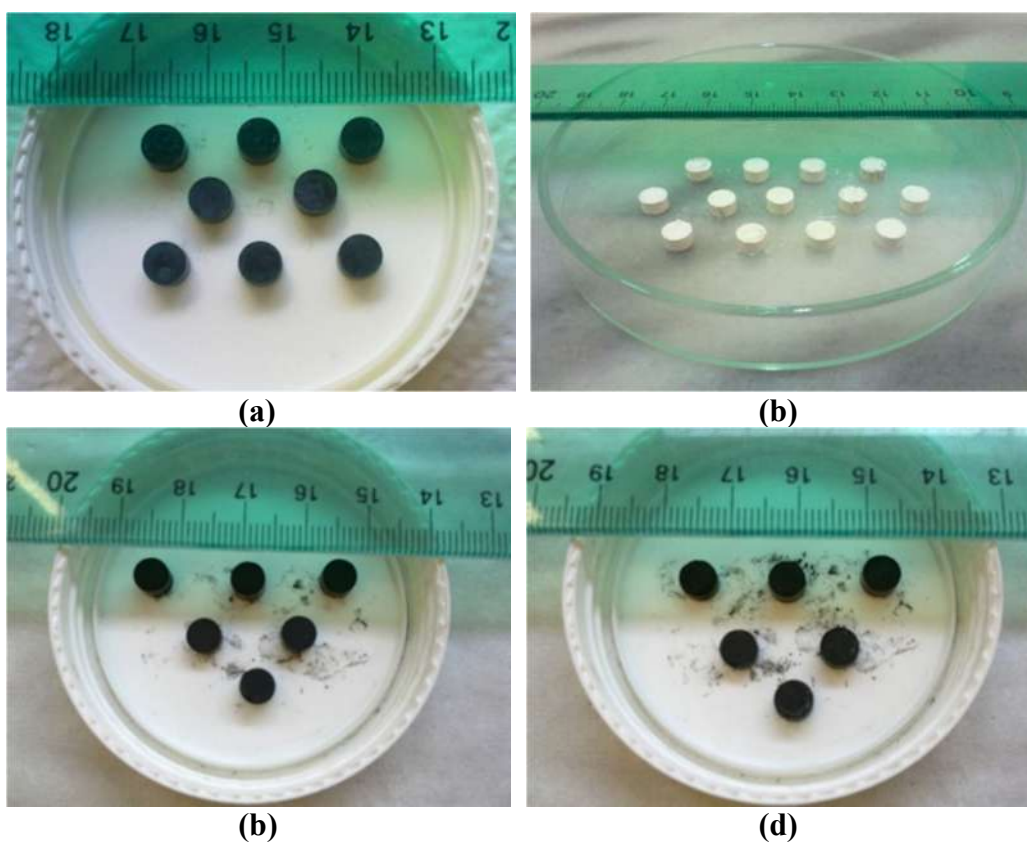


**Figure 4.6** (a) UO<sub>2</sub>, (b) ThO<sub>2</sub>, (c) ThO<sub>2</sub>-10%UO<sub>2</sub>, and (d) ThO<sub>2</sub>-5%UO<sub>2</sub> pellets

### 4.4 Characterization

In order to evaluate the influence of the preparation method on several chemical compositions of the powders as well as the sintered pellets, the microstructural characterization of the powdered compounds was undertaken in terms of thermogravimetry (TGA/DTA), specific surface area (BET) and crystallization state

(XRD). In this study powders of the  $\text{UO}_2$ ,  $\text{ThO}_2$ ,  $\text{ThO}_2$ -10% $\text{UO}_2$  and  $\text{ThO}_2$ -5% $\text{UO}_2$  were characterized by the following techniques:

#### **4.4.1 Thermogravimetry**

The TGA/DTA curves for  $\text{UO}_2$ ,  $\text{ThO}_2$ ,  $\text{ThO}_2$ -10% $\text{UO}_2$  and  $\text{ThO}_2$ -5% $\text{UO}_2$  microspheres oxidation were carried out by TGA/DTA-Netzsch STA 449 C simultaneous thermal analyzer up to 800°C at 10°C/min in an air atmosphere and cooled down to room temperature when the desired temperature was reached. The kernels were placed in platinum covered crucibles, an empty being the reference.

#### **4.4.2 BET**

Before sintering procedures, the specific surface area of the  $\text{UO}_2$ ,  $\text{ThO}_2$ ,  $\text{ThO}_2$ -10% $\text{UO}_2$  and  $\text{ThO}_2$ -5% $\text{UO}_2$  powders were measured using the BET method with nitrogen as the adsorbate gas.  $\text{N}_2$  adsorption and desorption isotherms were measured by Quantachrome Autosorb System at different temperature. All samples were firstly degassed in a vacuum at high temperatures.

The adsorption and desorption BET isotherms of the  $\text{UO}_2$ ,  $\text{ThO}_2$ -10% $\text{UO}_2$  and  $\text{ThO}_2$ -5% $\text{UO}_2$  powders prepared by heating 150 °C and  $\text{ThO}_2$  powder prepared by heating 300 °C.

#### **4.4.3 XRD**

The phase analysis was performed using X-ray diffractometry (Bruker AXS D8 Advance diffractometer). The crystallite sizes were evaluated by step scanning diffraction X-ray profile employing a Siemens ceramic X-ray equipped with a  $\text{CuK}\alpha$  tube for diffractometry, operated at 40 kV and 40 mA. The crystallite size was determined from the line broadening of XRD peaks; the full scan  $2\theta$  range was from 20° to 80° and carried at low speed of 0.01°/min. The Philips software allows the crystallite size determination through the comparison of profile lines broadening related to a standard material. For this purpose, Scherrer's relationship was utilized [114].

FWHM of the each diffraction peaks of the  $\text{UO}_2$ ,  $\text{ThO}_2$ ,  $\text{ThO}_2$ -10% $\text{UO}_2$  and  $\text{ThO}_2$ -5% $\text{UO}_2$  powders corrected for the contributions from the diffractometer were measured and then according to Scherrer, it is possible to determine the average grain size of spherical crystallites by measuring the FWHM of the diffraction peaks

corrected for the contributions from the diffractometer. Particle (crystalline) size of the powder was calculated from the Debye Scherrer formula. The wavelength of the X-ray radiation,  $\lambda$  ( $\text{CuK}\alpha$ ) is 0.15406 nm.

#### **4.5 Sintering of the Green Pellets**

The sintering behaviour of the  $\text{UO}_2$ ,  $\text{ThO}_2$ ,  $\text{ThO}_2$ -10% $\text{UO}_2$  and  $\text{ThO}_2$ -5% $\text{UO}_2$  pellets prepared by sol-gel method was studied by measuring the shrinkage in axial direction using a push rod type dilatometer (Netzsch DIL 402 C). For the dilatometric studies, the samples used were in the form of pellets of 6 mm diameter and around 4 mm length.

The length change measurements were made by Linear Voltage Differential Transformer (LVDT), which was maintained at a constant temperature by means of water circulation from a constant temperature bath. The accuracy of the measurement of change in length was within  $\pm 0.1 \mu\text{m}$ . The temperature was measured using a calibrated Pt/PtRh10% thermocouple which was placed closely above the sample. A small force of 0.25 N was applied to the sample through the push rod. The dilatometric experiments were carried out in reducing Ar+5%  $\text{H}_2$  atmosphere with a heating rate of  $5^\circ\text{C}/\text{min}$  in isothermal condition. The shrinkage of the standard sample was measured under identical condition in order to correct for the differences in shrinkage between in the sample holder and the sample. The selection of the temperature programme was made by computer via the data acquisition system. The dilatometric data were obtained are in the form of curves of dimension against time and temperature.

Time vs. dimensional shrinkage plots were obtained from dilatometric studies for all the pellets. The data obtained were thus analyzed to find out the kinetics of sintering and the activation energies of the  $\text{UO}_2$ ,  $\text{ThO}_2$ ,  $\text{ThO}_2$ -10% $\text{UO}_2$  and  $\text{ThO}_2$ -5% $\text{UO}_2$  pellets.

## CHAPTER V

### RESULTS and DISCUSSIONS

#### 5.1 Investigation of TGA/DTA curve by Thermogravimetry

Oxygen to metal ratio (O/M) of the powders were calculated by thermogravimetric analysis which technique was described in chapter III. The O/U ratio of the  $\text{UO}_2$ ,  $\text{ThO}_2$ ,  $\text{ThO}_2$ -10% $\text{UO}_2$  and  $\text{ThO}_2$ -5% $\text{UO}_2$  powders are listed in Table 5.6.

##### 5.1.1 TGA/DTA curve of the $\text{UO}_{2+x}$

Figure 5.1 presents TGA/DTA curve of the  $\text{UO}_{2+x}$  powder that was heated at a rate of  $10^\circ\text{C}/\text{min}$  in an air atmosphere and cooled down to room temperature when the desired temperature was reached.

In this figure, the increasing curve (TG) designates the increase in the weight of the sample due to oxygen uptake while the blue ones is the differential increase in weight. The decrease in weight seen shortly after the heating is started must be due to the removal of moisture from powder. In Figure 5.1, the first step of air oxidation of  $\text{UO}_{2+x}$  at  $\sim 150^\circ\text{C}$  shows  $\text{U}_3\text{O}_7$  formation. In the second step reaction, there is a sharp increase in oxygen content at about  $410^\circ\text{C}$  showing the more stable  $\text{U}_3\text{O}_8$  formation. Considering the these oxidation steps, O/U ratio was determined by thermo gravimetric method as 2.207.

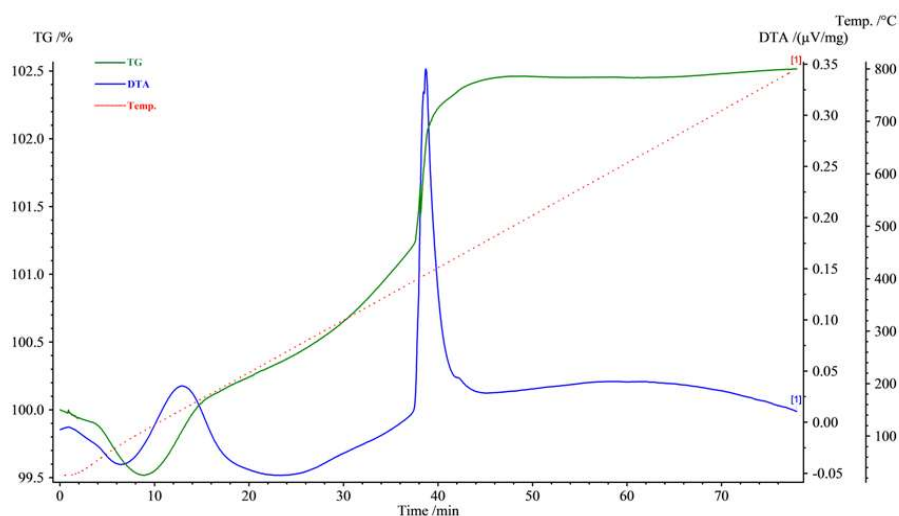
##### 5.1.2 TGA/DTA curve of the $\text{ThO}_2$

Figure 5.2 presents TGA/DTA curve of the  $\text{ThO}_2$  powder that was heated to  $800^\circ\text{C}$  at a rate of  $10^\circ\text{C}/\text{min}$  in an air atmosphere and cooled down to room temperature when the desired temperature was reached.

In this figure, the decrease in weight seen shortly after the heating is started and then keep on decreasing, which must be due to the removal of moisture from powder.



ThO<sub>2</sub> is relatively inert and does not oxidize unlike UO<sub>2</sub>, which oxidizes easily to U<sub>3</sub>O<sub>8</sub>. Therefore, there is no increase in weight as shown in Figure 5.2.



**Figure 5.1** TGA/DTA curves of UO<sub>2+x</sub>

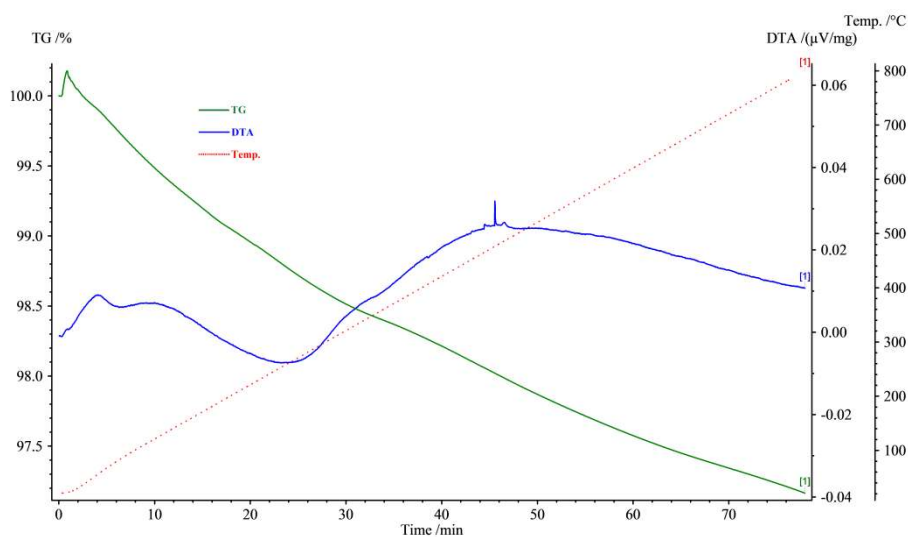


**Figure 5.2** TGA/DTA curves of ThO<sub>2</sub>

### 5.1.3 TGA/DTA curve of the (Th,U)O<sub>2+x</sub>

Figures 5.3 and 5.4 represent TGA/DTA curve of the ThO<sub>2</sub>-10%UO<sub>2+x</sub> and ThO<sub>2</sub>-5%UO<sub>2+x</sub> powders, respectively. These were heated to 800°C at a rate of 10°C/min in an air atmosphere and cooled down to room temperature when the desired temperature was reached.

In these figures, the increasing curve designates the increase in the weight of the sample due to oxygen uptake of uranium.  $\text{ThO}_2$  is relatively inert and does not oxidize unlike  $\text{UO}_2$ , which oxidizes easily to  $\text{U}_3\text{O}_8$ . In Figure 5.3 and Figure 5.4, the formations  $\text{U}_3\text{O}_8$  by oxidation of  $\text{UO}_{2+x}$  are about at  $415^\circ\text{C}$  for  $\text{ThO}_2$ -10% $\text{UO}_2$  and at  $400^\circ\text{C}$  for  $\text{ThO}_2$ -5% $\text{UO}_2$  powders. Considering these oxidation steps, O/U ratio were determined by thermo gravimetric method as 2.167 and 2.254, respectively.

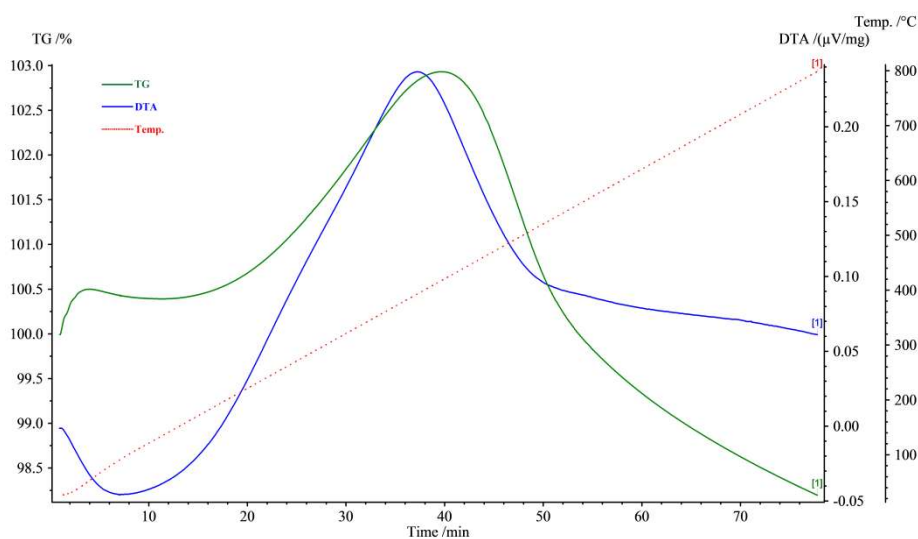


**Figure 5.3** TGA/DTA curves of  $\text{ThO}_2$ -10% $\text{UO}_{2+x}$

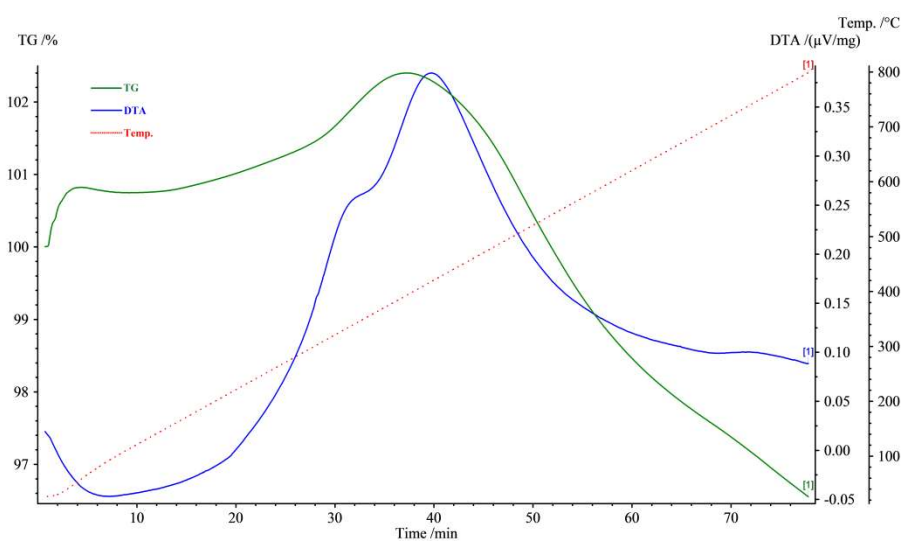


**Figure 5.4** TGA/DTA curves of  $\text{ThO}_2$ -5% $\text{UO}_{2+x}$

## 5.2 Investigation of Specific Surface Area by BET Method

The BET plots of the UO<sub>2</sub>, ThO<sub>2</sub>, ThO<sub>2</sub>-10%UO<sub>2</sub> and ThO<sub>2</sub>-5%UO<sub>2</sub> powders using points collected at the pressure range 0.05 to 0.3 are shown in Figure 5.5. C values for all powders high from 5, it means strong interaction N<sub>2</sub> with powders surface.

Specific surface area for UO<sub>2</sub> and ThO<sub>2</sub> data are in agreement with these in the literature powders present low surface area values [115]. The increase in the Th metal ion concentration from the ThO<sub>2</sub>-10%UO<sub>2</sub> and ThO<sub>2</sub>-5%UO<sub>2</sub> powders, specific surface area of these powders increased from 2.5 m<sup>2</sup>/g to 3.07 m<sup>2</sup>/g. [115,116]

In Table 5.1 C, X<sub>m</sub>, the total and specific surface area is listed for the UO<sub>2</sub>, ThO<sub>2</sub>, ThO<sub>2</sub>-10%UO<sub>2</sub> and ThO<sub>2</sub>-5%UO<sub>2</sub> powders.

**Table 5.1** Parameters used for the calculation of specific surface area of the powders

	<b>Powder composition</b>			
	<b>UO<sub>2</sub></b>	<b>ThO<sub>2</sub>-10%UO<sub>2</sub></b>	<b>ThO<sub>2</sub>-5%UO<sub>2</sub></b>	<b>ThO<sub>2</sub></b>
<b>Sample Weight (g)</b>	2.3059	1.501	1.5715	1.7501
<b>Slope</b>	241.5	745	861	484
<b>Intercept</b>	2.14	9.75	25.2	5.15
<b>C</b>	114.10	74.9	35.2	88.24
<b>X<sub>m</sub></b>	4.105x10 <sup>-3</sup>	1.324 x10 <sup>-3</sup>	1.128 x10 <sup>-3</sup>	2.044 x10 <sup>-3</sup>
<b>Total Surface Area (m<sup>2</sup>/g)</b>	14.30	4.614	3.931	7.120
<b>Specific Surface Area (m<sup>2</sup>/g)</b>	<b>6.2017</b>	<b>2.5016</b>	<b>3.0741</b>	<b>4.0683</b>

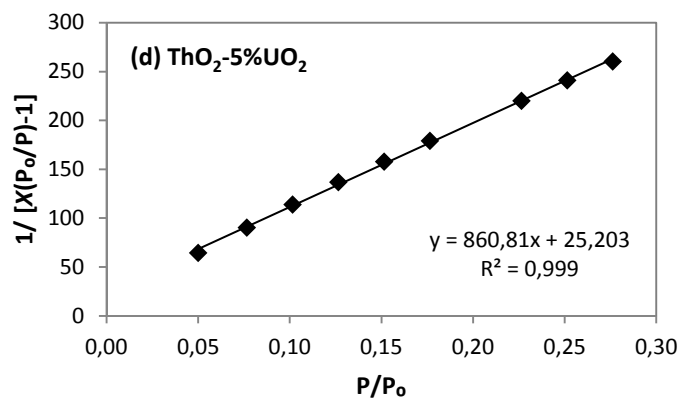
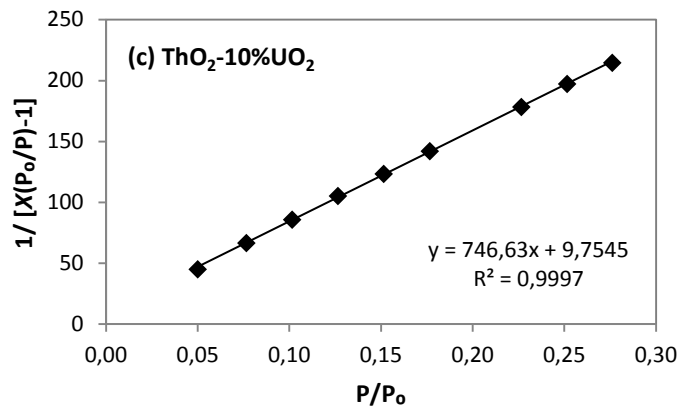
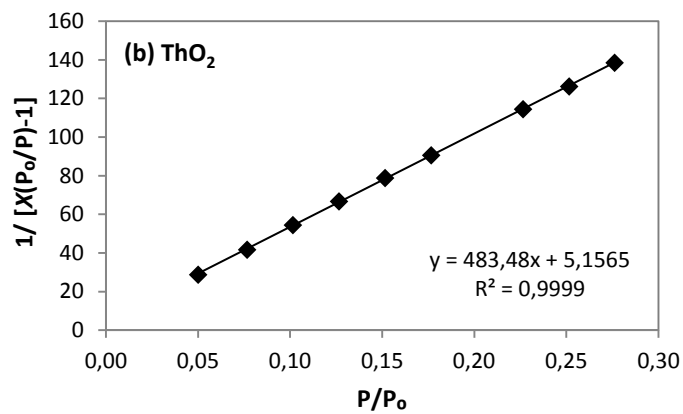
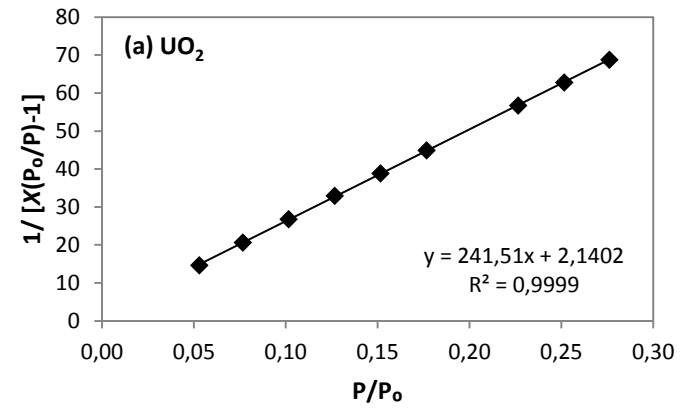


**Figure 5.5.** BET plot of **(a)**UO<sub>2</sub>, **(b)**ThO<sub>2</sub>, **(c)**ThO<sub>2</sub>-10%UO<sub>2</sub> and **(d)** ThO<sub>2</sub>-5%UO<sub>2</sub> powders.

## 5.3 Investigation of Crystallite Size from XRD

### 5.3.1 Crystallite sizes of UO<sub>2</sub> powder

The XRD pattern of the UO<sub>2+x</sub> powder obtained from our experiment and similar uraninite-UO<sub>2</sub> particle calculated from ICSD using POWD-12++[117,118] are compared in Figure 5.6. The pattern of the UO<sub>2+x</sub> compound particles from our experiment and Uraninite-UO<sub>2</sub> compound particles correspond perfectly and appeared to be much like a  $2\theta$  angle. Crystal lattice and unit cell data source are face centered cubic and single crystal.

The X-ray diffraction spectrum of the UO<sub>2</sub> powder was given in Figure 5.6. In this XRD pattern of the peaks at  $2\theta = 28.324, 32.815, 47.11$  and  $55.869^\circ$ , corresponding to the lattice planes (111), (200), (220) and (311), respectively, of the face centered cubic (fcc) structure of UO<sub>2</sub>, were present. The sizes of crystallites corresponding to major diffracting plan are summarized in Table 5.2.

### 5.3.2 Crystallite sizes of ThO<sub>2</sub> powder

The XRD pattern of the ThO<sub>2</sub> powder obtained from our experiment and similar thorianite-ThO<sub>2</sub> particle calculated from ICSD using POWD-12++ [117,118] are compared in Figure 5.7. The pattern of the ThO<sub>2</sub> compound particles from our experiment and Thorianite-ThO<sub>2</sub> compound particles correspond perfectly and appeared to be much like a  $2\theta$  angle. Crystal lattice and unit cell data source are face centered cubic and single crystal.

The X-ray diffraction spectrum of the ThO<sub>2</sub> powder was given in Figure 5.7. In this XRD pattern of the peaks at  $2\theta = 27.612, 31.976, 45.817,$  and  $54.320^\circ$ , corresponding to the lattice planes (111), (200), (220) and (311), respectively, of the face centered cubic (fcc) structure of ThO<sub>2</sub>, were present. The sizes of crystallites corresponding to major diffracting plan are summarized in Table 5.3.

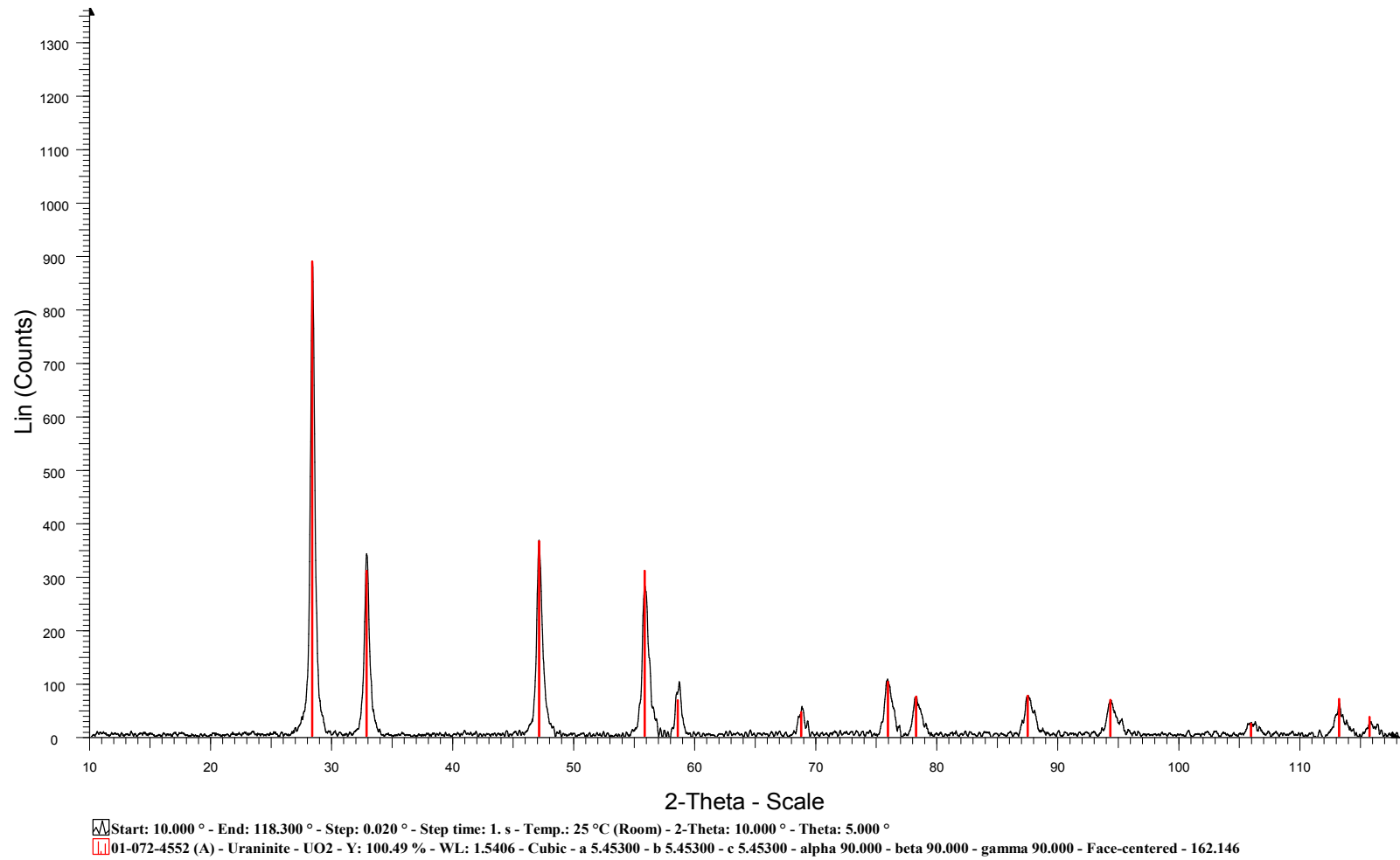
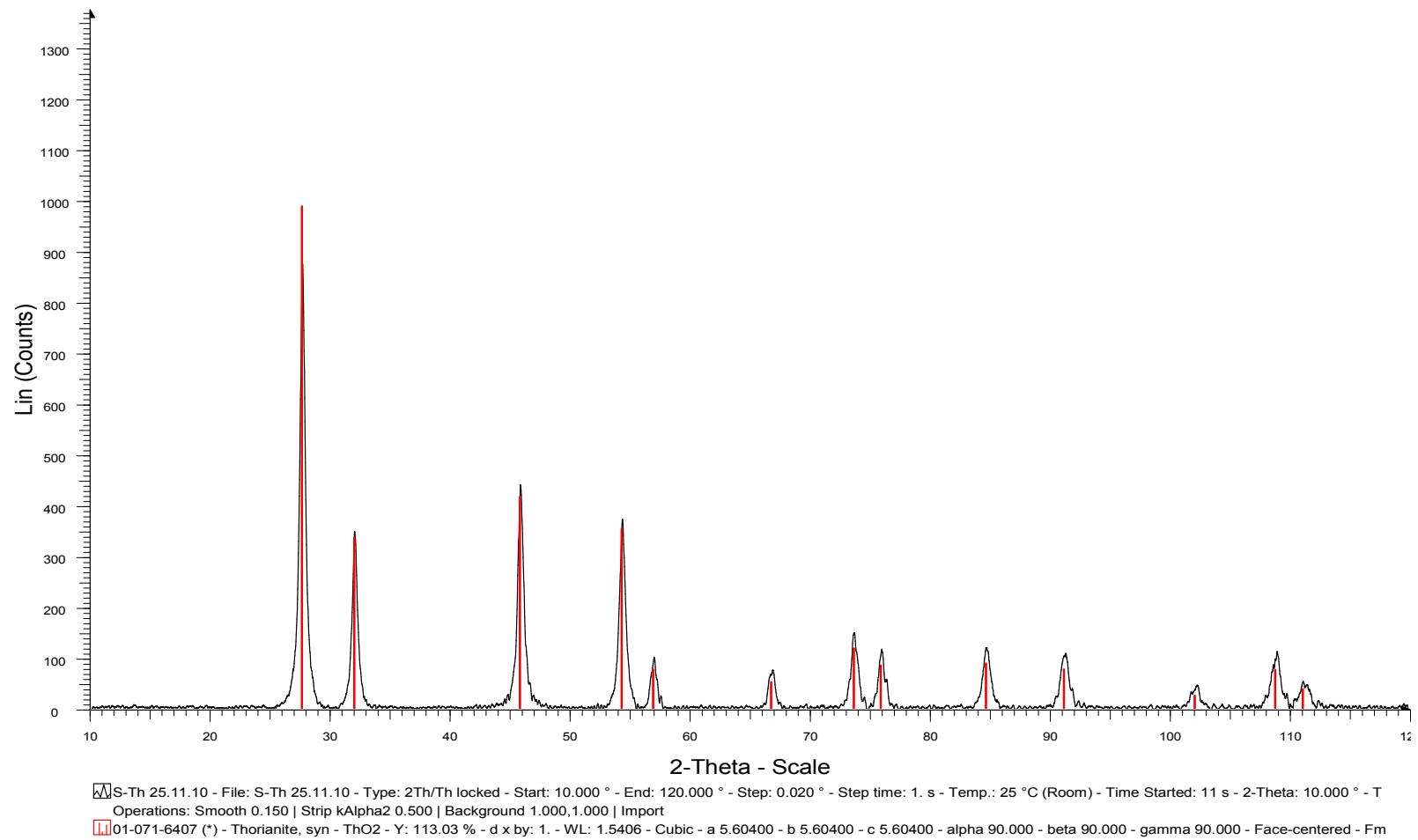


Figure 5.6 X-Ray Diffraction Pattern of UO<sub>2</sub> powder



**Figure 5.7** X-Ray Diffraction Pattern of ThO<sub>2</sub> powder

**Table 5.2** Crystallite sizes of UO<sub>2</sub> powder calculated from XRD

<b>2θ</b>	<b>FWHM</b>	<b>hkl</b>	<b>d (Å)</b>	<b>B</b>	<b>a* (Å)</b>	<b>t** (Å)</b>
28.324	0.4	(111)	3,148395	0,006981	5.4532	202,55661
32.815	0.428	(200)	2,727044	0,00747	5.4541	191,34395
47.11	0.508	(220)	1,927537	0,008866	5.4519	168,7029
55.869	0.619	(311)	1,644317	0,010804	5.4536	143,65255

\*a is lattice constant, \*\*t is crystallite size.

**Table 5.3** Crystallite sizes of ThO<sub>2</sub> powder calculated from XRD

<b>2θ</b>	<b>FWHM</b>	<b>hkl</b>	<b>d (Å)</b>	<b>B</b>	<b>a* (Å)</b>	<b>t** (Å)</b>
27.612	0.514	(111)	3,22794	0,008971	5.5909	157,38789
31.976	0.523	(200)	2,796657	0,009128	5.5933	156,25472
45.817	0.575	(220)	1,97888	0,010036	5.5971	148,32517
54.320	0.594	(311)	1,68749	0,010367	5.5967	148,6467

\*a is lattice constant, \*\*t is crystallite size.

### 5.3.3 Crystallite sizes of (Th,U)O<sub>2</sub> powders

The XRD patterns of the ThO<sub>2</sub>-10%UO<sub>2</sub> and ThO<sub>2</sub>-5%UO<sub>2</sub> are shown in Figure 5.8 and Figure 5.9, respectively. The ThO<sub>2</sub>-10%UO<sub>2</sub> and ThO<sub>2</sub>-5%UO<sub>2</sub> powders are compared with ThO<sub>2</sub> powder pattern in the same figure (Fig 5.10). The intensity was plotted as a function of diffraction angle, 2θ.

Both ThO<sub>2</sub>-10%UO<sub>2</sub> and ThO<sub>2</sub>-5%UO<sub>2</sub> powders show single phase of CaF<sub>2</sub> type solid solution similar to the pure UO<sub>2</sub> and ThO<sub>2</sub> powders, indicating that solid solutions were formed to extent. But it supposed that the solid solution is not yet fully formed since the FWHM of the peaks is wider than that of pure UO<sub>2</sub> and ThO<sub>2</sub>. These appreciable broadening regions in the X-ray diffraction regions of the ThO<sub>2</sub>-10%UO<sub>2</sub> and ThO<sub>2</sub>-5%UO<sub>2</sub> powder may in fact correspond to the actual size of the particles.

The X-ray diffraction spectrum of the ThO<sub>2</sub>-10%UO<sub>2</sub> and ThO<sub>2</sub>-5%UO<sub>2</sub> powders was given in Figure 5.8 and 5.9, respectively. In these XRD patterns corresponding to the lattice planes (111), (200), (220) and (311), respectively, of the face centred cubic (fcc) structure of ThO<sub>2</sub>-10%UO<sub>2</sub> and ThO<sub>2</sub>-5%UO<sub>2</sub>, were present. The sizes of crystallites corresponding to major diffracting plan are summarized in Table 5.4 for ThO<sub>2</sub>-10%UO<sub>2</sub> and in Table 5.5 for ThO<sub>2</sub>-5%UO<sub>2</sub>.



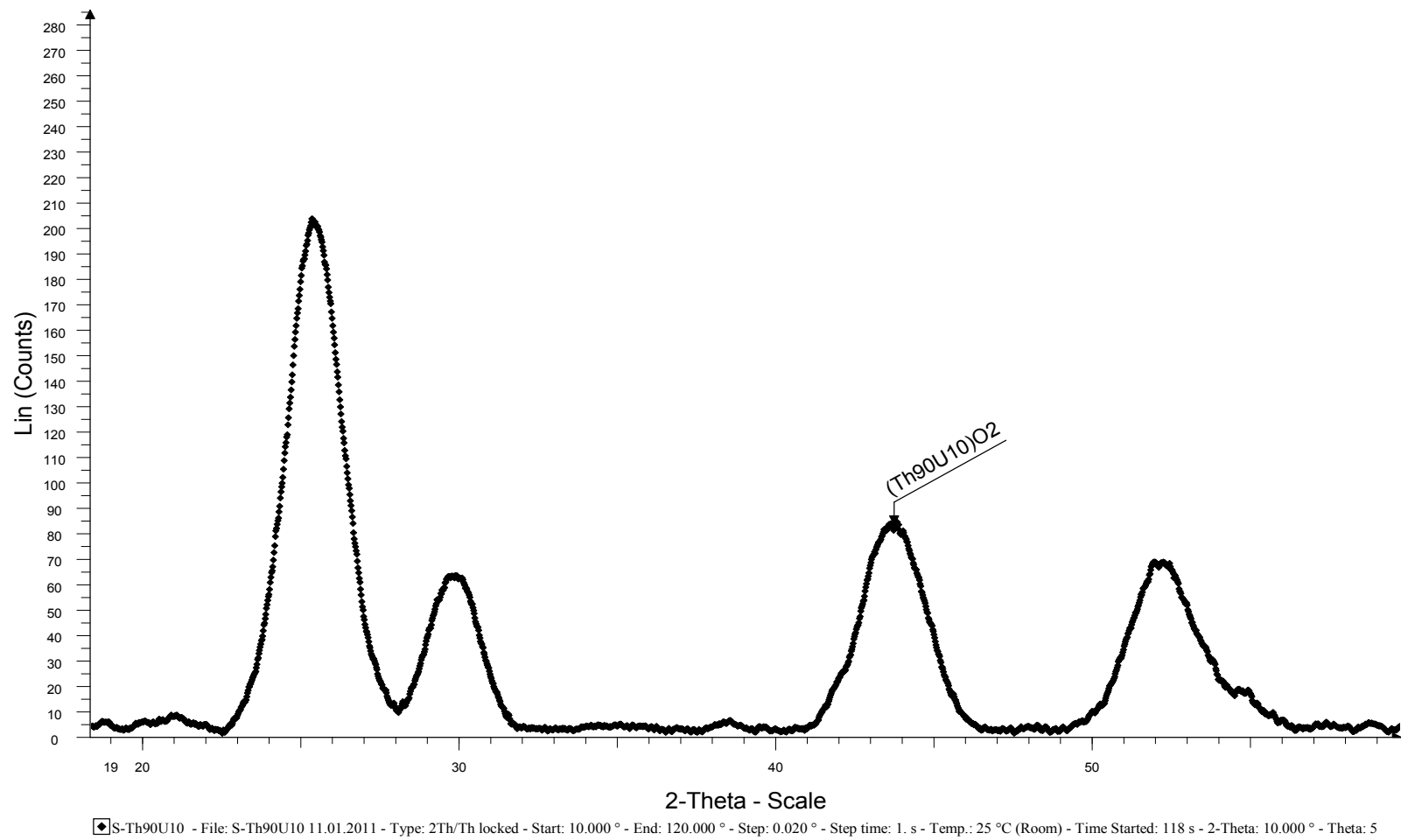


**Figure 5.8** X-Ray Diffraction Pattern of ThO<sub>2</sub>-10%UO<sub>2</sub> powder

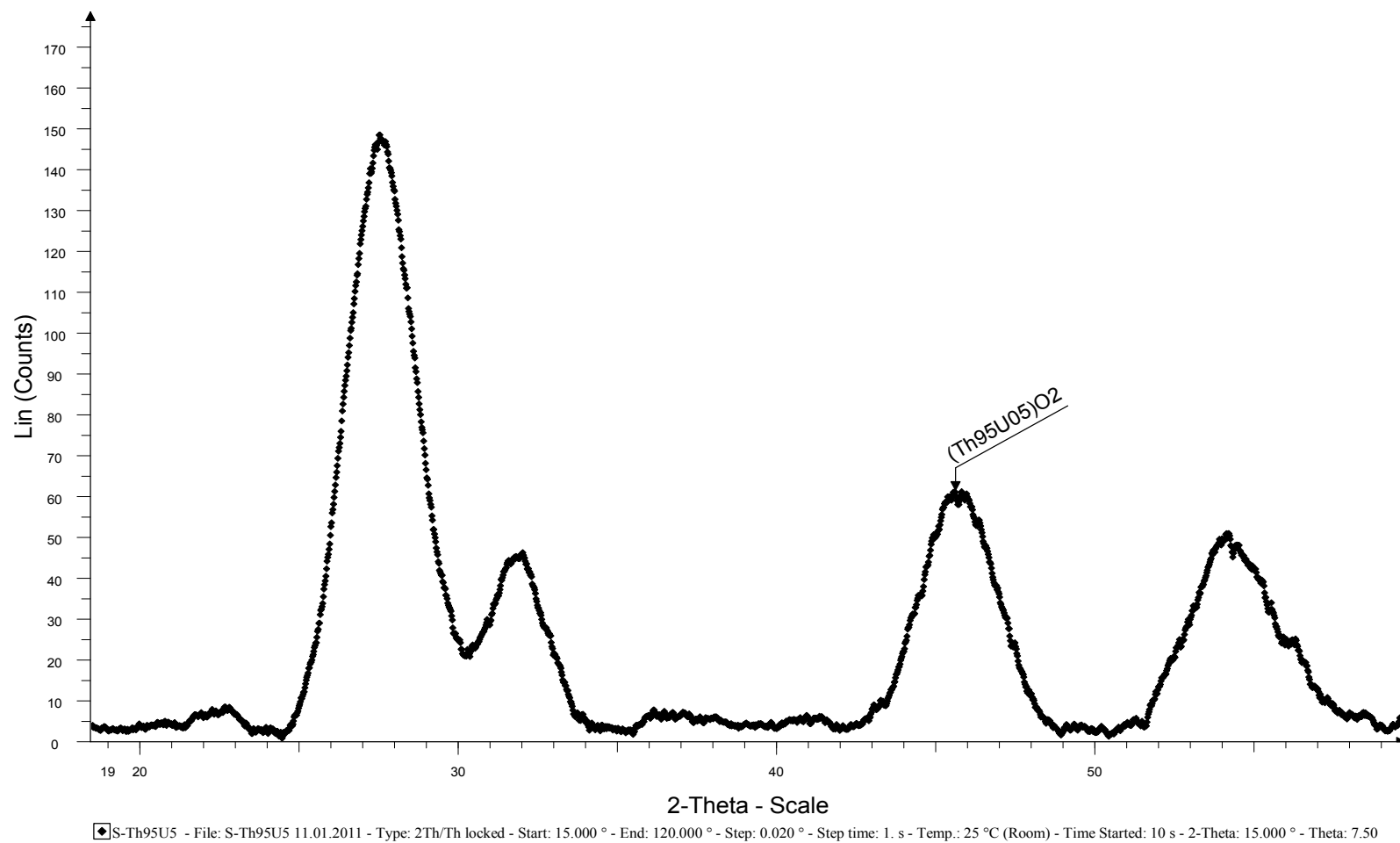


**Figure 5.9** X-Ray Diffraction Pattern of ThO<sub>2</sub>-5%UO<sub>2</sub> powder

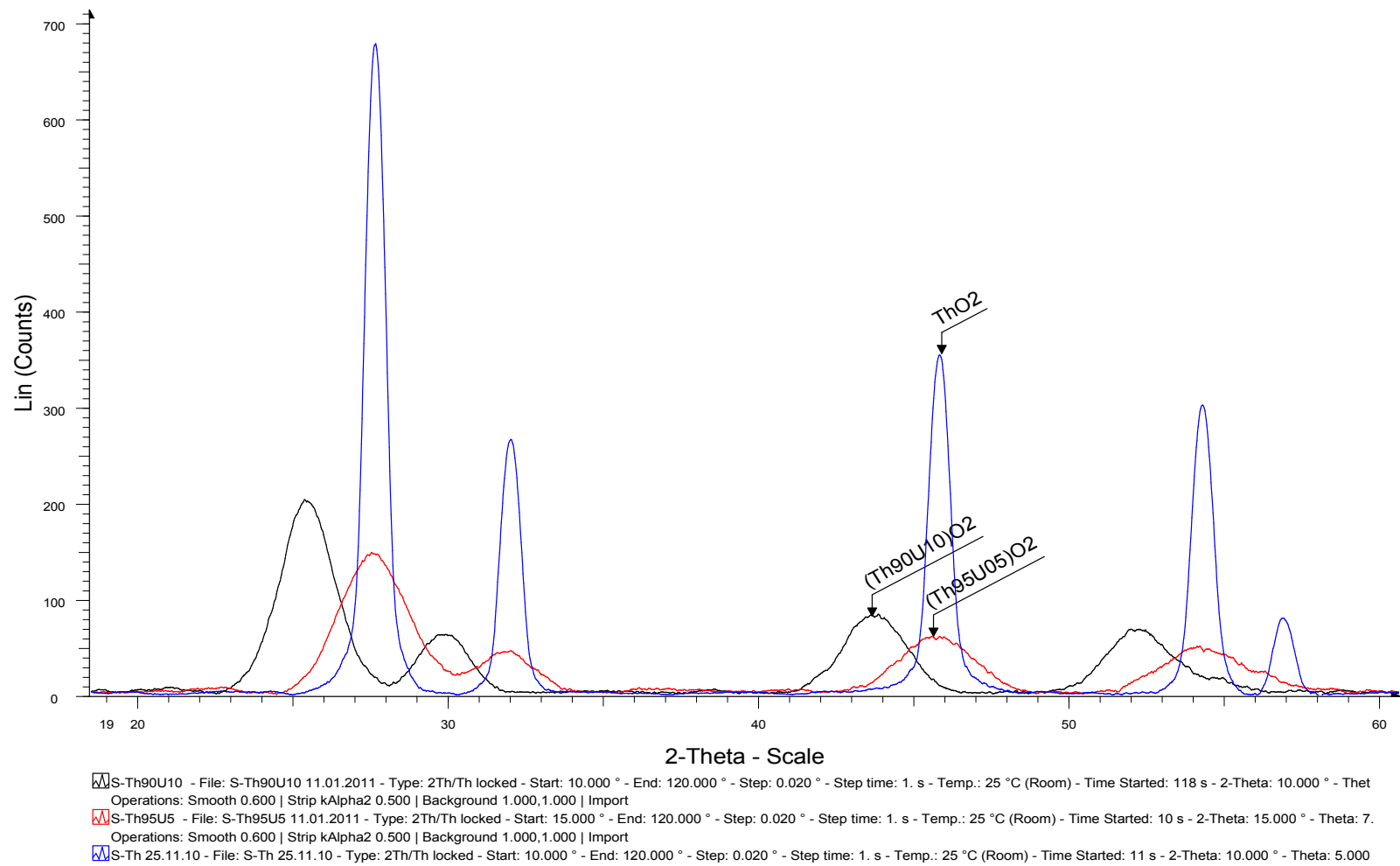


**Figure 5.10** XRD of ThO<sub>2</sub>, ThO<sub>2</sub>-10%UO<sub>2</sub> and ThO<sub>2</sub>-5%UO<sub>2</sub> powders

**Table 5.4** Crystallite sizes of ThO<sub>2</sub>-10%UO<sub>2</sub> powder calculated from XRD

<b>2θ</b>	<b>FWHM</b>	<b>hkl</b>	<b>d (Å)</b>	<b>B</b>	<b>a* (Å)</b>	<b>t** (Å)</b>
25.122	1.664	(111)	3,541953	0,029042	6.1348	48,36937
30.071	1.064	(200)	2,969345	0,01857	5.9386	76,45208
43.761	1.291	(220)	2,066965	0,022532	5.8462	65,57609
52.023	1.012	(311)	1,756464	0,017663	5.8255	86,37824

\*a is lattice constant, \*\*t is crystallite size.

**Table 5.5** Crystallite sizes of ThO<sub>2</sub>-5%UO<sub>2</sub> powder calculated from XRD

<b>2θ</b>	<b>FWHM</b>	<b>hkl</b>	<b>d (Å)</b>	<b>B</b>	<b>a* (Å)</b>	<b>t** (Å)</b>
27.62	2.318	(111)	3,227023	0,040457	5.5894	34,9002
31.82	1.728	(200)	2,810011	0,030159	5.6200	47,2740
45.642	2.041	(220)	1,986059	0,035622	5.6174	41,7600
54.914	1.06	(311)	1,670633	0,0185	5.5409	83,5215

\*a is lattice constant, \*\*t is crystallite size.

The XRD patterns of the UO<sub>2</sub>, ThO<sub>2</sub>, ThO<sub>2</sub>-10%UO<sub>2</sub> and ThO<sub>2</sub>-5%UO<sub>2</sub> powders are shown in the same figure (Fig.5.11). The intensity was plotted as a function of diffraction angle, 2θ. From the XRD patterns, increasing UO<sub>2</sub> percentage in MOX powder removes the peak left side. Furthermore, there is appreciable broadening in the X-ray diffraction regions of the ThO<sub>2</sub>-10%UO<sub>2</sub> and ThO<sub>2</sub>-5%UO<sub>2</sub> powder differently from UO<sub>2</sub> and ThO<sub>2</sub>. These regions may in fact correspond to the actual size of the particles and crystalline.

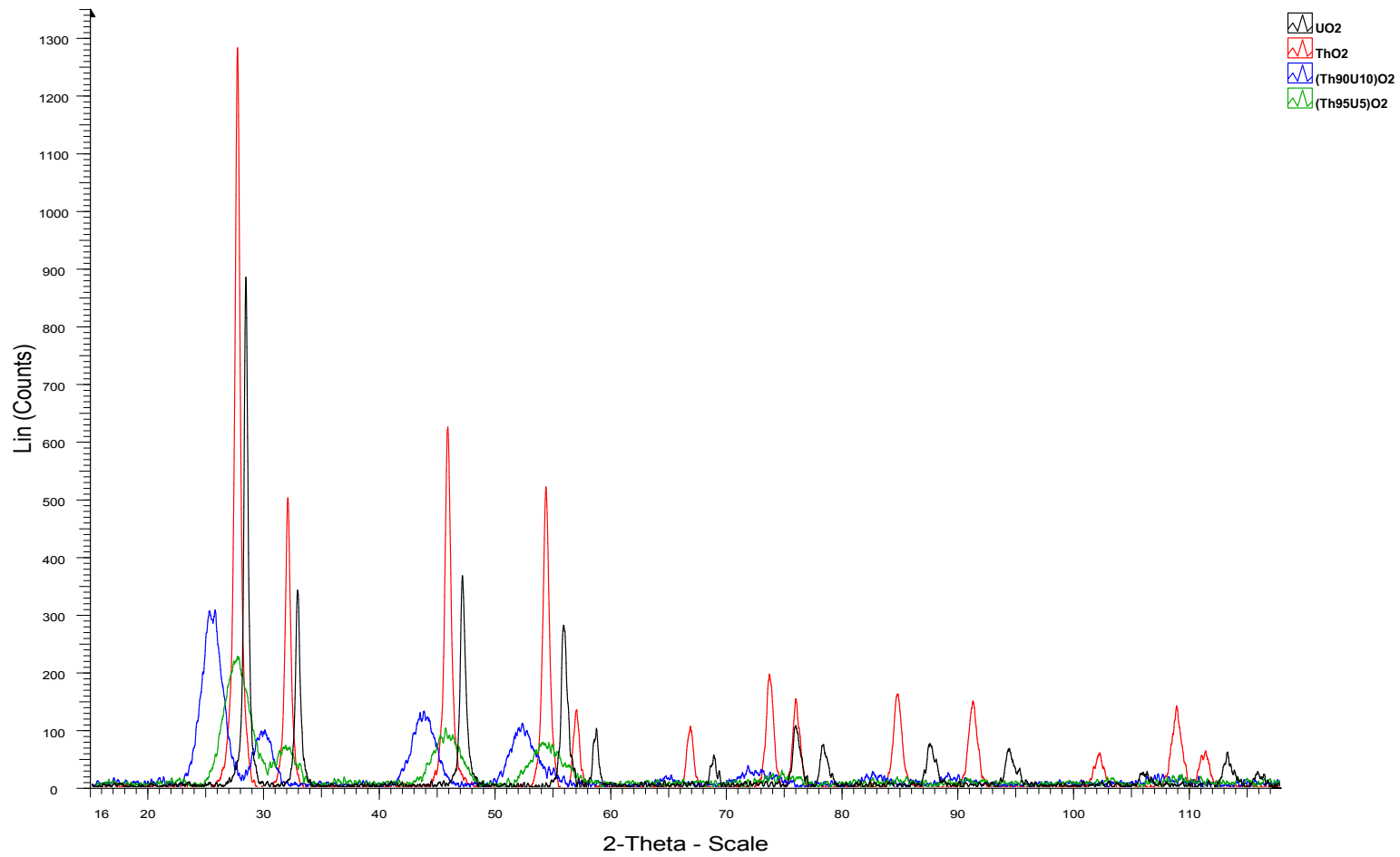


**Figure 5.11** X-Ray Diffraction patterns of UO<sub>2</sub>, ThO<sub>2</sub>, ThO<sub>2</sub>-10%UO<sub>2</sub> and ThO<sub>2</sub>-5%UO<sub>2</sub> powders

The characteristics of  $\text{UO}_2$ ,  $\text{ThO}_2$ ,  $\text{ThO}_2\text{-10\%UO}_2$  and  $\text{ThO}_2\text{-5\%UO}_2$  powders used in this study is given in Table 5.6.

**Table 5.6** Characterization of the  $\text{UO}_2$ ,  $\text{ThO}_2$ ,  $\text{ThO}_2\text{-10\%UO}_2$  and  $\text{ThO}_2\text{-5\%UO}_2$  powders

Property	$\text{UO}_2$	$\text{ThO}_2$	$\text{ThO}_2\text{-10\% UO}_2$	$\text{ThO}_2\text{-5\% UO}_2$
Theoretical density [ $\text{g/cm}^3$ ]	10.97	10	10.096	10.048
O/M ratio	2.207	2	2.167	2.254
Surface energy, $\gamma$ [ $\text{erg/cm}^2$ ]	600	1150	1095	1122.5
Specific surface area, S [ $\text{m}^2/\text{g}$ ]	6.2017	4.0683	2.5016	3.0741
Crystallite size, a [ $\text{\AA}$ ]	5.43	5.60	5.23	5.59
Particle radius, r [ $\text{\AA}$ ]	2.13	2.19	2.32	2.19
Vacancy volume, $\Omega$ [ $\text{cm}^3$ ]	$4.04 \times 10^{-23}$	$4.38 \times 10^{-23}$	$5.23 \times 10^{-23}$	$4.37 \times 10^{-23}$
Metallic impurities, [ppm]	<1000	<1000	< 1000	<1000

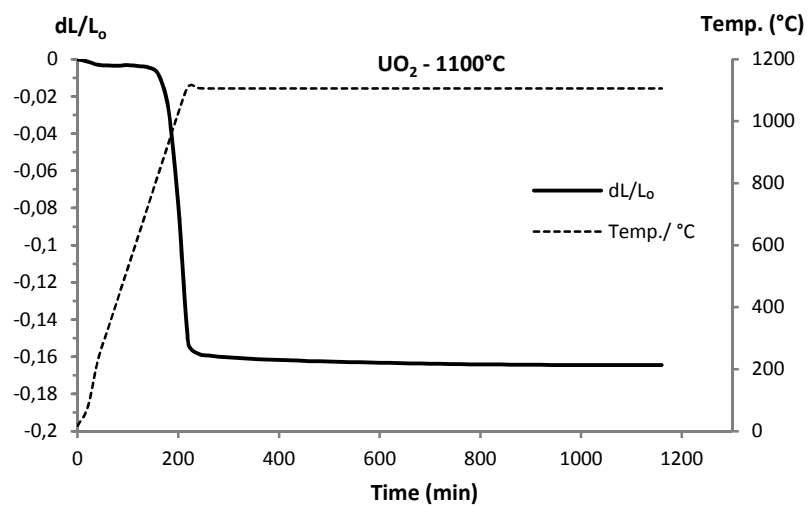
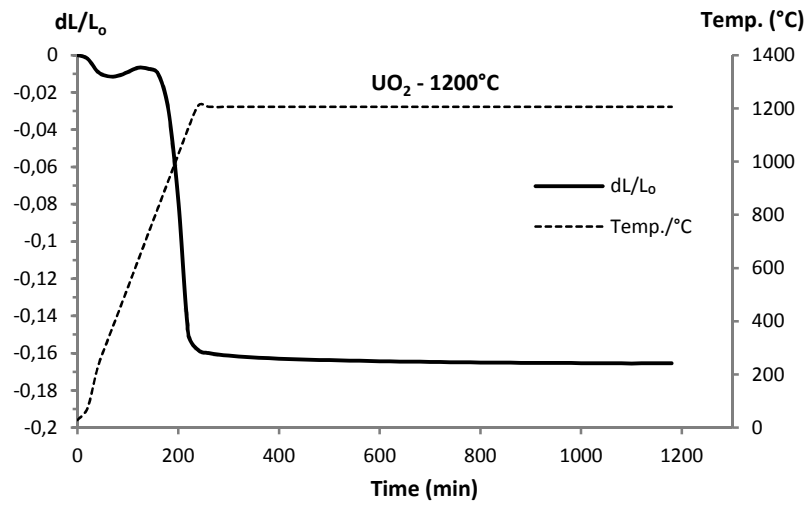
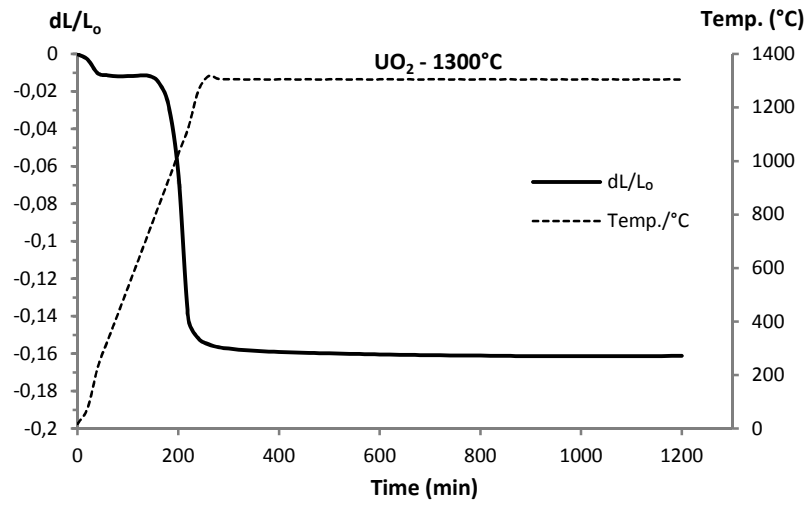
## 5.4 Investigation of Sintering Kinetics and Activation Energy

### 5.4.1 Investigation for $\text{UO}_2$ pellets

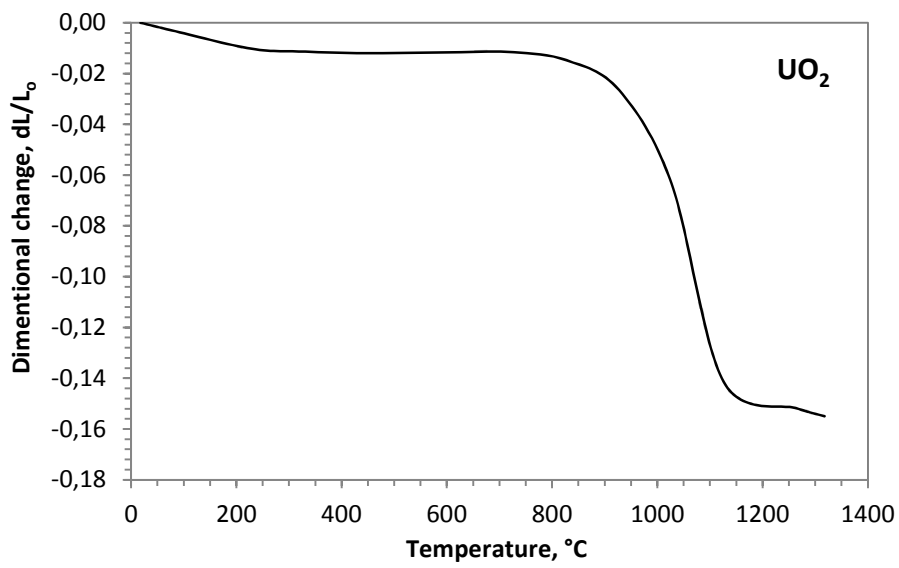
The shrinkage behaviour of the  $\text{UO}_2$  pellets in  $\text{Ar}+\%5\text{H}_2$  at  $1300^\circ\text{C}$ ,  $1200^\circ\text{C}$  and  $1100^\circ\text{C}$  temperatures are shown in Figures 5.12. The dilatometric data is obtained from the curves which  $dL/L_o$  ( $L_o$ : initial length) versus time and temperature.

Figure 5.13 shows the  $dL/L_o$  versus temperature plot of  $\text{UO}_2$  under different isothermal steps in  $\text{Ar}+\%5\text{H}_2$  atmosphere. The  $dL/L_o$  values are plotted against temperature, where  $L_o$  is the initial length of the pellet in axial direction and  $dL$  is its increment. The corresponding shrinkage rates  $d(dL/L_o)/dt$  of the these pellets are shown in Figure 5.14.

The onset temperature of shrinkage was determined from shrinkage curves by extrapolating method (as the point at which it deviates from its horizontal path). It can be seen from the Figure 5.13 that the onset of the shrinkage occurs at  $990^\circ\text{C}$  for  $\text{UO}_2$ . Figure 5.14 shows the shrinkage rate for  $\text{UO}_2$  pellets. From the shrinkage rate curves, it was observed that the maximum shrinkage rates for  $\text{UO}_2$  pellets occur at around  $1100^\circ\text{C}$ .



**Figure 5.12** Shrinkage curves of the UO<sub>2</sub> pellets in Ar+5%H<sub>2</sub> versus time and temperature sintered at 1300°C, 1200°C and 1100°C



**Figure 5.13** Shrinkage curves for  $\text{UO}_2$  pellets in  $\text{Ar}+5\% \text{H}_2$  plotted against temperature

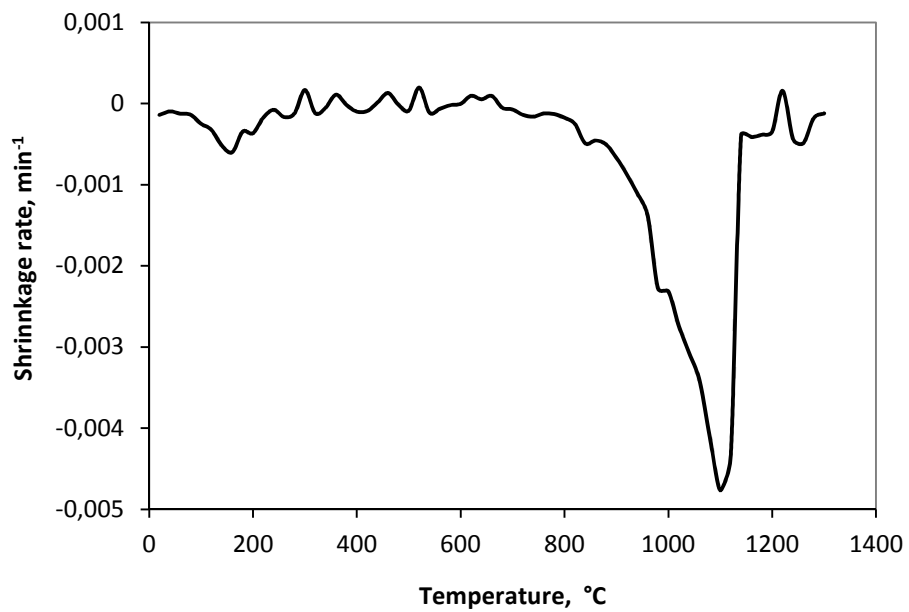


**Figure 5.14** Shrinkage rate  $d(dL/L_0)/dt$  of  $\text{UO}_2$  pellet in  $\text{Ar}+5\% \text{H}_2$  plotted against temperature, where  $L_0$  is the initial length



The  $\log \dot{Y} = \log(dY/dt)$  vs.  $\log t$  curves of the  $\text{UO}_2$  pellets at 1300°C, 1200°C and 1100°C temperatures are shown together in Figure 5.15. With the plotting  $\log(dY/dt)$  versus  $\log t$ , a straight line (slope:  $n-1$ ) was obtained for each isothermal temperature. The value of  $n$ , for the  $\text{UO}_2$  sintered pellets, was determined from the slope of the line.  $n$  is a constant whose value depends on the sintering mechanism. The value of  $n$  obtained for pellets sintered in  $\text{Ar}+5\%\text{H}_2$  is about 0.50. The mechanism for the initial stage of sintering was considered to be volume diffusion [98].

After the determination of parameter  $n$  from the straight line of the  $\log \dot{Y}$ - $\log t$  curves, the diffusion coefficient  $D$  is going to be calculated by using parameter  $n$  and Arrhenius constant,  $K(T)$ . Arrhenius constant is calculated from the intercept with  $\log \dot{Y}$  versus. Finally, the activation energies for sintering pellets are going to be calculated from the slope of the variation of  $\log D$  versus  $1/T$ .

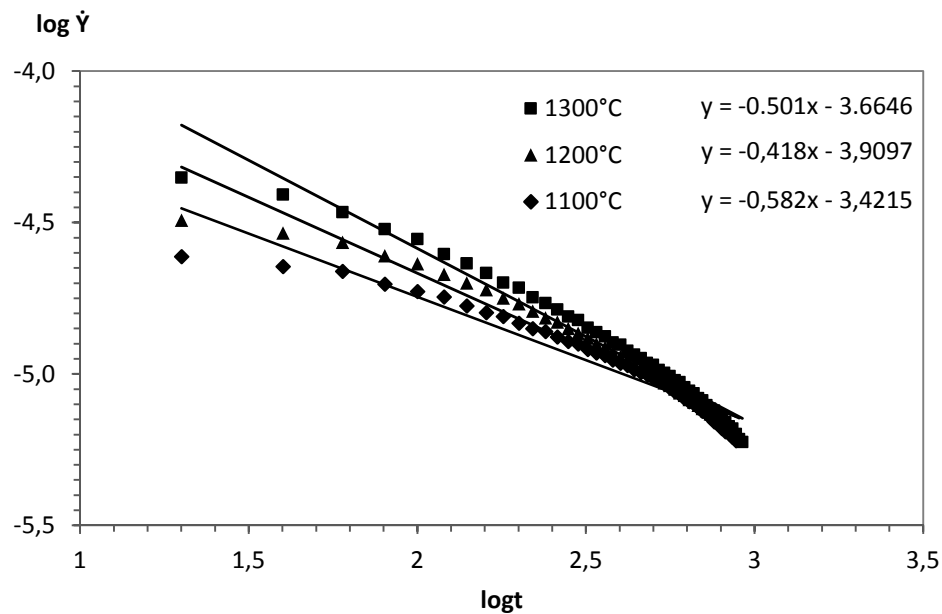


**Figure 5.15** Diffusion mechanism of  $\text{UO}_2$  in reducing  $\text{Ar}-5\%\text{H}_2$  atmosphere

The diffusion coefficients are calculated from the intercepts in Figure 5.15 using Eqs. (2.8) and (2.9) in chapter II. The values of parameters of  $\text{UO}_2$  powder used for this calculation are given in Table 5.6. The  $\ln D$  versus  $1/T$  plots for  $\text{UO}_2$  pellets in  $\text{Ar}+5\%\text{H}_2$  atmosphere are given in Figure 5.16. The slope of this curve will be  $Q/R$  from which the activation energy  $Q$  can be calculated.

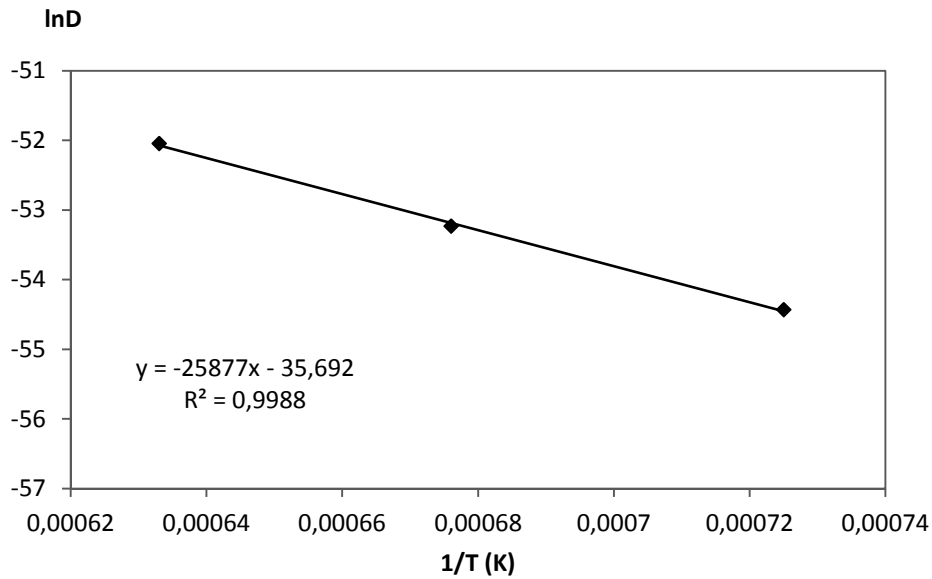


**Figure 5.16** The Arrhenius plot  $\ln D$  versus  $1/T$  for  $\text{UO}_2$  pellet sintered in  $\text{Ar}+5\% \text{H}_2$

Finally, the activation energies for sintering pellets are going to be calculated from the slope of the variation of  $\ln D$  versus  $1/T$ . The activation energy of sintering for  $\text{UO}_2$  determined from dilatometric experiments was found to be 215.140 kJ/mol in  $\text{Ar}+5\% \text{H}_2$ .

#### 5.4.2 Investigation for $\text{ThO}_2$ pellets

The shrinkage behaviour of the  $\text{ThO}_2$  pellets in  $\text{Ar}+5\% \text{H}_2$  at 1300°C, 1200°C, 1100°C and 1000°C temperatures are shown in Figures 5.17(a) and 5.17(b). The dilatometric data is obtained from the curves which  $dL/L_o$  ( $L_o$ : initial length) versus time and temperature.

Figure 5.18 shows the  $dL/L_o$  versus temperature plot of  $\text{ThO}_2$  under different isothermal steps in  $\text{Ar}+5\% \text{H}_2$  atmosphere. The  $dL/L_o$  values are plotted against temperature, where  $L_o$  is the initial length of the pellet in axial direction and  $dL$  is its increment. The corresponding shrinkage rates  $d(dL/L_o)/dt$  of these pellets are shown in Figure 5.19.

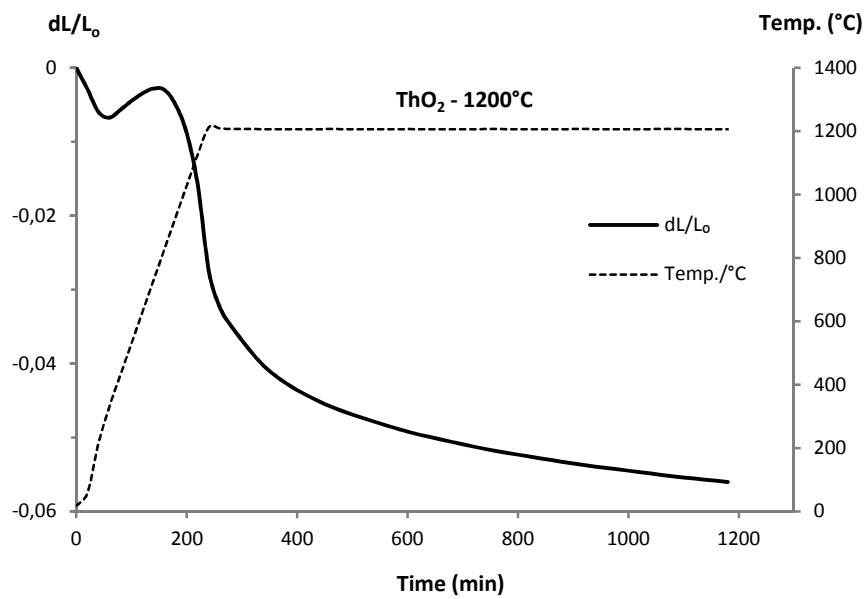
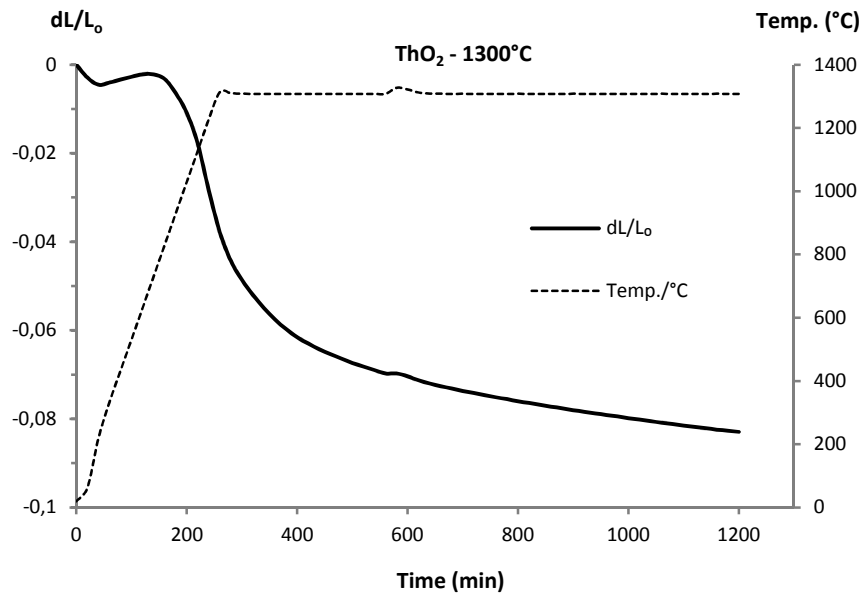


**Figure 5.17(a)** Shrinkage curves of the ThO<sub>2</sub> pellets in Ar+%5H<sub>2</sub> versus time and temperature sintered at 1300°C and 1200°C

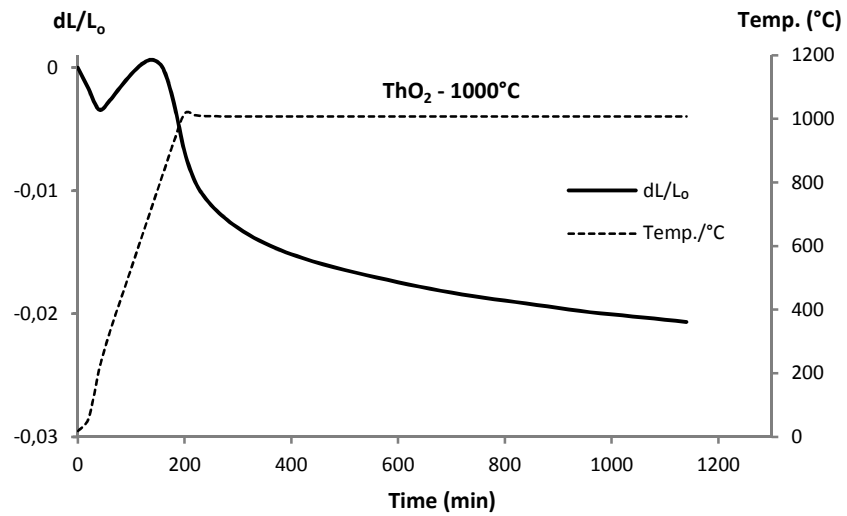
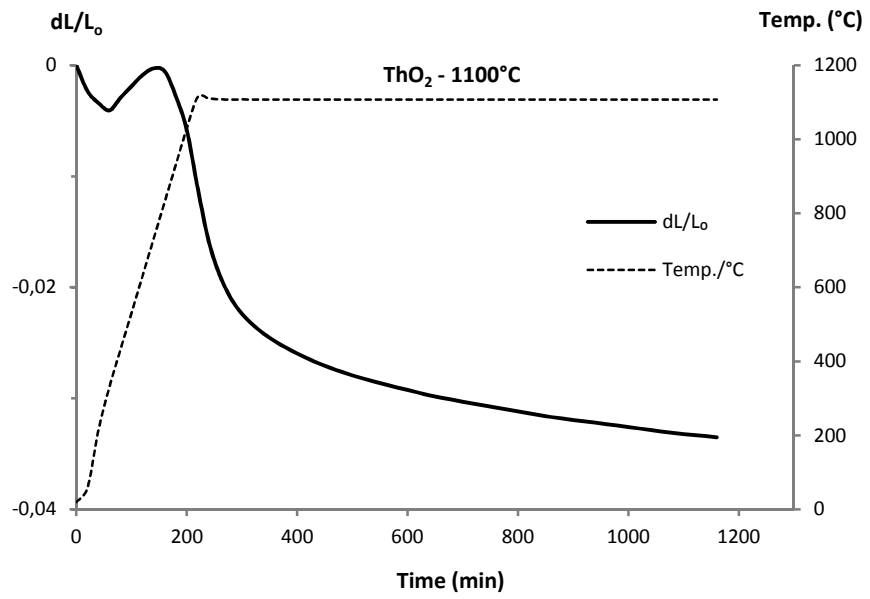


**Figure 5.17(b)** Shrinkage curves of the ThO<sub>2</sub> pellets in Ar+%5H<sub>2</sub> versus time and temperature sintered at 1100°C and 1000°C

The onset temperature of shrinkage was determined from shrinkage curves by extrapolating method (as the point at which it deviates from its horizontal path). It can be seen from the Figure 5.18 that the onset of the shrinkage occurs at 800°C for ThO<sub>2</sub>. Figure 5.19 shows the shrinkage rate for ThO<sub>2</sub> pellets. From the shrinkage rate curves, it was observed that the maximum shrinkage rates for ThO<sub>2</sub> pellets occur at around 1160°C.

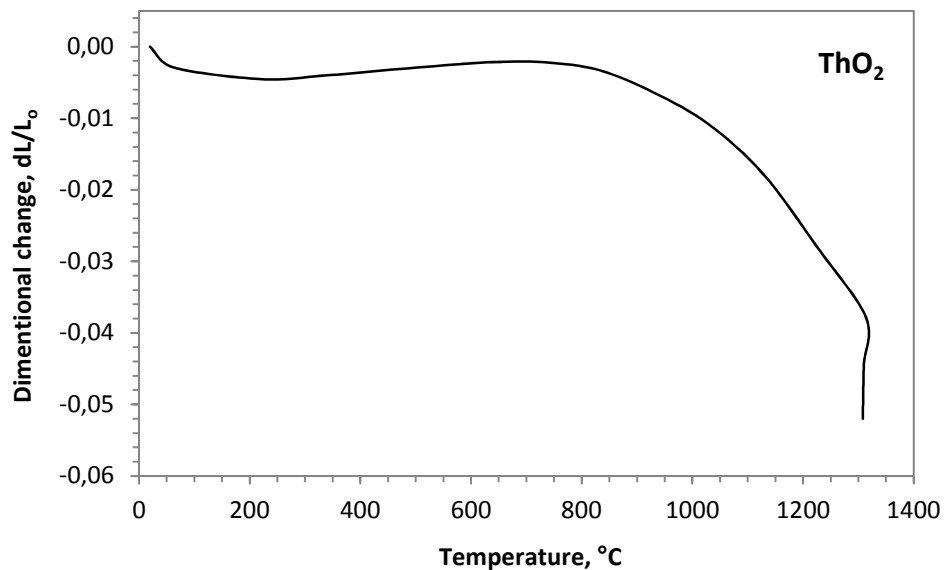


**Figure 5.18** Shrinkage curves for ThO<sub>2</sub> pellets in Ar+5%H<sub>2</sub> versus temperature

The  $\log \dot{Y} = \log(dY/dt)$  vs.  $\log t$  curves of the ThO<sub>2</sub> pellets at 1300°C, 1200°C, 1100°C and 1000°C temperatures are shown together in Figure 5.20. With the plotting  $\log(dY/dt)$  versus  $\log t$ , a straight line (slope:  $n-1$ ) was obtained for each isothermal temperature. The value of  $n$ , for the ThO<sub>2</sub> sintered pellets, was determined from the slope of the line.  $n$  is a constant whose value depends on the sintering mechanism. The value of  $n$  obtained for pellets sintered in Ar+5%H<sub>2</sub> is about 0.58. The mechanism for the initial stage of sintering was considered to be volume diffusion [98].

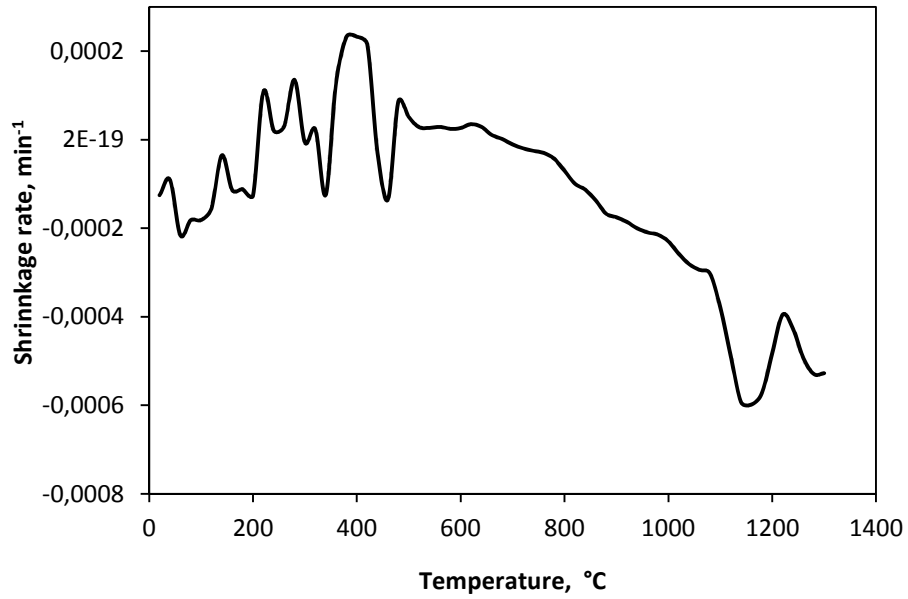


**Figure 5.19** Shrinkage rate  $d(L/L_0)/dt$  of  $\text{ThO}_2$  pellet in  $\text{Ar}+5\%\text{H}_2$  plotted against temperature, where  $L_0$  is the initial length.

After the determination of parameter  $n$  from the straight line of the  $\log \dot{Y}$ - $\log t$  curves, the diffusion coefficient  $D$  is going to be calculated by using parameter  $n$  and Arrhenius constant,  $K(T)$ . Arrhenius constant is calculated from the intercept with  $\log \dot{Y}$  versus. Finally, the activation energies for sintering pellets are going to be calculated from the slope of the variation of  $\log D$  versus  $1/T$ .

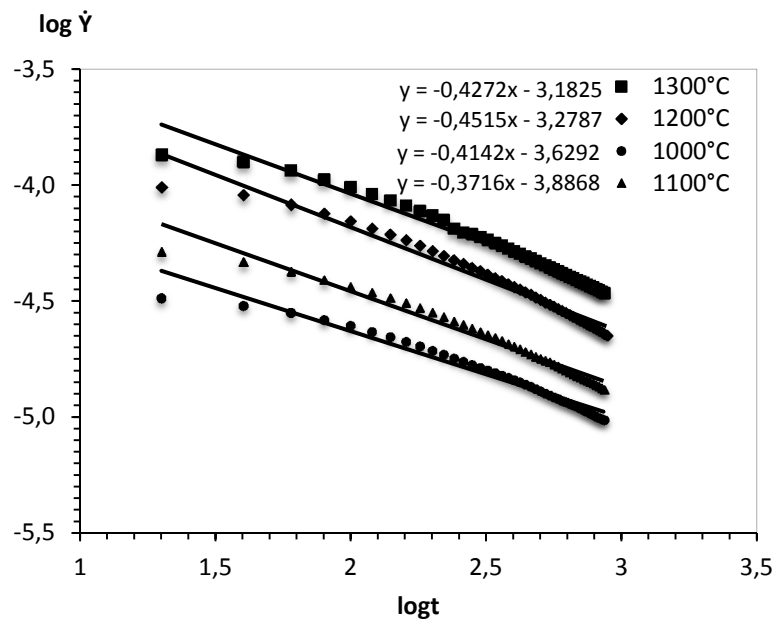


**Figure 5.20** Diffusion mechanism of  $\text{ThO}_2$  in reducing  $\text{Ar}-5\%\text{H}_2$  atmosphere.

The diffusion coefficients are calculated from the intercepts in Figure 5.20 using Eqs. (2.8) and (2.9). The values of parameters of ThO<sub>2</sub> powder used for this calculation are given in Table 5.6. The ln*D* versus 1/*T* plots for ThO<sub>2</sub> pellets in Ar+5%H<sub>2</sub> atmosphere are given in Figure 5.21. The slope of this curve will be *Q*/*R* from which the activation energy *Q* can be calculated.

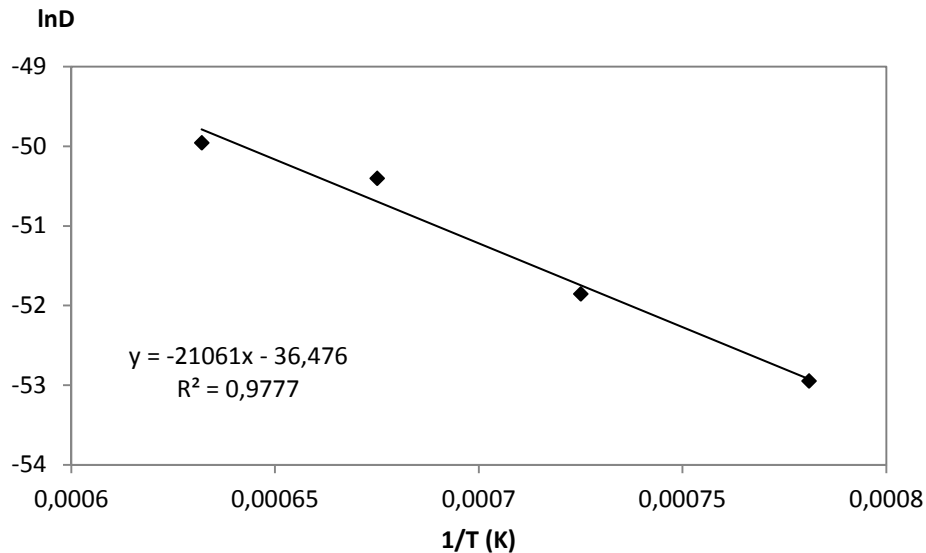


**Figure 5.21** The Arrhenius plot ln*D* versus 1/*T* for ThO<sub>2</sub> pellet sintered in Ar+5%H<sub>2</sub>. Finally, the activation energies for sintering pellets are going to be calculated from the slope of the variation of ln*D* versus 1/*T*. The activation energy of sintering for ThO<sub>2</sub> determined from dilatometric experiments was found to be 175.105 kJ/mol for Ar+5%H<sub>2</sub>.

#### 5.4.3 Investigation for ThO<sub>2</sub>-10%UO<sub>2</sub> pellets

The shrinkage behaviour of the ThO<sub>2</sub>-10%UO<sub>2</sub> pellets in Ar+5%H<sub>2</sub> at 1200°C, 1100°C and 1000°C temperatures are shown in Figure 5.22. The dilatometric data is obtained from the curves which *dL*/*L<sub>o</sub>* (*L<sub>o</sub>*: initial length) versus time and temperature.

Figure 5.23 shows the *dL*/*L<sub>o</sub>* versus temperature plot of ThO<sub>2</sub>-10%UO<sub>2</sub> under different isothermal steps in Ar+5%H<sub>2</sub> atmosphere. The *dL*/*L<sub>o</sub>* values are plotted against temperature, where *L<sub>o</sub>* is the initial length of the pellet in axial direction and *dL* is its increment. The corresponding shrinkage rates *d*(*dL*/*L<sub>o</sub>*)/*dt* of these pellets are shown in Figure 5.24.

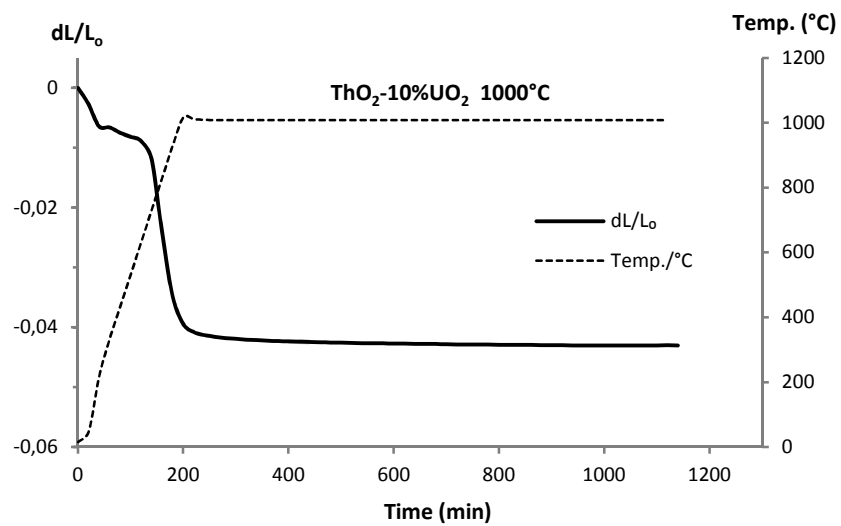
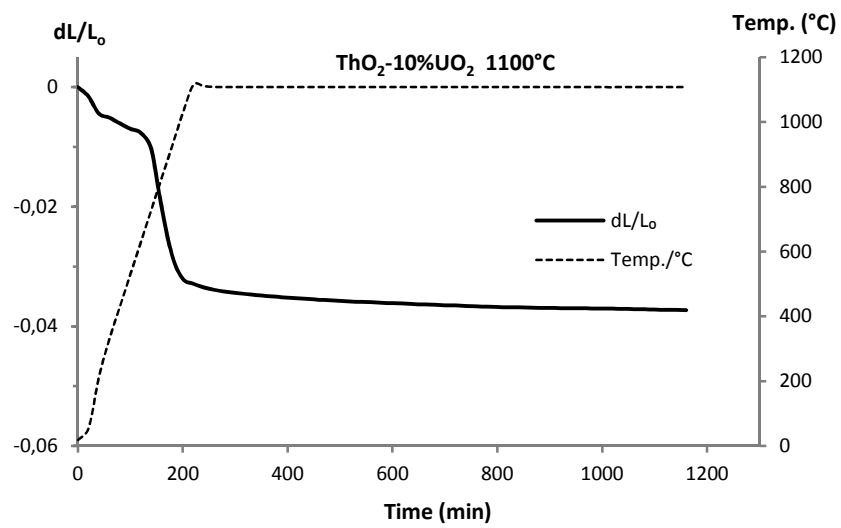
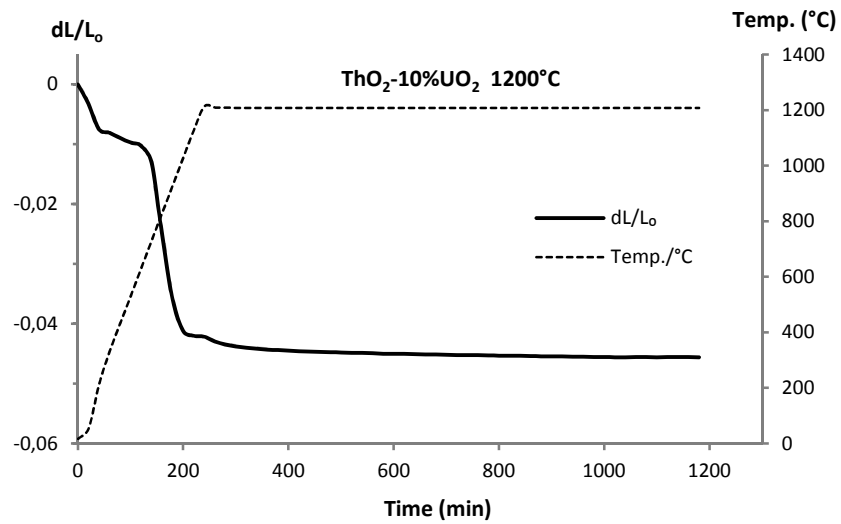


**Figure 5.22** Shrinkage curves of the ThO<sub>2</sub>-10%UO<sub>2</sub> pellets in Ar+%5H<sub>2</sub> versus time and temperature sintered at 1200°C, 1100°C and 1000°C



The onset temperature of shrinkage was determined from shrinkage curves by extrapolating method (as the point at which it deviates from its horizontal path). It can be seen from the Figure 5.23 that the onset of the shrinkage occurs at 735°C for ThO<sub>2</sub>-10%UO<sub>2</sub>. Figure 5.24 shows the shrinkage rate for ThO<sub>2</sub>-10%UO<sub>2</sub> pellets. From the shrinkage rate curves, it was observed that the maximum shrinkage rates for ThO<sub>2</sub>-10%UO<sub>2</sub> pellets occur at around 840°C.

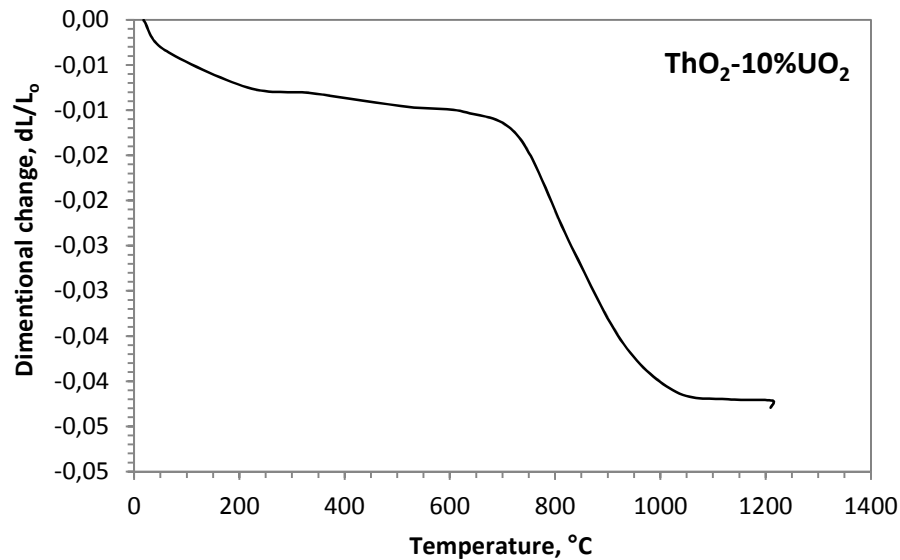


**Figure 5.23** Shrinkage curves for ThO<sub>2</sub>-10%UO<sub>2</sub> pellets in Ar+5%H<sub>2</sub> versus temperature

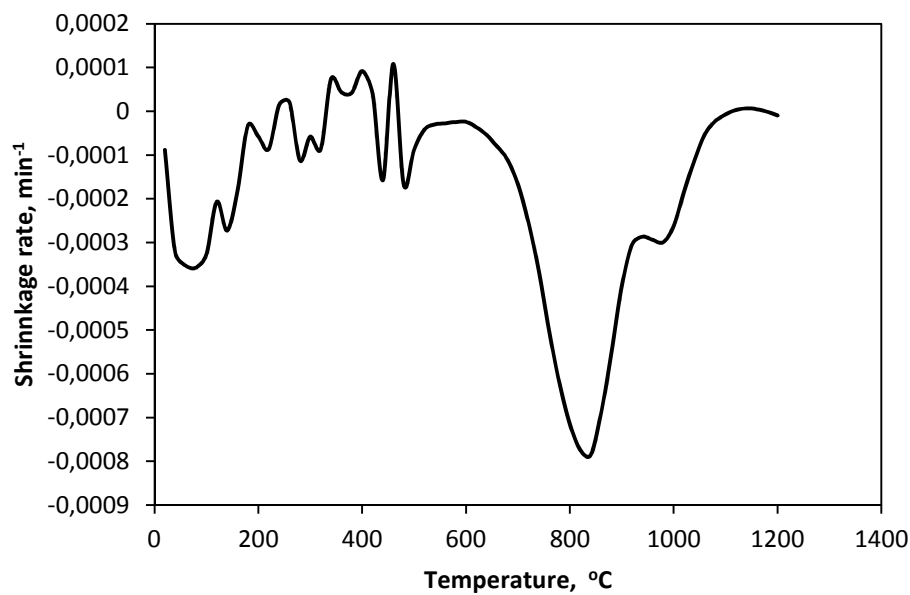


**Figure 5.24** Shrinkage rate  $d(dL/L_0)/dt$  of ThO<sub>2</sub>-10%UO<sub>2</sub> pellet in Ar+5%H<sub>2</sub> plotted against temperature, where  $L_0$  is the initial length.

The  $\log \dot{Y} = \log(dY/dt)$  vs.  $\log t$  curves of the  $\text{ThO}_2$ -10% $\text{UO}_2$  pellets at 1200°C, 1100°C and 1000°C temperatures are shown together in Figure 5.25. With the plotting  $\log(dY/dt)$  versus  $\log t$ , a straight line (slope:  $n-1$ ) was obtained for each isothermal temperature. The value of  $n$ , for the  $\text{ThO}_2$ -10% $\text{UO}_2$  sintered pellets, was determined from the slope of the line.  $n$  is a constant whose value depends on the sintering mechanism. The value of  $n$  obtained for pellets sintered in  $\text{Ar}+5\%\text{H}_2$  is about 0.53. The mechanism for the initial stage of sintering was considered to be volume diffusion [98].

After the determination of parameter  $n$  from the straight line of the  $\log \dot{Y}$ - $\log t$  curves, the diffusion coefficient  $D$  is going to be calculated by using parameter  $n$  and Arrhenius constant,  $K(T)$ . Arrhenius constant is calculated from the intercept with  $\log \dot{Y}$  versus. Finally, the activation energies for sintering pellets are going to be calculated from the slope of the variation of  $\log D$  versus  $1/T$ .

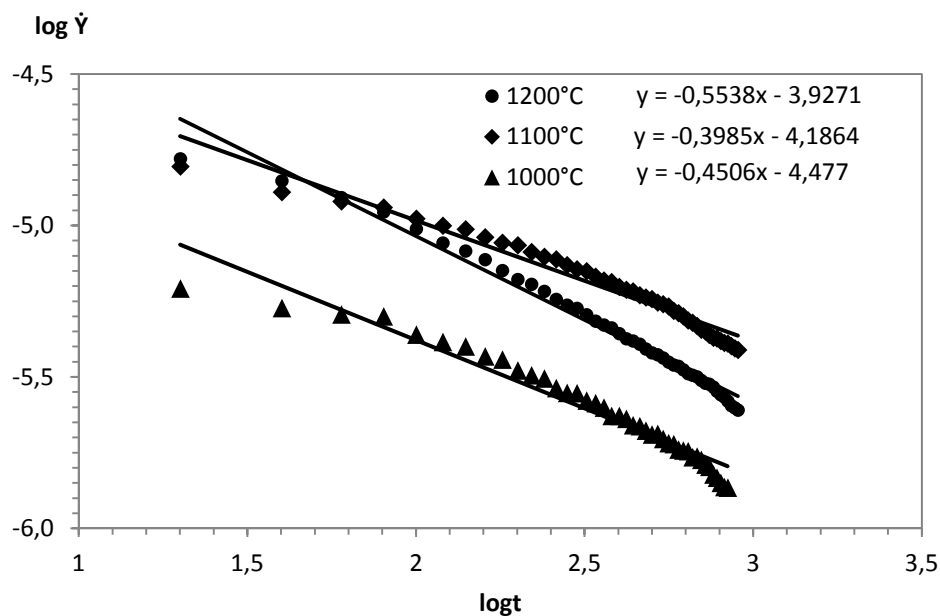


**Figure 5.25** Diffusion mechanism of  $\text{ThO}_2$ -10% $\text{UO}_2$  in reducing  $\text{Ar}+5\%\text{H}_2$  atmosphere.

The diffusion coefficients are calculated from the intercepts in Figure 5.25 using Eqs. (2.8) and (2.9) in chapter II. The values of parameters of  $\text{ThO}_2$ -10% $\text{UO}_2$  powder used for this calculation are given in Table 5.6. The  $\ln D$  versus  $1/T$  plots for  $\text{ThO}_2$ -10% $\text{UO}_2$  pellets in  $\text{Ar}+5\%\text{H}_2$  atmosphere are given in Figure 5.26. The slope of this curve will be  $Q/R$  from which the activation energy  $Q$  can be calculated.

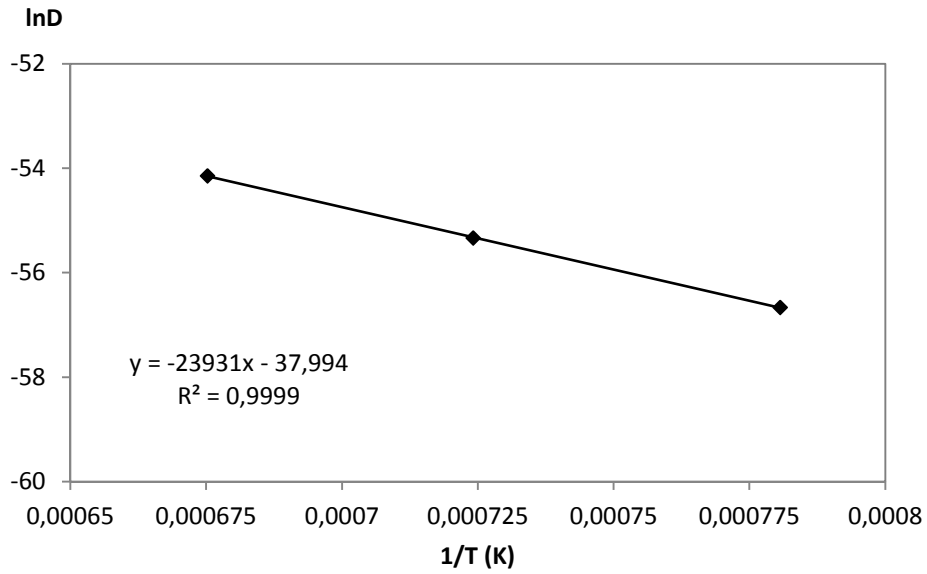


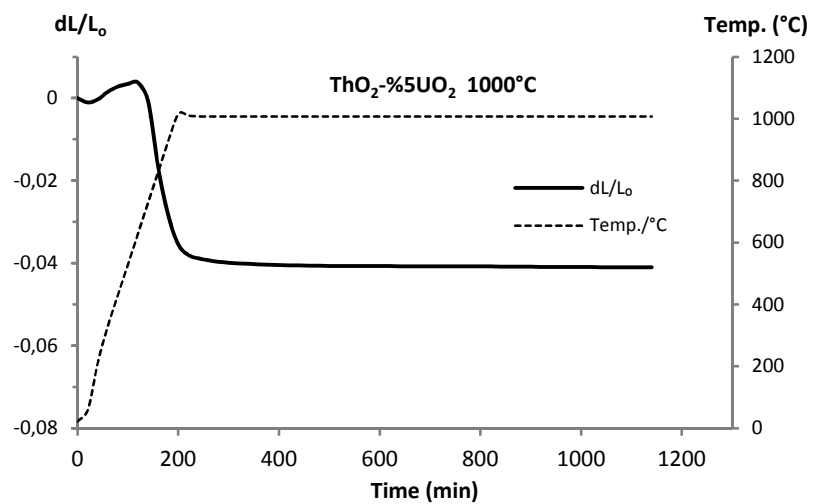
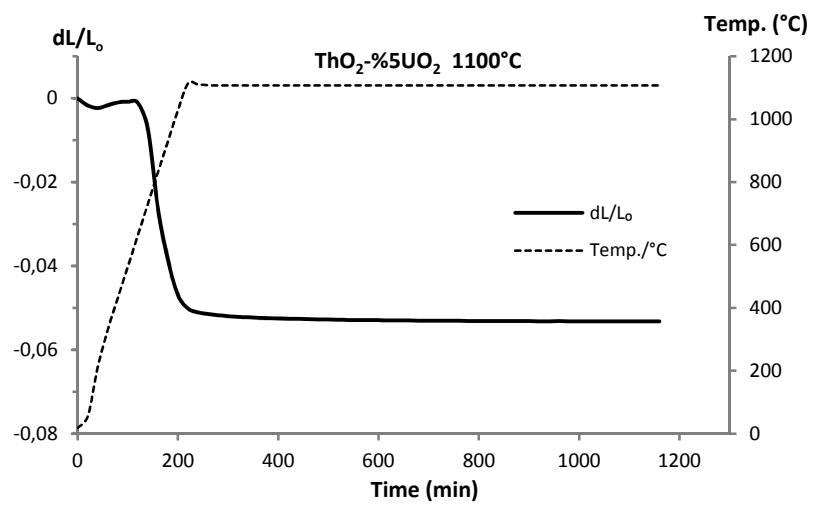
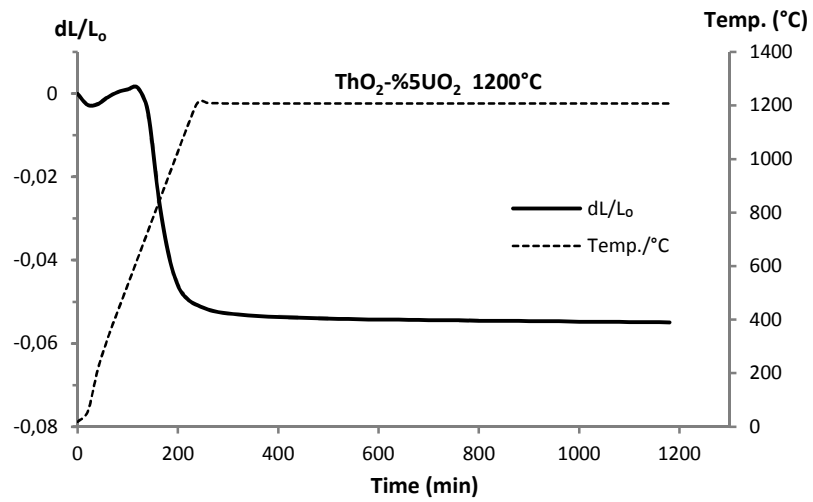
**Figure 5.26** The Arrhenius plot  $\ln D$  versus  $1/T$  for  $\text{ThO}_2$ -10% $\text{UO}_2$  pellet sintered in  $\text{Ar}+5\%\text{H}_2$ .

Finally, the activation energies for sintering pellets are going to be calculated from the slope of the variation of  $\ln D$  versus  $1/T$ . The activation energy of sintering for  $\text{ThO}_2$ -10% $\text{UO}_2$  determined from dilatometric experiments was found to be 198.961 kJ/mol for  $\text{Ar}+5\%\text{H}_2$ .

#### 5.4.4 Investigation for $\text{ThO}_2$ -5% $\text{UO}_2$ pellets

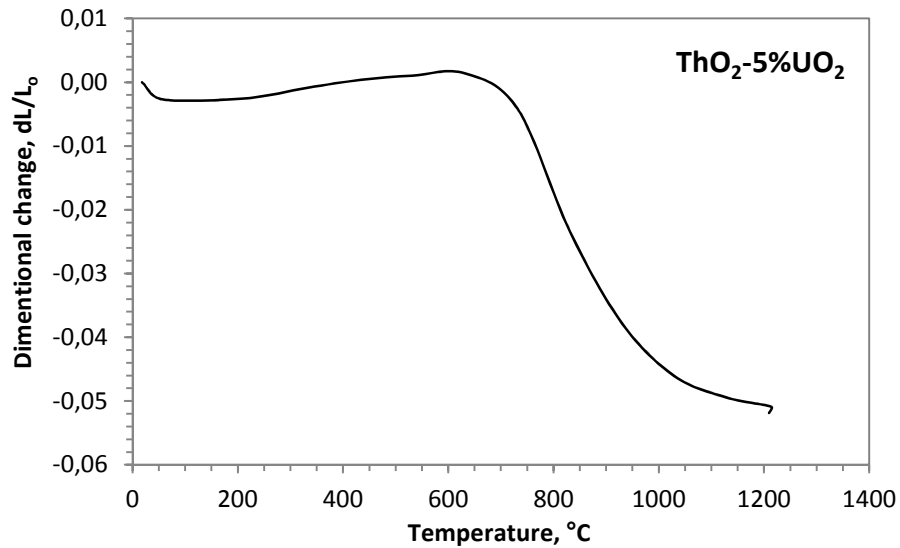
The shrinkage behaviour of the  $\text{ThO}_2$ -5% $\text{UO}_2$  pellets in  $\text{Ar}+5\%\text{H}_2$  at 1200°C, 1100°C and 1000°C temperatures are shown in Figure 5.27. The dilatometric data is obtained from the curves which  $dL/L_o$  ( $L_o$ : initial length) versus time and temperature.

Figure 5.28 shows the  $dL/L_o$  versus temperature plot of  $\text{ThO}_2$ -5% $\text{UO}_2$  under different isothermal steps in  $\text{Ar}+5\%\text{H}_2$  atmosphere. The  $dL/L_o$  values are plotted against temperature, where  $L_o$  is the initial length of the pellet in axial direction and  $dL$  is its increment. The corresponding shrinkage rates  $d(dL/L_o)/dt$  of these pellets are shown in Figure 5.29.



**Figure 5.27** Shrinkage curves of the ThO<sub>2</sub>-5%UO<sub>2</sub> pellets in Ar+5%H<sub>2</sub> versus time and temperature sintered at 1200°C, 1100°C and 1000°C

The onset temperature of shrinkage was determined from shrinkage curves by extrapolating method (as the point at which it deviates from its horizontal path). It can be seen from the Figure 5.28 that the onset of the shrinkage occurs at 707°C for ThO<sub>2</sub>-5%UO<sub>2</sub>. Figure 5.29 shows the shrinkage rate for ThO<sub>2</sub>-5%UO<sub>2</sub> pellets. From the shrinkage rate curves, it was observed that the maximum shrinkage rates for ThO<sub>2</sub>-5%UO<sub>2</sub> pellets occur at around 800°C.



**Figure 5.28** Shrinkage curves for ThO<sub>2</sub>-5%UO<sub>2</sub> pellets in Ar+5%H<sub>2</sub> versus temperature

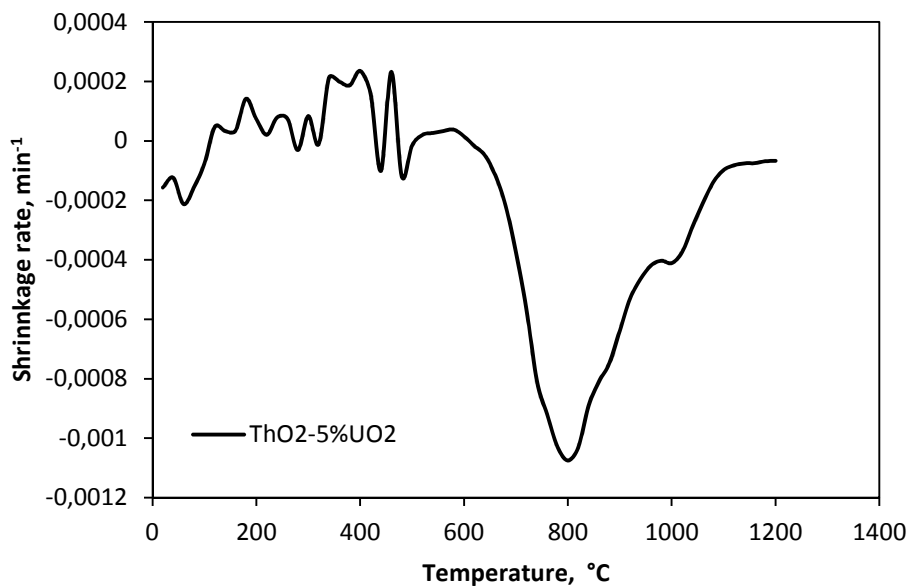


**Figure 5.29** Shrinkage rate  $d(dL/L_0)/dt$  of ThO<sub>2</sub>-5%UO<sub>2</sub> pellet in Ar+5%H<sub>2</sub> plotted against temperature, where  $L_0$  is the initial length

The  $\log \dot{Y} = \log(dY/dt)$  vs.  $\log t$  curves of the  $\text{ThO}_2\text{-5\%UO}_2$  pellets at  $1200^\circ\text{C}$ ,  $1100^\circ\text{C}$  and  $1000^\circ\text{C}$  temperatures are shown together in Figure 5.30. With the plotting  $\log(dY/dt)$  versus  $\log t$ , a straight line (slope:  $n-1$ ) was obtained for each isothermal temperature. The value of  $n$ , for the  $\text{ThO}_2\text{-5\%UO}_2$  sintered pellets, was determined from the slope of the line.  $n$  is a constant whose value depends on the sintering mechanism. The value of  $n$  obtained for pellets sintered in  $\text{Ar+5\% H}_2$  is about 0.45. The mechanism for the initial stage of sintering was considered to be volume diffusion [98].

After the determination of parameter  $n$  from the straight line of the  $\log \dot{Y}\text{-}\log t$  curves, the diffusion coefficient  $D$  is going to be calculated by using parameter  $n$  and Arrhenius constant,  $K(T)$ . Arrhenius constant is calculated from the intercept with  $\log \dot{Y}$  versus. Finally, the activation energies for sintering pellets are going to be calculated from the slope of the variation of  $\log D$  versus  $1/T$ .

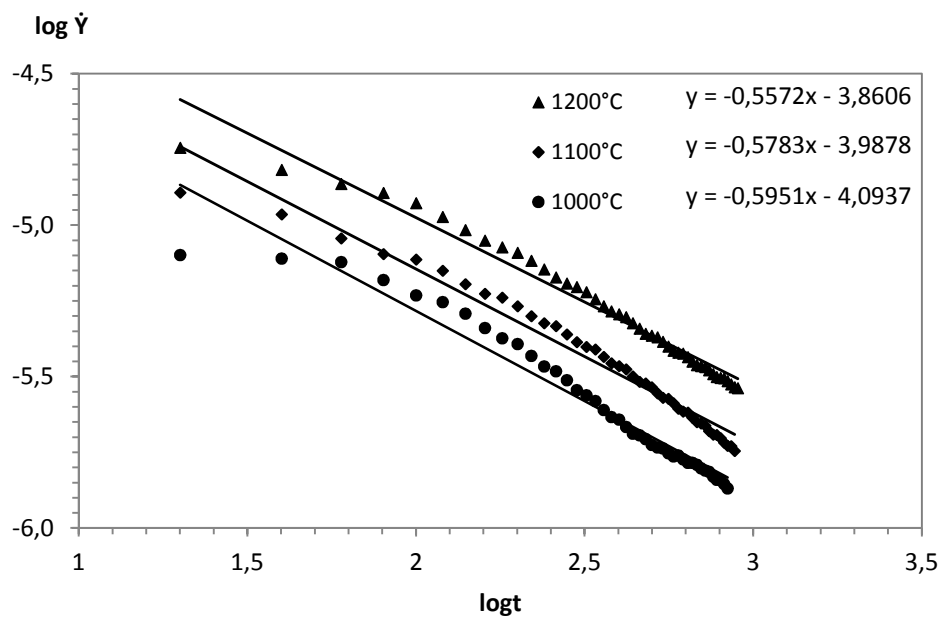


**Figure 5.30** Diffusion mechanism of  $\text{ThO}_2\text{-5\%UO}_2$  in reducing  $\text{Ar-5\%H}_2$  atmosphere.

The diffusion coefficients are calculated from the intercepts in Figure 5.30 using Eqs. (2.8) and (2.9) in chapter II. The values of parameters of  $\text{ThO}_2\text{-5\%UO}_2$  powder used for this calculation are given in Table 5.6. The  $\ln D$  versus  $1/T$  plots for  $\text{ThO}_2\text{-5\%UO}_2$  pellets in  $\text{Ar+5\%H}_2$  atmosphere are given in Figure 5.31. The slope of this curve will be  $Q/R$  from which the activation energy  $Q$  can be calculated.

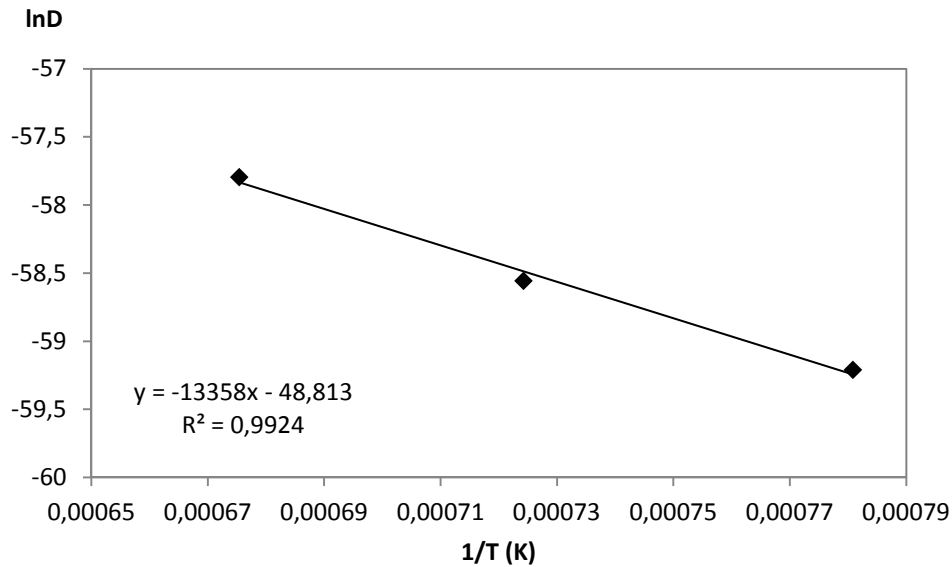


**Figure 5.31** The Arrhenius plot  $\ln D$  versus  $1/T$  for  $\text{ThO}_2$ -5% $\text{UO}_2$  pellet sintered in  $\text{Ar}+5\% \text{H}_2$

Finally, the activation energies for sintering pellets are going to be calculated from the slope of the variation of  $\ln D$  versus  $1/T$ . The activation energy of sintering for  $\text{ThO}_2$ -5% $\text{UO}_2$  determined from dilatometric experiments was found to be 111.056 kJ/mol for  $\text{Ar}+5\% \text{H}_2$ .

Figure 5.32 and 5.33 show the typical shrinkage behaviour of pure urania and thoria, and two different compositions of urania-thoria pellets in the same figure as a function of temperature in reducing  $\text{Ar}+5\% \text{H}_2$  atmosphere under constant heating rate of  $5^\circ\text{C}/\text{min}$ .

The onset temperature of sintering was determined from the dilatometric curve as the point at which it deviated from its horizontal path. The onset of sintering was found marginally shift to lower temperature on decreasing the  $\text{UO}_2$  content (Figure 5.32). This occurs at temperatures 735 and  $707^\circ\text{C}$ , for compositions  $\text{ThO}_2$ -10% $\text{UO}_2$  and  $\text{ThO}_2$ -5% $\text{UO}_2$ , respectively. The onset of sintering for pure  $\text{ThO}_2$  occurs at  $800^\circ\text{C}$  which is higher than the urania-thoria pellets, but pure  $\text{UO}_2$  is much higher occurs at  $990^\circ\text{C}$ .

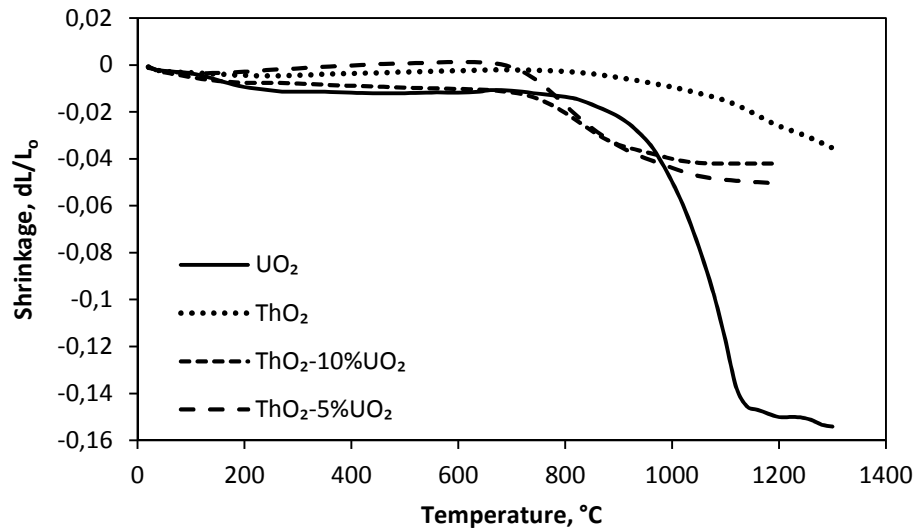


**Figure 5.32** Shrinkage behaviour on heating in Ar+5%H<sub>2</sub> Atmosphere. Curves of UO<sub>2</sub>, ThO<sub>2</sub>, ThO<sub>2</sub>-10%UO<sub>2</sub> and ThO<sub>2</sub>-5%UO<sub>2</sub> are shown.

The temperature, at which the maximum shrinkage rate occurs for a particular composition, was observed to shift lower temperatures with decrease in UO<sub>2</sub> content as shown in Figure 5.33. This occurs at temperatures 840 and 800°C, for compositions ThO<sub>2</sub>-10%UO<sub>2</sub> and ThO<sub>2</sub>-5%UO<sub>2</sub>, respectively. The maximum shrinkage rates for pure UO<sub>2</sub> and ThO<sub>2</sub> are higher than the urania-thoria pellets occur at 1100 and 1160°C, respectively. Moreover, the maximum pellet shrinkage at a particular temperature is found for pure UO<sub>2</sub> while the minimum for pure ThO<sub>2</sub>.

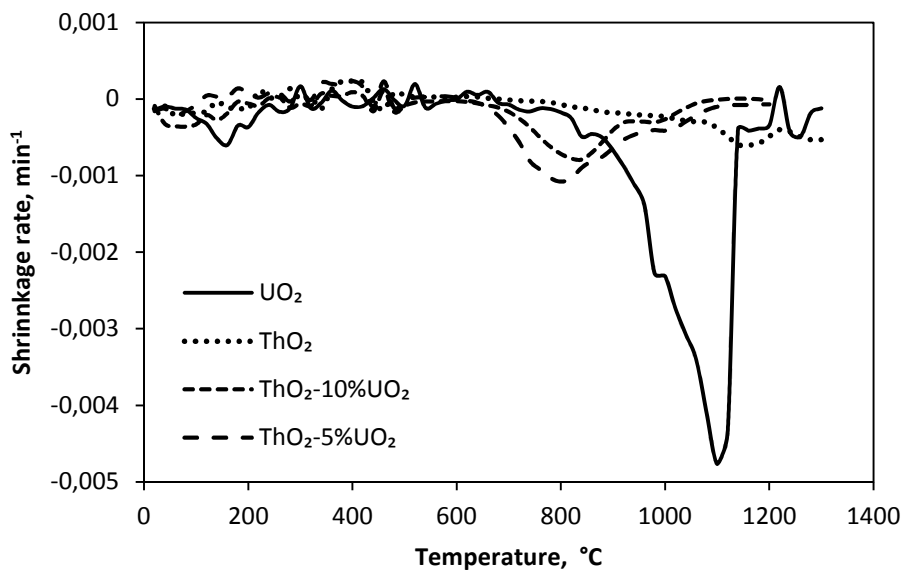


**Figure 5.33** Shrinkage rate for UO<sub>2</sub>, ThO<sub>2</sub>, ThO<sub>2</sub>-10%UO<sub>2</sub> and ThO<sub>2</sub>-5%UO<sub>2</sub> pellets heated in Ar+5%H<sub>2</sub> Atmosphere plotted against temperature.



The Table 5.7 shows the diffusion parameters ( $A$ ,  $n$  and  $p$ ), the diffusion coefficients and activation energy values of the sintered  $\text{UO}_2$ ,  $\text{ThO}_2$ , and  $\text{ThO}_2$ -10% $\text{UO}_2$  and  $\text{ThO}_2$ -5% $\text{UO}_2$  pellets.  $A$ ,  $n$  and  $p$  are the constants whose values depend on the sintering mechanism. The constants,  $A$  and  $p$  were obtained from the PhD. Thesis (1979) of M.M. El-Sayed Ali [98]

**Table 5.7** The diffusion mechanism characteristics ( $A$ ,  $n$  and  $p$ ), diffusion coefficients and activation energy values of the sintered  $\text{UO}_2$ ,  $\text{ThO}_2$ ,  $\text{ThO}_2$ -10% $\text{UO}_2$  and  $\text{ThO}_2$ -5% $\text{UO}_2$  pellets.

	T(°C)	$A^*$	$n$	$p^*$	K(T)	D(cm <sup>2</sup> /s)	Q(kJ/mol)
<b>UO<sub>2</sub></b>	1306				5.742x10 <sup>-7</sup>	2.49x10 <sup>-23</sup>	
	1206	2	0.50	3	1.874x10 <sup>-7</sup>	7.61x10 <sup>-24</sup>	215.14
	1106				6.063x10 <sup>-8</sup>	2.30x10 <sup>-24</sup>	
<b>ThO<sub>2</sub></b>	1308				8.905x10 <sup>-6</sup>	2.02x10 <sup>-22</sup>	
	1208	2	0.58	3	6.093x10 <sup>-6</sup>	1.29x10 <sup>-22</sup>	175.105
	1108				1.529x10 <sup>-6</sup>	3.03x10 <sup>-23</sup>	
	1008				5.538x10 <sup>-7</sup>	1.02x10 <sup>-23</sup>	
<b>ThO<sub>2</sub>-10%UO<sub>2</sub></b>	1208				1.371 x10 <sup>-7</sup>	3.06x10 <sup>-24</sup>	
	1108	2	0.53	3	4.468x10 <sup>-8</sup>	9.29x10 <sup>-25</sup>	198.961
	1008				1.271 x10 <sup>-8</sup>	2.45x10 <sup>-25</sup>	
<b>ThO<sub>2</sub>-5%UO<sub>2</sub></b>	1208				5.732x10 <sup>-9</sup>	7.93x10 <sup>-26</sup>	
	1108	31/ $\pi^2$	0.44	3	2.870x10 <sup>-9</sup>	3.70 x10 <sup>-26</sup>	111.056
	1008				1.613x10 <sup>-9</sup>	1.93x10 <sup>-26</sup>	

\* $A$  and  $p$  obtained from PhD. Thesis of M.M. El-Sayed Ali (1979) [98]

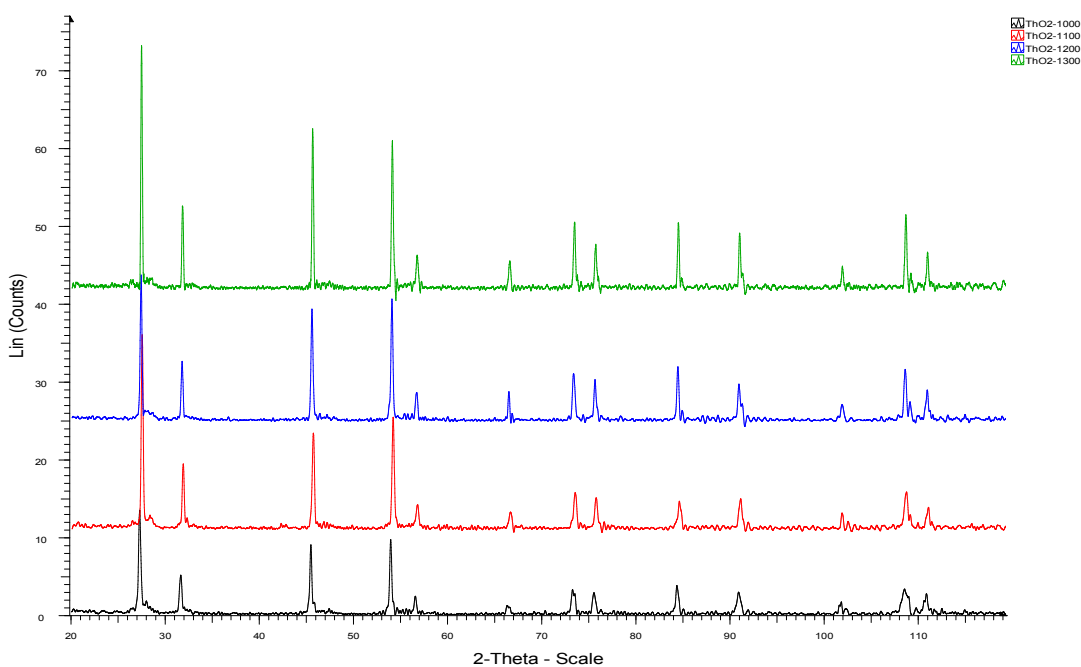
The activation energies of  $\text{UO}_2$ ,  $\text{ThO}_2$ ,  $\text{ThO}_2$ -10% $\text{UO}_2$  and  $\text{ThO}_2$ -5% $\text{UO}_2$  for the initial stages of sintering obtained in this study using dilatometry have shown that the mechanism for the initial stage of sintering for all the pellet groups were considered to be volume diffusion. Our results are contrary to the results reported [70,119] where the authors had reported that the grain boundary diffusion is the rate controlling mechanism in reducing atmosphere  $\text{ThO}_2$ - $\text{UO}_2$  pellets. Aybers has carried out RCS (Rate Controlled Sintering) technique on  $\text{UO}_2$ ,  $(\text{U,Th})\text{O}_2$ ,  $(\text{U,Pu})\text{O}_2$  [71,72] and reported that the mechanism changes with atmosphere used for sintering. He has proposed that the mechanisms during initial stage of sintering are volume and grain

boundary diffusion in reducing and oxidising atmospheres, respectively. El-Sayed Ali and Sorensen [120,121] have found  $n=0.32$  in  $\text{CO}_2$  atmosphere for  $(\text{U,Pu})\text{O}_2$  and  $n=0.45$  in reducing atmosphere. Our results agree with this observation in reducing atmospheres.

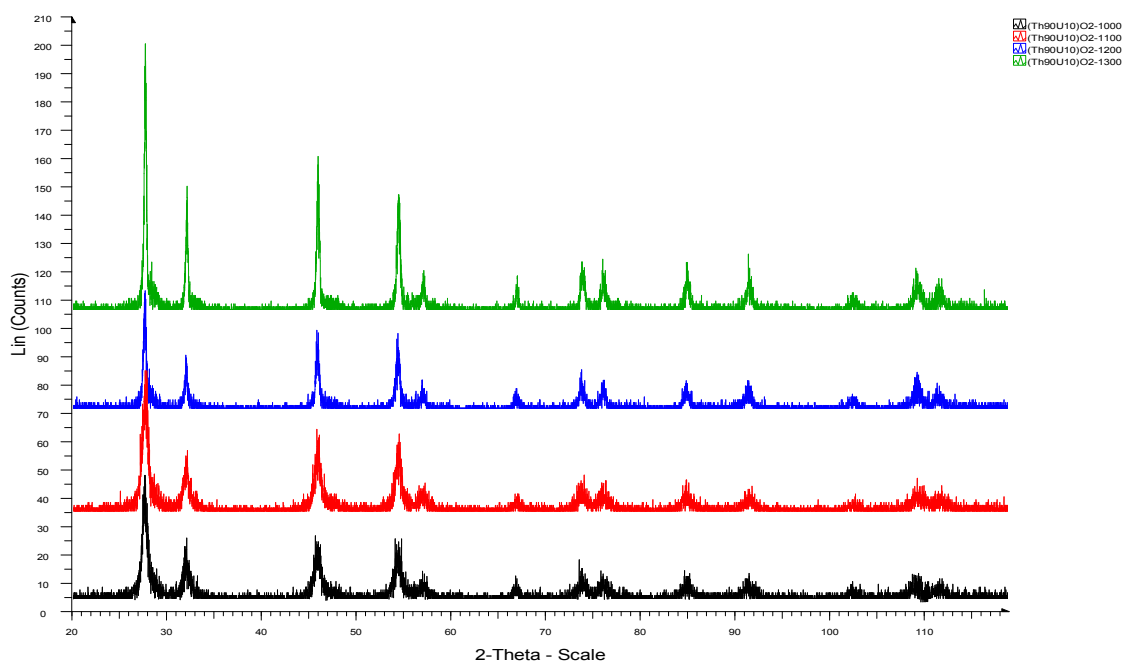
### 5.5 XRD Analysis of $\text{ThO}_2$ , $\text{ThO}_2$ -10% $\text{UO}_2$ and $\text{ThO}_2$ -5% $\text{UO}_2$ Pellets After Sintering in $\text{Ar}+\%5\text{H}_2$ Atmosphere

Figure 5.34 shows the XRD patterns of the  $\text{ThO}_2$  pellets sintered in  $\text{Ar}+\%5\text{H}_2$  atmosphere at  $1300^\circ\text{C}$ ,  $1200^\circ\text{C}$ ,  $1100^\circ\text{C}$  and  $1000^\circ\text{C}$  temperatures. X-ray diffraction (XRD) pattern of  $\text{ThO}_2$  pellets showed only single phase. Additionally, XRD patterns of the MOX pellets are shown in Figure 5.35 for  $\text{ThO}_2$ -10% $\text{UO}_2$  and shown in Figure 5.36 for  $\text{ThO}_2$ -5% $\text{UO}_2$ .

As seen in these figures, the sintered at higher temperature pellets shows the higher intensity and narrower peaks than the sintered at lower temperature. XRD pattern of the pellets with different sintering temperature showed more sharp and intense peak for the pellets sintering at higher temperature, which might indicate the larger grain size of pellets as well as higher crystallinity and the better homogeneity in the pellets.



**Figure 5.34** XRD patterns of the  $\text{ThO}_2$  pellets sintered in  $\text{Ar}+\%5\text{H}_2$  atmosphere at  $1300^\circ\text{C}$ ,  $1200^\circ\text{C}$ ,  $1100^\circ\text{C}$  and  $1000^\circ\text{C}$  for 16 h



**Figure 5.35** XRD patterns of the ThO<sub>2</sub>-10%UO<sub>2</sub> sintered in Ar+5%H<sub>2</sub> atmosphere at 1300°C, 1200°C, 1100°C and 1000°C for 16 h

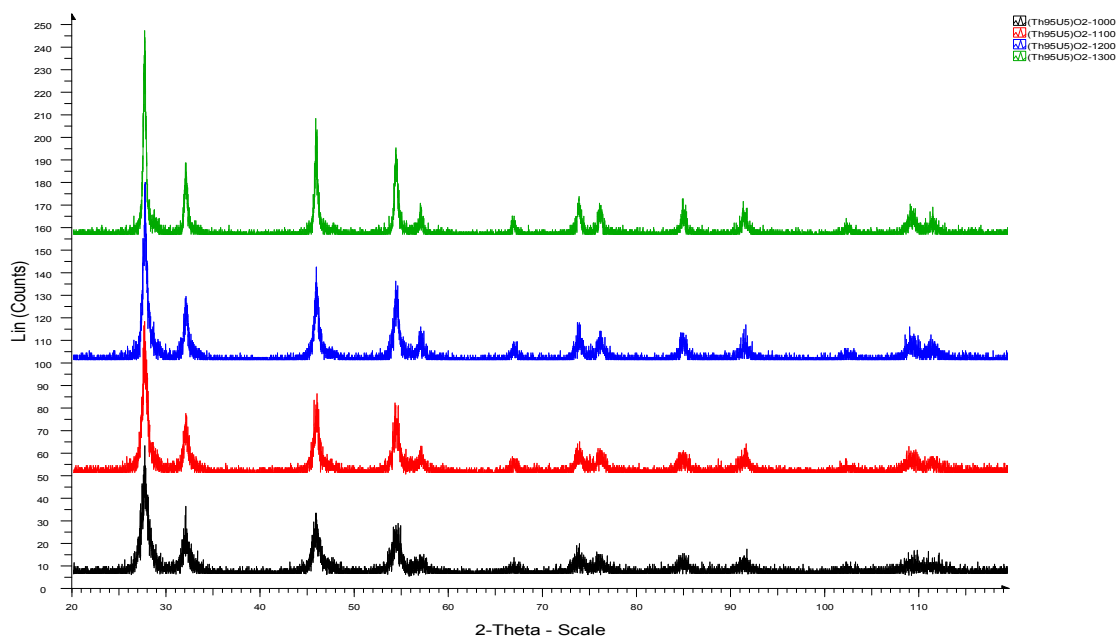


**Figure 5.36** XRD patterns of the ThO<sub>2</sub>-5%UO<sub>2</sub> pellets sintered in Ar+5%H<sub>2</sub> atmosphere at 1300°C, 1200°C, 1100°C and 1000°C for 16 h

Figure 5.37 shows the XRD patterns of the  $\text{ThO}_2$ ,  $\text{ThO}_2$ ,  $\text{ThO}_2$ -10% $\text{UO}_2$  and  $\text{ThO}_2$ -5% $\text{UO}_2$  pellets sintered in  $\text{Ar}+\%5\text{H}_2$  atmosphere at  $1300^\circ\text{C}$  for 16h. It was found that the X-ray peaks of the MOX pellets are stronger, but broader than the  $\text{ThO}_2$  pellets. Furthermore, the increase of the line width broadening of the MOX pellets and the shifting to higher angles of diffraction peaks are attributed to microcrystallinity and local disorder.

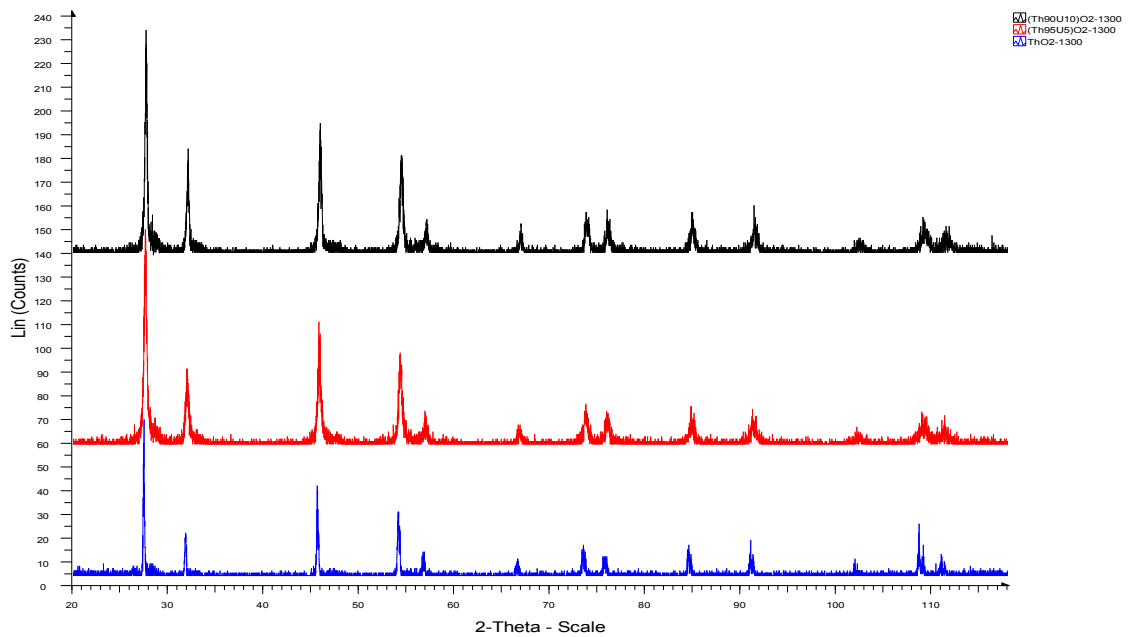


**Figure 5.37** XRD patterns of the  $\text{ThO}_2$ ,  $\text{ThO}_2$ -10% $\text{UO}_2$  and  $\text{ThO}_2$ -5% $\text{UO}_2$  pellets sintered in  $\text{Ar}+\%5\text{H}_2$  atmosphere at  $1300^\circ\text{C}$  for 16 h.

## CHAPTER VI

### CONCLUSION

This thesis was focused on the developing an alternative method to produce thorium, uranium and mixed thorium-uranium dioxide fuel pellets which are prepared by internal gelation technique of sol-gel process. The sol-gel process which is among the methods used for the production of  $\text{UO}_2$ ,  $\text{ThO}_2$  and  $\text{ThO}_2\text{-UO}_2$  mixed oxide fuel pellets allows a high degree of micro-homogeneity of uranium and thorium in the solution stage.

This thesis further aims was to investigate shrinkage behavior and first-stage sintering kinetics of pellets compacted in the  $\text{Ar-}5\text{H}_2$  atmosphere by using dilatometer. Various methods have been used to study the determination of sintering mechanism. Among these, dilatometric studies of isothermal shrinkage for powder compacts have been particularly useful they allow one continuously to follow dimensional variation in the same sample. Shrinkage curves of the  $\text{UO}_2$ ,  $\text{ThO}_2$ ,  $\text{ThO}_2\text{-}10\%\text{UO}_2$  and  $\text{ThO}_2\text{-}5\%\text{UO}_2$  pellets obtained from the dilatometer were used to determine the sintering mechanism, the diffusion coefficients and the activation energy.

In order to evaluate the influence of the preparation method on several chemical compositions of the powders as well as the sintered pellets, the microstructural characterization of the powdered compounds was undertaken in terms of thermogravimetry (TGA/DTA), specific surface area (BET) and crystallization state (XRD). Findings show that the  $(\text{Th,U})\text{O}_2$  powders have a higher O/U ratio, smaller specific surface area and have single phases.

The O/U ratios of the  $\text{UO}_2$ ,  $\text{ThO}_2$ ,  $\text{ThO}_2\text{-}10\%\text{UO}_2$  and  $\text{ThO}_2\text{-}5\%\text{UO}_2$  powders were measured by thermogravimetrically. The higher O/U ratio obtained from TGA/DTA curves indicates the presence of higher concentration of oxygen interstitials.

Specific surface area for  $\text{UO}_2$  and  $\text{ThO}_2$  data are in agreement with these in the literature powders present low surface area values [115]. The increase in the Th metal ion concentration from the  $\text{ThO}_2$ -10% $\text{UO}_2$  and  $\text{ThO}_2$ -5% $\text{UO}_2$  powders, specific surface area of these powders increased from 2.5  $\text{m}^2/\text{g}$  to 3.07  $\text{m}^2/\text{g}$ . [115,116]

After calcination and reduction steps, the  $\text{UO}_2$ ,  $\text{ThO}_2$ ,  $\text{ThO}_2$ -10% $\text{UO}_2$  and  $\text{ThO}_2$ -5% $\text{UO}_2$  microspheres were found extremely hard to pressed directly. The applied pressure was not enough for the microspheres with this hardness to merge them into one another. Use of higher pressure resulted in lamination/end chipping of the pellets. Accordingly, the microspheres were grinded with automatic mortar grinder to obtain soft powder. Furthermore, the lower specific surface area of the powders is related with hardness of the microspheres.

The  $[\text{NO}_3^-]/[\text{M}]$  ratio of solution is an important parameter for obtaining good quality microspheres capable of maintaining their integrity during drying. Also, the feed composition range for obtaining good quality gel is very narrow with regards to  $[\text{M}]$ ,  $[\text{HMTA-Urea}]$  and  $[\text{NO}_3^-]/[\text{M}]$  ratio. Because of that, the hard microspheres could have obtained during gelation into hot silicon oil in glass column.

The XRD data of the  $\text{UO}_2$ ,  $\text{ThO}_2$ ,  $\text{ThO}_2$ -10% $\text{UO}_2$  and  $\text{ThO}_2$ -5% $\text{UO}_2$  powders show that all the powders are of single phased. The XRD peaks are found to be indicating that the material crystalline. The lattice parameters were calculated and found to be 5.453, 5.595, 5.936 and 5.592 Å for  $\text{UO}_2$ ,  $\text{ThO}_2$ ,  $\text{ThO}_2$ -10% $\text{UO}_2$  and  $\text{ThO}_2$ -5% $\text{UO}_2$  powders, respectively. This indicated that the deviation in lattice parameter from ideal value may be due to solubility of oxygen in the crystal lattice.

Both  $\text{ThO}_2$ -10% $\text{UO}_2$  and  $\text{ThO}_2$ -5% $\text{UO}_2$  powders show single phase of  $\text{CaF}_2$  type solid solution similar to the pure  $\text{UO}_2$  and  $\text{ThO}_2$  powders, indicating that solid solutions were formed to extent. But it supposed that the solid solution is not yet fully formed since the FWHM of the peaks is wider than that of pure  $\text{UO}_2$  and  $\text{ThO}_2$ . These appreciable broadening regions in the X-ray diffraction regions of the  $\text{ThO}_2$ -10% $\text{UO}_2$  and  $\text{ThO}_2$ -5% $\text{UO}_2$  powder may in fact correspond to the actual size of the particles.

The XRD pattern of the  $\text{ThO}_2$ ,  $\text{ThO}_2$ -10% $\text{UO}_2$  and  $\text{ThO}_2$ -5% $\text{UO}_2$  pellets sintered at higher temperature shows the higher intensity and narrower peaks than the sintered at

lower temperature, which might indicate the larger grain size of pellets as well as higher crystallinity and the better homogeneity in the pellets.

It was found that the X-ray peaks of the mix oxide pellets ( $\text{ThO}_2$ -10% $\text{UO}_2$  and  $\text{ThO}_2$ -5% $\text{UO}_2$ ) sintered in  $\text{Ar}+5\%\text{H}_2$  atmosphere at  $1300^\circ\text{C}$  are stronger, but broader than that of the  $\text{ThO}_2$  pellets. Furthermore, the increase of the line width broadening of the mix oxide pellets and the shifting to higher angles of diffraction peaks are attributed to micro-crystallinity and local disorder.

The sintering mechanism is considered as consisting of three stages. The most important is the first stage. Because, during this stage solid particles in contact are bonded together and the aggregate shrinks resulting in a decrease of surface area and energy. A method of isolating the initial stage of the process is to employ small spheres of the same diameter touching each other. The neck formation, the neck growth and shrinkage take place by the material transport.

In this study, dilatometric curves were used to determine the sintering mechanism, the diffusion coefficients and the activation energy. The shrinkage behaviour of the  $\text{UO}_2$ ,  $\text{ThO}_2$ ,  $\text{ThO}_2$ -10% $\text{UO}_2$  and  $\text{ThO}_2$ -5% $\text{UO}_2$  pellets were investigated in  $\text{Ar}+5\%\text{H}_2$ . Heating rate of  $5^\circ\text{C}/\text{min}$  was used until the isothermal temperature reached and pellet still remained this temperature for 16h in isothermal condition. Sintering in reducing atmosphere resulted in good microstructure with excellent homogeneity. The dilatometric data was obtained from the curves which  $dL/L_0$  versus time and temperature.

It is very difficult to determine the origin of the curve because the sample will not reach the isothermal temperature immediately. After making the time and shrinkage corrections,  $dY/dt$  is calculated from the dilatometric data.

The onset temperature of sintering was determined from the dilatometric curve as the point at which it deviated from its horizontal path. The onset of sintering was found marginally shift to lower temperature on decreasing the  $\text{UO}_2$  content for compositions  $\text{ThO}_2$ -10% $\text{UO}_2$  and  $\text{ThO}_2$ -5% $\text{UO}_2$ . This occurs at temperatures  $735$  and  $707^\circ\text{C}$ , respectively. This also coincides with the surface area results. Namely, the larger specific surface area gives the smaller onset temperature of sintering. The onset of sintering for pure  $\text{ThO}_2$  occurs at  $800^\circ\text{C}$  which is higher than the uranium-thoria pellets, but pure  $\text{UO}_2$  is much higher occurs at  $990^\circ\text{C}$ .

The temperature, at which the maximum shrinkage rate occurs for a particular composition, was observed to shift lower temperatures with decrease in  $\text{UO}_2$  content for compositions  $\text{ThO}_2$ -10% $\text{UO}_2$  and  $\text{ThO}_2$ -5% $\text{UO}_2$ . This occurs at temperatures 840 and 800°C, respectively. The maximum shrinkage rates for pure  $\text{UO}_2$  and  $\text{ThO}_2$  are higher than the uranium-thoria mix oxide pellets occur at 1100 and 1160°C, respectively. Moreover, the maximum pellet shrinkage at a particular temperature is found for pure  $\text{UO}_2$  while the minimum for pure  $\text{ThO}_2$ .

With the plotting  $\log(dY/dt)$  versus  $\log t$ , a straight line was obtained for each isothermal temperature. The values of  $n$ , for the  $\text{UO}_2$ ,  $\text{ThO}_2$ ,  $\text{ThO}_2$ -10% $\text{UO}_2$  and  $\text{ThO}_2$ -5% $\text{UO}_2$  sintered pellets, were determined from the slope of the line. The values of  $n$  obtained for these pellets sintered in Ar+5%  $\text{H}_2$  is about 0.5, 0.58, 0.53 and 0.45, respectively. The mechanism for the initial stage of sintering for all the pellet groups were considered to be volume diffusion.

After the determination of parameter  $n$ , the diffusion coefficient  $D$  is calculated by using parameter  $n$  and Arrhenius constant,  $K(T)$ . Finally, the activation energies of first-stage sintering for  $\text{UO}_2$ ,  $\text{ThO}_2$ ,  $\text{ThO}_2$ -10% $\text{UO}_2$  and  $\text{ThO}_2$ -5% $\text{UO}_2$  pellets were calculated from the slope of the variation of  $\log D$  versus  $1/T$  and found to be 215.140, 175.105, 198.961 and 111.056 kJ/mol, respectively.

Experimental results for two different compositions of uranium-thoria pellets brings out that the value of activation energy determined increases considerably with increasing uranium content. It is observed that the value of activation energy decreases drastically from pure  $\text{ThO}_2$  with the small addition (5%) of  $\text{UO}_2$ . However, increasing the amount of uranium in the composition (10%  $\text{UO}_2$ ), the value of activation energy is higher than that of pure  $\text{ThO}_2$ .

For nuclear fuel ceramics, it is reported that the diffusion rate is slow under reducing atmosphere and fast under oxidizing atmosphere. Since diffusion is largely dependent on oxygen potential of the sintering atmosphere.

It is known that uranium dioxide and thorium dioxide form a continuous series of solid solutions maintaining their inherent face centered cubic of calcium fluoride ( $\text{CaF}_2$ ) type structure [122]. Statistical substitution of  $\text{Th}^{4+}$  cations by  $\text{U}^{4+}$  in the cubic face-centered lattice of thoria is feasible at all contents when substituted uranium remains quadrivalent. Stoichiometry plays an important role in the diffusion of slower



moving cation in the matrix during sintering. Since  $\text{UO}_2$  is always hyperstoichiometric, its presence in the solution results in defect structure in terms of oxygen interstitial. On the other hand,  $\text{ThO}_2$  is always stoichiometric and difficult to sinter due to the absence of any defects in the crystal lattice. When  $\text{UO}_2$  is added to  $\text{ThO}_2$ , it renders a defect structure which might lead to nonstoichiometric solid solutions of general formula  $\text{Th}_{1-x}\text{U}_x\text{O}_{2+y}$ . This is helpful to sintering in terms of enhancing the diffusion of rate controlling cations in the lattice. This might lead to lower value of activation energy than pure  $\text{ThO}_2$  making environment more favorable for densification.

On the other hand, shrinkage curve of  $\text{ThO}_2$ -10% $\text{UO}_2$  pellet shows the lower shrinkage compared to the other composition. This result is rather unexpected since  $\text{ThO}_2$ -10% $\text{UO}_2$  contains a larger amount of  $\text{UO}_2$ , and therefore should contain higher concentration of oxygen interstitials leading to higher shrinkage. Recently Schram [123] has measured the oxygen potential of  $(\text{Th}_{1-x}\text{U}_x)\text{O}_{2+y}$  solid solution. Author has shown that the oxygen potential of  $(\text{Th}_{1-x}\text{U}_x)\text{O}_{2+y}$  solid solution decreases with increase in uranium concentration (x) although it increases with the oxygen excess (y). Since  $\text{ThO}_2$ -10% $\text{UO}_2$  pellet has a lower oxygen potential than  $\text{ThO}_2$  and  $\text{ThO}_2$ -5% $\text{UO}_2$ , it may be a factor for its lower shrinkage behavior.

Because the activation energies obtained from the first-stage sintering kinetics of isothermal shrinkage found to be lower in reducing atmosphere, the internal gelation technique of the sol-gel process has emerged as a suitable alternative to the conventional powder oxide pelletization route for the fabrication of (Th,U) $\text{O}_2$  mix oxide fuel.

## REFERENCES

- [1] IAEA. Nuclear Technology Review 2015. GC(59)/INF/2.
- [2] IAEA. Annual Report 2014. GC(59)/7.
- [3] IAEA. PRIS. Power Reactor Information System. Available at: <https://www.iaea.org/pris/>.
- [4.] IAEA. Nuclear Power Reactors in the World. Reference Data Series No:2. 2015 Edition.
- [5] Zabunoglu O.H. and Akbas T. (January 2003). Flow Sheet Calculations in Thorex Method for Reprocessing Th-based Spent Fuels. Nuclear Engineering and Design. 219:1, 77-86.
- [6] Thomas Lorenz & Joanna Kidd. (2010). Turkey and Multilateral Nuclear Approaches In The Middle East, The Nonproliferation Review, **17:3**, 513-530.
- [7] The International Institute for Strategic Studies. May 2008. Nuclear Programmes in the Middle East: In the shadow of Iran, Chapter Three: Turkey: power-balance concerns, ISBN:978-0-86079-202-4, 61-71.
- [8] IAEA Technical Cooperation Programme, “IAEA-TC Project Datasheet”, Project No.TUR/3/009, [www.tc.iaea.org/tcweb/projectinfo/projectinfo\\_body.asp](http://www.tc.iaea.org/tcweb/projectinfo/projectinfo_body.asp).
- [9] International Atomic Energy Agency. 2005. Thorium fuel cycle-Potential Benefits and Challenges, IAEA-TECDOC-1450, IAEA, Vienna.
- [10] Boczar P.G., Dyck G.R., Chan P.S.W., Buss D.B. 2002. Recent advances in thorium fuel cycles for CANDU reactors. IAEA-TECDOC-1319, IAEA, Vienna 104–120.
- [11] Milgram M.S. (1982). Once through thorium cycles in CANDU reactors. Report AECL-7516.
- [12] Critoph E., et al. Prospects for self-sufficient thorium cycles in CANDU reactors. Report AECL-8326.
- [13] Dastur A.R., Meneley D.A. and Buss D.B. (1995). Thorium cycle options in CANDU reactors. GLOBAL '95, Proc. Int. Conf. Versailles, 1908–1917.
- [14] Pigford T.H. and Levi H.W. 1981. Nuclear Chemical Engineering, 2<sup>nd</sup> edition, Ch. 6 (Benedict, M., Ed.) McGraw-Hill 283–317.
- [15] Ringel H.D. and Zimmer E. (1979). External gelation of thorium process for preparation of ThO<sub>2</sub> and (Th,U)O<sub>2</sub> fuel kernels. *Nucl. Tech.* **45**, 287.
- [16] Merz E. and Zimmer E. (1984). Aqueous chemical processing of HTR fuel, KfA Report-1899, Jülich, Germany
- [17] Kernforschungsanlage Jülich, Thorium Utilisation in PWRs, Final Report (1979–1988), German-Brazilian Cooperation, Jülich, Germany (1988).

- [18] Balakrishnan K., Ganguly C. (1989). Thorium utilization in Indian power program, *Materials Science Forum*, **48**, 125–138.
- [19] Sinha R. K., et al. 2000. Design and development of AHWR—the Indian thorium fuelled innovative nuclear reactor, Power from Thorium—Status, Strategies and Directions (INSAC 2000), (Proc. Ann. Conf., Mumbai, 2000), Mumbai, India, **1**, 81–106.
- [20] Anantharaman K., et al. 2000. Thorium-based fuel reprocessing and re-fabrication technologies and strategies, Power from Thorium—Status, Strategies and Directions (INSAC 2000), (Proc. Ann. Conf., 2000), BARC, Mumbai, India, **1**, 107–122.
- [21] Proceedings of Conference on Power from Thorium Status, Strategies and Directions, Vol. I & II, Annual Conference of Indian Nuclear Society (INSAC-2000), Mumbai, India (2000).
- [22] Ponomarev-Stepnoi N.N., et al. (1998). Light-water thorium WWER-T reactor, *Atomic Energy*. **85**, 263.
- [23] Murogov V.M., Troyanov M.F. and Shmelev A.N. (1983). The use of thorium in nuclear reactors, *Energoatomizdat*, Moscow.
- [24] Dekoussar V.M., et al. (1999). The ways and possibilities of the use of thorium cycle in light-water and fast reactors, *Yadernaya Energetika*. (In Russian). **1**, 25.
- [25] International Atomic Energy Agency. 1997. Fuel Performance and Fission Product Behavior in Gas Cooled Reactors, IAEA-TECDOC-978, IAEA, Vienna.
- [26] Galperin A., et al. 1998. A Competitive Thorium Fuel Cycle for Pressurized Water Reactors, (Eds.) The Ninth International Conference on Emerging Nuclear Energy System, ICENES'98, Eds. (Ronen Y., Tepper L., Elias E., Eds.) Tel Aviv. **2**, 637.
- [27] Radkowsky A. and Galperin A. (1998). The non-proliferative light water reactor thorium reactor: A new approach to LWR core technology, *Nucl. Tech.* **124**, 215–222.
- [28] International Atomic Energy Agency. 2003. Potential of Thorium-Based Fuel Cycles to Constrain Plutonium and to Reduce the Long-Lived Waste Toxicity, IAEA-TECDOC-1348, IAEA, Vienna.
- [29] Shwageraus E., Hejzlar P. and Kazimi M.S. (2004). Use of thorium for transmutation of plutonium and minor actinides in PWRs, *Nucl. Tech.* **147**, 53–68.
- [30] Lung M., Gremm O. (1998). Perspectives on thorium fuel cycle, *Nuclear Eng. and Des.* **180**, 130–146.
- [31] Wymer R.G. (1968). Thorium Fuel Cycle, Proc. 2<sup>nd</sup> Int. Symp. on Thorium Fuel Cycle, Ten. USA, 1966, US Atomic Energy Commission.
- [32] International Atomic Energy Agency. 1987. Thorium-Based Nuclear Fuel: Current Status and Perspectives, IAEA-TECDOC-412, IAEA, Vienna.
- [33] World Nuclear Association. 2015. Publication on Thorium, registered in England and Wales, number 0121574. <http://www.world-nuclear.org/info/Current-and-Future-Generation/Thorium/>

- [34] Robert H., Ralph M. (2010). Liquid Fluoride Thorium Reactors, *American Scientist*, **98** 4, 304.
- [35] International Atomic Energy Agency. 2012. Experiences and Trends of Manufacturing Technology of Advanced Nuclear Fuels, IAEA-TECDOC-1686, IAEA, Vienna.
- [36] Freshley M. (1972). Behavior of Discrete Plutonium-Dioxide Particles in Mixed-Oxide Fuel During Rapid Power Transients. *Nucl. Technol.* **15**, 239-248.
- [37] Freshley M.D., Brite D.W., Daniel J.L., Hart P.E. (1979). Irradiation-induced densification and PuO<sub>2</sub> particle behavior in mixed-oxide pellet fuel. *J. Nucl. Mater.* **81**, 63-92.
- [38] Vandezande J. 1999. Advanced Methods of Process/Quality Control in Nuclear Reactor Fuel Manufacture, IAEA-TECDOC-1166, IAEA, Vienna, 59.
- [39] Ivison P.K., Cook P.M.A., Bremier S., Walker C.T. (2001). Nuclear Fuel Behaviour Modelling at High Burnup and its Experimental Support, IAEA-TECDOC-1233, IAEA, Vienna, 239.
- [40] Kennedy J.R. et al., (June 21–24, 2004). Advances for Future Nuclear Fuel Cycles, Atalante, France.
- [41] Matzke Hj. in: Sørensen, T. (Ed.). 1981. Non-stoichiometric Oxides. Academic Press, New York. 156.
- [42] Olander D.R. (1976). Fundamental Aspects of Nuclear Reactor Fuel Elements, TID-26711-P1, *US Department of Energy*. 145.
- [43] Lee B.H., Koo Y.H., Sohn D.S. (2001). Nuclear Fuel Behaviour Modelling at High Burnup and its Experimental Support, IAEA-TECDOC-1233, IAEA, Vienna, 247.
- [44] Leyva A.G., Vega D., Trimacor V., Mar, D. (2002). Homogeneity characterisation of sintered (U,Gd)O<sub>2</sub> pellets by X-Ray diffraction. *J. Nucl. Mater.* **303**, 29-33.
- [45] Vettraino F., Magnani G., La Torretta T., Marmo E., Coelli S., Luzzi L., Ossi P., Zappa G. (1999). Preliminary fabrication and characterisation of inert matrix and thoria fuels for plutonium disposition in light water reactors. *J. Nucl. Mater.* **274**, 23-33.
- [46] Magill J., Peerani P., Matzke Hj., Van Geel J. 21–23 November, 1995. in: IAEA Technical Committee Meeting on Advanced Fuels with Reduced Actinide Generation, Vienna.
- [47] Rubbia C., Buono S., Gonzalez E., Kadi Y., Rubio J.A. (12 December, 1995). European Organization for Nuclear Research, CERN/AT/95-53 (ET).
- [48] Feiveson H.A., Rodionov S.N. (1997). *Sci. Global Secur.* **6**, 265.
- [49] Kazimi M.S., Driscoll M.J., Ballinger R.G., Clarno K.T., Czerwinski K.R., Hejzlar P., LaFond P.J., Long Y., Meyer J.E., Reynard M.P., Schultz S.P., Zhao X. (June 1999). Proliferation Resistant, Low Cost, Thoria–Urania Fuel for Light Water Reactors, Annual Report, Nuclear Engineering Department, Massachusetts Institute of Technology (MIT), Cambridge, MA.

- [50] Magill J., Peerani P., Van Geel J. June 1–4, 1997. Second International ARS Topical Meeting on Advanced Reactor Safety, Orlando, Florida.
- [51] Kazimi M.S., Pilat E.E., Driscoll M.J., Xu Z., Wang D., Zhao X. September, 2001. International Conference on: Back-End of the Fuel Cycle: From Research to Solutions, Global, Paris, France.
- [52] Philip E. MacDonald. (1999). Advanced Proliferation Resistant, Lower Cost Uranium–Thorium Dioxide Fuels for Light Water Reactors, US Department of Energy Nuclear Energy Research Initiative, NERI 99- 0153.
- [53] Kazimi M.S., Czerwinski K. R., Driscoll M. J., Hejzlar P., Meyer J.E. (April, 1999). On the Use of Thorium in Light Water Reactors, MIT-NFC- 0016, Nuclear Engineering Department, MIT.
- [54] Zhao X., Driscoll M.J., Kazimi M.S. (1999). Rationale for Reconsideration of the Thorium Cycle in Light-Water Reactors. *Trans. Am. Nucl. Soc.* **80**, 43-44.
- [55] Dehaut Ph., Bourgeois L., Chevrel H. (2001). Activation energy of  $\text{UO}_2$  and  $\text{UO}_{2+x}$  sintering. *J. Nucl. Mater.* **299**. 250-259.
- [56] Lahiri D., Ramana Rao S.V., Hemantha Rao G.V.S., Srivastava R.K. (2006). Densification behaviour of  $\text{UO}_2$  in six different atmospheres. Study on sintering kinetics and activation energy of  $\text{UO}_2$  pellets using three different methods. *J. Nucl. Mater.* **357**. 88–96.
- [57] Kutty T.R.G., Hegde P.V., Khan K.B., Basak U., Pillai S.N., Sengupta A.K., Jain G.C., Majumdar S., Kamath H.S., Purusotham D.S.C. (2002). Densification behaviour of  $\text{UO}_2$  in six different atmospheres. *J. Nucl. Mater.* **305**. 159.
- [58] Lay K.W., Carter R.E. (1969). Role of the O/U ratio on the sintering of  $\text{UO}_2$ . *J. Nucl. Mater.* **30**, 74-87.
- [59] Woolfrey J.L. (1972). Effect of Green Density on the Initial-Stage Sintering Kinetics of  $\text{UO}_{2s}$ . *J. Am. Ceram. Soc.* **55**, 383.
- [60] J Bacmann J., Cizeron G. (1969). Contribution a l'etude des mecanismes du debut de frittage du bioxyde d'uranium. *J. Nucl. Mater.* **33**, 271-285.
- [61] Bacmann J.J., Cizeron G. (1968). Dorn Method in the Study of Initial Phase of Uranium Dioxide Sintering. *J. Am. Ceram. Soc.* **51**, 209-212.
- [62] Ristic M.M., Kostic E. (1963). NP-14124.
- [63] Clavier N., Podor R., Deliere L., Ravaux J., Dacheux N. (2013). Combining in situ HT-ESEM observations and dilatometry: An original and fast way to the sintering map of  $\text{ThO}_2$ . *Mater. Chem. Phys.* **137**. 742–749.
- [64] Ray A., Banerjee J., Kutty T.R.G., Kumar Arun, Banerjee S. (2012). Construction of master sintering curve of  $\text{ThO}_2$  pellets using optimization technique. *Sci. Sint.* **44**. 147–160.
- [65] Kutty T.R.G., Khan K.B., Hedge P.V., Banerjee J., Sengupta A.K., Majumdar S., Kamath H.S. (2004). Development of a master sintering curve for  $\text{ThO}_2$ . *J. Nucl. Mater.* **327**. 211-219.
- [66] Banerjee J., Ray A., Kumar A., Banerjee S. (2013). Studies on sintering kinetics of  $\text{ThO}_2$ – $\text{UO}_2$  pellets using master sintering curve approach. *J. Nucl. Mater.* **443**. 467-478

- [67] M.T. Aybers. (1989). Investigation of the First-Stage Sintering Kinetics of  $\text{UO}_2$ ,  $\text{ThO}_2$  and  $(\text{Th,U})\text{O}_2$ . PhD. Thesis.
- [68] Kutty T.R.G., Hegde P.V., Khan K.B., Jarvis T., Sengupta A.K., Majumdar S., Kamath H.S. (2004). Characterization and densification studies on  $\text{ThO}_2$ - $\text{UO}_2$  pellets derived from  $\text{ThO}_2$  and  $\text{U}_3\text{O}_8$  powders. *J. Nucl. Mater.* **335**, 462–470.
- [69] Kutty T.R.G., Nair M.R., Sengupta P., Basak U., Kumar Arun, Kamath H.S. (2008). Characterization of  $(\text{Th,U})\text{O}_2$  fuel pellets made by impregnation technique. *J. Nucl. Mater.* **374**, 9–19.
- [70] Banerjee J., Kutty T.R.G., Kumar Arun, Kamat H.S., Banerjee S. (2011). Characterization of  $(\text{Th,U})\text{O}_2$  fuel pellets made by impregnation technique. *J. Nucl. Mater.* **408**, 224–230.
- [71] M.T. Aybers. (1994). The sintering apparent activation energy of  $(\text{U}_{0.8}, \text{Th}_{0.2})\text{O}_2$  in reducing the oxidizing atmospheres. *J. Nucl. Mater.* **210**, 73–77.
- [72] M.T. Aybers (1995). Etude du stade initial de frittage des oxydes:  $(\text{U}_{0.8}, \text{Th}_{0.2})\text{O}_{2+x}$ ,  $(\text{U}_{0.2}, \text{Th}_{0.8})\text{O}_{2+x}$ ,  $(\text{U}_{0.05}, \text{Th}_{0.95})\text{O}_{2+x}$ . *J. Nucl. Mater.* **226**, 27–33.
- [73] WNA. World Nuclear Association. <http://www.worldnuclear.org/info/inf75.html>, 10.05.2015.
- [74] WNA. World Nuclear Association. <http://www.world-nuclear.org/info/Nuclear-Fuel-Cycle/Uranium-Resources/Supply-of-Uranium/>, 10.05.2015.
- [75] Thomas Augusto Guisard Restivo, Selma Luiza Silva. (1999). Specific Surface Area Determination by TG/DSC, *Thermochimica Acta.* **328**, 47-53.
- [76] Belle J. 1961. Uranium Dioxide: Properties and Nuclear Applications. Naval Reactors, Division of Reactor Development. United States Atomic Energy Commission. Washington, D. C.
- [77] Katz J. J., Seaborg G. T., Mors L. R. 1986. The Chemistry of the Actinide Element, 1, 2nd ed., Chapman and Hall, New York.
- [78] Proc.Symp. May 3-6, 1966. “Thorium Fuel Cycle”, Gatlinburg, Tennessee, CONF-660524, US Atomic Energy Commission.
- [79] McBride, J. P. (1966). Preparation of  $\text{UO}_2$  Microspheres by a Sol-Gel Technique. ORNL-3874
- [80] The IAEA-NEA publication Uranium 2014: Resources, Production and Demand (Red Book), OECD Nuclear Energy Agency and the International Atomic Energy Agency.
- [81] Kanij J.B.W., Noothout A.J., Votocek O. (1974). The KEMA U(VI) Process for the Production of  $\text{UO}_2$  Microspheres, in Sol-gel Process for Fuel Fabrication, International Atomic Energy Agency Report, IAEA-161, Vienna, pp 185–195.
- [82] Bruggheens F.W., Noothout A.J., Hermans M.E.A., Kanij J.B.W., Votoce O. 1970. A U(VI)-Process for Microsphere Production, in Proceedings of Symposium on Sol-Gel Processes and Reactor Fuel Cycles, CONF-700502, U.S. Atomic Energy Commission, Washington, pp 252–263
- [83] Aparicio M. et al. (eds.) 2012. Sol-Gel Processing for Conventional and Alternative Energy, Advances in Sol-Gel Derived Materials and Technologies, DOI: 10.1007/978-1-4614-1957-0\_16, Springer Science+Business Media, New York.

- [84] Collins J.L., Lloyd M.H., Fellows R.L. (1987). The basic chemistry involved in the internal-gelation method of precipitating uranium as determined by pH measurements. *Radiochemica Acta*. **42**, 121-134.
- [85] V.N. Vaidya, S.K. Mukerjee, J.K. Joshi, R.V. Kamat, D.D. Sood. (1987). A study of chemical parameters of the internal gelation based sol-gel process for uranium dioxide. *J Nucl Mater*. **148**, 324–331.
- [86] Lloyd M.H., Biscoff K., Peng K., Nissen H.U., Wessicken R. (1976). Crystal habit and phase attribution of U(VI) oxides in a gelation process. *J Inorg Nucl Chem*. **38**, 1141.
- [87] Kumar N., Sharma R.K., Ganatra V.R., Mukerjee S.K., Vaidya V.N., Sood D.D. (1991). Studies of the preparation of thoria and thoria-urania microspheres using internal gelation process. *Nucl Technol*. **96**, 169–177.
- [88] Thümmler F. and Thomma W. (June 1967). The Sintering Process. *Metallurgical Reviews No. 115*, **12**, 69–108.
- [89] Suk-Joong L.Kang. 2005. Sintering Densification, Grain Growth, and Microstructure. Elsevier Butterworth-Heinemann. 1<sup>st</sup> published.
- [90] Rahaman M.N. 2003. Ceramic Processing and Sintering, 2<sup>nd</sup> Edition. (Marcel Dekker Inc.). New York Basel.
- [91] Kuczynski G.C. (1949). Self-diffusion in sintering of metallic particles, *Metall. Trans. AIME*. **185**, 169–78.
- [92] Johnson K.L., Kendall K., Roberts A.D. (1971). Surface energy and the contact of elastic solids. *Proc. Roy. Soc. A*. **324**, 301-313.
- [93] Coble R.L. (1961). Sintering crystalline solids. I. Intermediate and final state diffusion models; Sintering crystalline solids. II. Experimental test of diffusion models in power compacts. *J. Appl. Phys.* **32**, 787; **32**, 793.
- [94] Johnson D. L., Clarke T. M. (1964). Grain Boundary and Volume Diffusion in the Sintering of Silver. *Acta. Met.* **12**, 1173.
- [95] Johnson D. L., Cutler I. B. (1963). Diffusion sintering, initial stage sintering models and their application to shrinkage of powder compacts. *J. Amer. Ceram. Soc.* **46**, 541.
- [96] Coble R. L. (1958). Initial Sintering of Alumina and Hematite. *J. Am. Ceram. Soc.* **41**, 55-62.
- [97] Bannister M. J. (1968). Shape Sensitivity of Initial Sintering Equations. *J. Am. Ceram. Soc.* **51**, 548-553.
- [98] El-Sayed Ali M.M. (1979). Etude Du Stade Initiale De Frittage Des Oxydes D'Actinides: UO<sub>2</sub>, PuO<sub>2</sub> et De Leurs Melanges, PhD. Thesis.
- [99] Rolando M.A., Roque-Malherbe. 2009. The Physical Chemistry of Materials: Energy and Environmental Application. Printed in the United States of America. CRC Press. ISBN:978-1-4200-8272-2
- [100] Coats A. W.; Redfern J. P. (1963). Thermogravimetric Analysis: A Review. *Analyst*. **88**. 906–924. doi:10.1039/AN9638800906.
- [101] Hill J. O. 1991. For Better Thermal Analysis. 3rd Edition, International Confederation for Thermal Analysis, New Castle, Australia.

- [102] Brunauer S., Emmett P.H. and Teller E., (1938). *J. Am. Chem. Soc.* **60**, 309. doi:10.1021/ja01269a023.
- [103] Andrew R. Barron. 07 May 2009. Physical Methods in Chemistry and Nano Science, Chapter-2:Physical and Thermal Analysis-BET Surface Area Analysis of Nanoparticles. [http://cnx.org/contents/ba27839d-5042-4a40-afcf-c0e6e39fb454@21.1:38/Physical\\_Methods\\_in\\_Chemistry](http://cnx.org/contents/ba27839d-5042-4a40-afcf-c0e6e39fb454@21.1:38/Physical_Methods_in_Chemistry)
- [104] Ralph T. Yang. 2003. Adsorbents: Fundamentals and Applications. Wiley-Blackwell. ISBN: 978-0-471-29741-3
- [105] Jozef Toth. 2002. Adsorption: Theory, Modeling, and Analysis, (Surfactant Science Series, Volume 107) Publisher, 1<sup>st</sup> edition. Marcel Dekker.
- [106] Duong D. Do. 1998. Adsorption Analysis: Equilibria and Kinetics. Publisher: Imperial College Pres.
- [107] Yang Leng, JohnWiley & Sons (Asia). 2008. Materials Characterization, Introduction to Microscopic and Spectroscopic Methods, p.58-69.
- [108] Bish D.L. and Post J.E. (ed.) 1989. Modern powder diffraction. Mineralogical Society of America, Washington, DC.
- [109] Harold T. Stokes. 1998. Solid State Physics, for Advanced Undergraduate Students. Third edition, second printing. Brigham Young University.
- [110] Li B., Wang X., Yan M., Li L. (2002). Preparation and characterization of nano-TiO<sub>2</sub> powder. *Materials Chemistry and Physics*. **78**, 184-188.
- [111] Ying L., Hon L.S., White T., Withers R. and Hai L.B. (2003). Controlled Nanophase Development in Photocatalytic Titania. *Materials Transactions*. **44**, 1328-1332.
- [112] Barakat M.A., Hayes G., Ismat Shah S. (2005). Effect of cobalt doping on the phase transformation of TiO<sub>2</sub> nanoparticles. *J. Nanoscience and Nanotechnology*. **5**, 1-7.
- [113] Bernard Dennis Cullity. 1956. Elements of X-Ray diffraction. Addison-Wesley publishing company.
- [114] Riella H.G., Martinez L.G., Imakuma K. (1988). Determination of Crystallite Size in UO<sub>2+x</sub> Powder by X-Ray Diffraction. *J. Nucl. Mat.* **153**, 71.
- [115] Hingant N., Claviera N., Dacheuxa N., Barre S., Hubert S., Obbade F., Tabora F. Abraham. (2009). Preparation, sintering and leaching of optimized uranium thorium dioxides. *Journal of Nuclear Materials*, **385** , 400–406.
- [116] Pai Rajesh V., Dehadraya J.V., Shovit Bhattacharya , Gupta S.K., Mukerjee S.K. (2008). Fabrication of dense (Th,U)O<sub>2</sub> pellets through microspheres impregnation technique. *Journal of Nuclear Materials*. **381**, 249–258.
- [117] Wasserstein B. (1951). Cube-edges of uraninites as a criterion of age? *Nature* (London), 168, 380. ISSN: 0028-0836
- [118] Pawel E. Tomaszewski. (1992). Structural phase transitions in crystals. I. Database. *Phase Transitions: A Multinational Journal*. **38**,127-220. DOI:10.1080/01411599208222899



- [119] Kutty T.R.G., Somayajulu P.S., Khan K.B., Kumar A., Kamath H.S. (2009). Characterization of (Th,U)O<sub>2</sub> pellets made by advanced CAP process. *J. Nucl. Mater.* **384**, 303–310.
- [120] Sayed Ali M.El., Sorensen O.T. (1982). Quasi-isothermal dilatometric studies of the influence of oxygen pressure on the initial sintering stage of UO<sub>2</sub> powder compacts *J. Therm. Anal.* **25**. 175-180.
- [121] M. El Sayed Ali, O.T. Sorensen, August 22-28, 1982. In: Thermal Analysis. Proceedings of the Seventh International Conference on Thermal Analysis. Kingston, Ed. by B. Miller (Wiley, New York) 344-349.
- [122] Lambertson W.A., Mueller M.H., Gunzel Jr. F.H. (1953). Uranium Oxide Phase Equilibrium Systems: IV, UO<sub>2</sub>–ThO<sub>2</sub>. *J. Am. Ceram. Soc.* **36**, 397–399.
- [123] Schram R.P.C. (2005). Analysis of the oxygen potential of Th<sub>1-y</sub>U<sub>y</sub>O<sub>2+x</sub>. *J. Nucl. Mater.* **344**. 223-229

## CURRICULUM VITAE

Surname, Name: SÖKÜCÜ (ALTUNBAYRAK), AYŞE SİBEL

Nationality: Turkish (TC)

Date and Place of Birth: 01 January 1980, GAZİANTEP

Marital Status: Married

Phone: +90 532 305 9801

e-mail: aysesibel.sokucu@taek.gov.tr

## EDUCATION

Degree	Institution	Yer of Graduation
MS	Gaziantep University, Physics Eng.	2007
BS	Gaziantep University, Physics Eng.	2004
High School	Cem Sultan Lisesi, Bursa	1997

## WORK EXPERIENCE

Year	Place	Enrollment
2009-Present	ÇNAEM / TAEK	Researcher
2005-2009	Kilis 7 Aralık University	Research Assistant

## FOREIGN LANGUAGES

English

## PUBLICATIONS

1. Yazici A. N., Bedir M. and Sökücü A. S. (2007). The analysis of dosimetric thermoluminescent glow peak of CaF<sub>2</sub>:Mn after  $\beta$ -irradiation. *Nuclear Inst. and Methods in Physics Research*, **259**, 955-965.,
2. Sökücü, A.Sibel, Bedir M. and Aybers M. T. (2015). Study on preparation and first-stage sintering kinetics of ThO<sub>2</sub>-UO<sub>2</sub> pellets made by sol-gel microspheres technique. *Acta Physica Polonica A*, **127**, 987-991.